2008

A Study of Rheological and Thermodynamic Properties of Polymer-Clay Gels and Multilayered Films

Eduard Adrian Stefanescu
Louisiana State University and Agricultural and Mechanical College, estefa1@lsu.edu

A STUDY OF RHEOLOGICAL AND THERMODYNAMIC PROPERTIES OF POLYMER-CLAY GELS AND MULTILAYERED FILMS

A Dissertation

Submitted to the Graduate Faculty of the
Louisiana State University and
Agricultural and Mechanical College
in partial fulfillment of the
requirements for the degree of
Doctor of Philosophy

In

The Department of Chemistry

by
Eduard Adrian Stefanescu
B.S., Technical University of Iasi, Romania, 2004
May 2008

This dissertation is dedicated to my grandmother, Ana Stefanescu (1936 – 1996),

for her enormous love and support

ACKNOWLEDGEMENTS

I would like to express my gratitude towards Dr. William H. Daly, Dr. Gudrun Schmidt and Dr. Ioan I. Negulescu, my major professors, for their invaluable guidance, encouragement, and counseling during my Ph.D. program.

A special thank is offered to Dr. Jayne Garno and Wanda LeBlanc of LSU for the training offered in atomic force microscopy and X-ray diffraction, respectively, and for assistance in interpreting the results.

I would also like to thank the members of my graduate committee: Dr. Bin Chen and Dr. Ilya Vekhter for their important feedback on my research.

Finally, yet importantly, I would like to thank my group members, my friends, my family and my wife for their tremendous help and support.

TABLE OF CONTENTS

LIST OF TABLES

LIST OF FIGURES

LIST OF ABBREVIATIONS

AFM	Atomic Force Microscopy
CNA	Montmorillonite, Cloisite Na+, natural Smectite type clay
DEA	Dielectric Analysis
DMA	Dynamic Mechanic Analysis
DSC	Differential Scanning Calorimetry
LRD	Laponite RD, synthetic Hectorite type clay
PEO	Poly(ethylene oxide)
SANS	Small Angle Neutron Scattering
SEM	Scanning Electron Microscopy
TGA	Thermo-gravimetric Analysis
TMDSC	Temperature Modulated Differential Scanning Calorimetry
XRD	X-ray Diffraction

ABSTRACT

The overall objective of the research presented here is to understand the nanoscopic and microscopic structures that exist in dispersions of laponite and montmorillonite in poly(ethylene oxide), (PEO) and to correlate their shear responses with the final structure and properties of multilayered nanocomposite films prepared from these dispersions. These structures were examined as a function of polymer molecular weight, polymer and clay concentrations, and type of clay used to prepare the nanocomposites. A sequence of shear and elongational rheological measurements is used to provide a more complete physical picture on the structure of polymer-clay hydrogels, while a combination of techniques such microscopy (SEM, AFM, PLOM), XRD, DSC, TGA, DMA is used to study the structure and thermo-mechanical properties of the multilayered nanocomposite films. It was found that polymer molecular weight, polymer and clay concentrations, and the aspect-ratio of clay platelets strongly influence the rheology of nanocomposite dispersions as well as crystallinity, toughness and thermal properties of solid nanocomposite films prepared from such dispersions.

CHAPTER 1
INTRODUCTION AND LITERATURE REVIEW

1.1 Polymer-Clay Nanocomposites

In recent years a broad literature has emerged that examines the fundamental relationships between network structure, chain dynamics, ionic conductivity and dimensional stability, in cross-linked nanosized polymer-silicate networks.[1-16] Highly ordered polymer nanocomposites are complex materials that display a rich morphological behavior because of variations in composition, structure, and properties on a nanometer length scale.[6, 14, 15] Novel physical properties of soft and bulk polymer nanocomposite materials are also dependent on the supramolecular organization of the nanostructures.[17-20] The presence of the nanoparticle and the interaction of the polymer with the particle as well as the particle orientation in an aqueous precursor phase may lead to a variety of ordered composite materials in the bulk or film.[18, 21] Anisotropic clay particles promote supramolecular organization[18, 22] similar to other systems such as liquid crystalline polymers[23], surfactants[24], block copolymers[25-27] and peptides[28]. Depending on the concentration of polymer and clay, the polymer type and molecular weight, the clay size, shape and surface chemistry, one may generate a variety of dispersions[29, 30], solutions[31], smart gels[32-34], shake gels[35, 36], glues[32-34] and gum-like gels[32-34, 37, 38] all of which may be excellent precursors for new hierarchically structured bulk materials.[5, 39] Some of these soft and bulk nanocomposite materials are sensitive to external stimuli including: light, temperature, pH, salt concentration, shear, pressure and electric fields, leading to novel properties that attract much scientific and technological interest.[5, 37]

Supramolecular polymer-nanoparticle composites combine the advantages of tailored nanometer structures with self-assembly on all length scales. Design and fabrication of polymer-nanoparticle electrolytes from solutions and gels would allow for solid polymer electrolytes to be shaped around nearly any form. In the absence of defects these materials should be transparent[5] with highly regular d_{00l} reflections in diffraction patterns.[2, 5, 32-34, 40-42] In solution, synthetic clay nanoparticles are exfoliated and act as multifunctional cross-links to poly(ethylene oxide) (PEO) polymers, thereby building a network.[5, 32-34, 40, 41] The shear orientation of this network, combined with simultaneous solvent evaporation, allows for the spontaneous assembly of unique supramolecular multilayered films.[5, 14] The resulting transparent films have highly ordered structures with sheet-like layers of oriented nanoparticles.[5] In these films, the polymer crystallization in confinement and under shear flow is not well understood and the subject of much speculation. Understanding the origin of these highly ordered structures requires a fundamental study.

The exfoliation, intercalation and aggregation of clays in PEO nanocomposites has been extensively studied in the past.[1, 2, 43-47] The dispersion of clay platelets in polymer nanocomposite films can be achieved using either layer-to-layer approaches or the Langmuir-Blodgett method.[45, 46, 48] Intercalation of PEO chains between the inorganic clay layers has been shown to reduce or completely suppress polymer crystallinity, depending on the polymer-clay composition as well as other parameters such as salt, humidity, structural defects, etc.[1,2] Cation movement in the clay interlayer space is radically improved by coordination to the polymer that easily replaces the water molecules of hydration [3]. Unfortunately the polymer crystallinity, as well as ionic conductivity of the nanocomposites, is often not reproducible and strongly depends on the thermal history of the samples as can be observed in different heating cycles of thermal experiments. The amount of polymer adsorbed to the clay is controlled by the layer charge density on the clay.[1] For example in PEO-montmorillonite nanocomposites the heterogeneous nucleation of PEO competes with the PEO coordination to sodium ions, which inhibit PEO crystallinity.[49-51] Although it has been found that ionic transport in polymer electrolytes occurs in the amorphous PEO phases above their glass transition temperature, ionic conductivity in the polymer crystalline phase has also been observed. The amount and orientation of the crystalline phase is thus very important in controlling specific properties.

To examine the polymer-clay interactions, a combination of methods is advisable. Among them, microscopy and scattering are techniques for studying structure and providing a measure of size, shape and interfacial polymer conformation. Recent advances in ultra small angle scattering techniques offer advantages and complementary information.[52] Rheology and mechanical testing may nicely distinguish between properties of chemically[37] versus physically cross-linked polymer-clay materials.[33, 34] Since shear can influence both the macroscopic texture and the orientation of the anisotropic particle on the nanometer length scale, it is helpful to combine the above mentioned techniques and correlate changes in the mechanical properties with changes in structure on different length scales.

1.2 Laponite Clay

Laponite is a disc-shaped, entirely synthetic, phyllosilicate clay that resembles the natural smectite mineral Hectorite in both structure and composition.[53] This clay is both inexpensive and environmentally benign. In an ideal laponite crystal the octahedral layer of six magnesium atoms is sandwiched between two tetrahedral layers, each one composed of four silicone atoms, as indicated in Figure 1.1. The positive charge carried by magnesium and silicone atoms is neutralized by twenty oxygen atoms and four hydroxyl groups. As opposed to the ideal structure, the real crystal structure of laponite contains defects so that some magnesium atoms are either missing entirely in some cases, or are substituted by lithium atoms in some other cases.[54] The empirical formula of laponite, $[Na^{+0.7}(Mg_{5.5}Li_{0.3})Si_8O_{20}(OH)_4]^{-0.7}$, indicates a negative charge of 0.7 per unit cell. The height of the unit cell corresponds to the thickness of the laponite crystal. The laponite disk, presented in Figure 1.2, is obtained by repeating the unit cell (Figure 1.1) 30,000 to 40,000 times in the two directions.

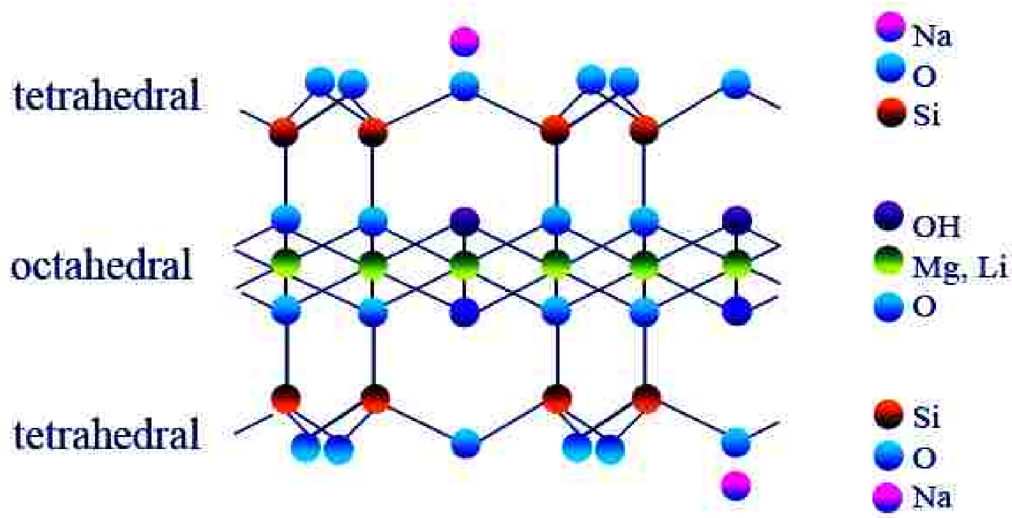

Figure 1.1: The ideal crystal structure of laponite

The platelets dimensions, 25 - 30 nm diameter and 1 nm thickness, have been obtained by means of small angle neutron [55, 56] and X-ray scattering [57] measurements that were performed on dilute laponite solutions. The large aspect ratio of laponite platelets may promote a supramolecular organization[18, 22] similar to other systems such as liquid crystalline polymers[23], surfactants[24], block copolymers[25-27] and peptides[28].

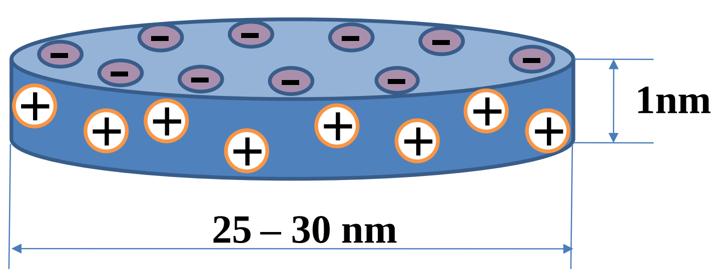

Figure 1.2: Sketch of a laponite platelet at neutral pH

In the dry powdery state the platelets arrange themselves on top of each other forming stacks. The negatively charged faces of individual platelets (Figure 1.2) are held together electrostatically by sharing sodium cations in the interlayer region. [54] When suspended in water, the sodium cations become hydrated, which leads to the screening of their interactions with the clay particles. In this way an electrical double layer forms that causes the particles to repel each-other and exfoliate.[54] At higher ionic strength, as the screening length decreases, the positive double layers at the edges of platelets can approach the negatively charged double layers on the faces.[58] The high-density gel state of laponite, called the house-of-cards structure (Figure 1.3), occurs when the screening length is sufficiently short so that this attractive interaction dominates.[59] This structure is readily observed if dry laponite powder is mixed with tap water which typically has a high ion concentration. As indicated in Figure 1.2 a single dispersed platelet has a negative charge on the faces, produced by isomorphous substitution, while the edge has a positive charge at neutral pH. At a higher pH (pH ≈ 10) the formation of a negative charge on the edge of the particle is favored. The small localized charges at the edges of laponite particles are generated by ionization or protonation of the hydroxyl groups at the end of the crystal structure.

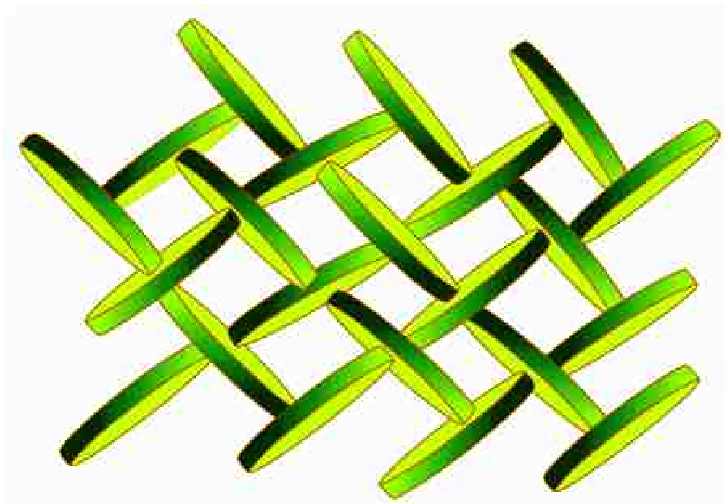

Figure 1.3: Schematic representation of a "House of cards" laponite gel structure

1.3 Montmorillonite Clay

Montmorillonite belongs to the smectite class and is a 2:1 charged phyllosilicate (two tetrahedral sheets sandwiching a central octahedral sheet) that contains exchangeable interlayer cations and shows the ability to intercalate various polymers, such as PEO. The platelet-shaped particles range on average in size from ca. 70 to 100 nm across and are approximately 1 nm thick. Average diameters of about 1 μm have been also reported.[14,60] Chemically, montmorillonite is hydrated sodium calcium aluminium magnesium silicate hydroxide, with the crystal structure $(Na, Ca)_{0.33}(Al, Mg)_2(Si_4O_{10})(OH)_2 \times nH_2O$, as indicated in Figure 1.4.[60] Other cations that may appear in the structure of montmorillonite are potassium and iron.

Montmorillonite produces an opaque aqueous suspension of predominantly exfoliated platelets.[14] Being a hygroscopic material the water content of the clay is variable. Because of its high affinity for water montmorillonite can swell to levels that go far beyond its original volumes.[61] The amount of swelling is largely due to the type of exchangeable cation contained by the clay. When sodium is the predominant cation the clay can expand in the presence of moisture several times its original volume. [60] When dispersed alone in water such clays exhibit a Newtonian behavior, but in the presence of polymers the interaction between the polymer chains and the particles causes a major change in the rheological behavior of dispersions.[62] Flow birefringence studies demonstrated that upon shear the clay platelets orient along the flow direction.[33, 34] In solution the amount of polymer adsorbed is limited by the clay surface area. [41]

Montmorillonite finds important applications in the oil industry where it is used as a component of drilling mud, making the mud slurry viscous. Its presence in the mud slurry helps in cooling the drilling bit and in suspending the drilled solids to facilitate removal from the site. [60] The clay is also used as a soil additive, where its purpose is to maintain a high level of moisture in water deficient soils. Other applications include its use as a component of foundry sands and as a desiccant to remove moisture from air and gases.

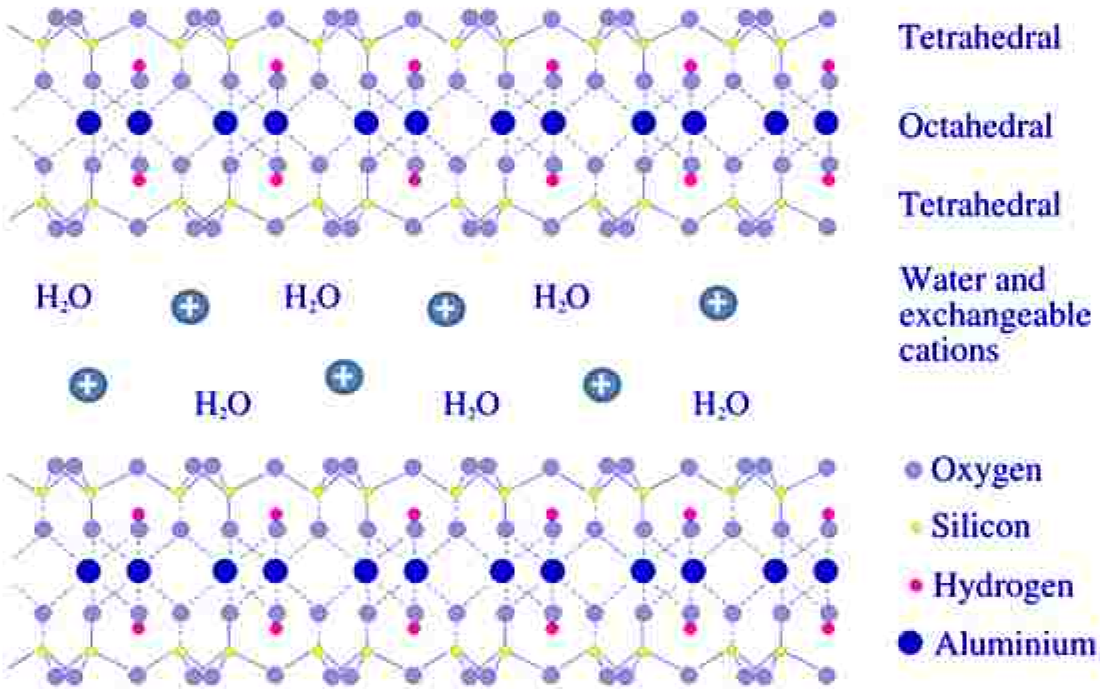

Figure 1.4: The structural organization of montmorillonite clay. Two crystal units are presented along with water molecules and exchangeable cations

1.4 Poly(ethylene oxide) (PEO)

Due to its flexible chain structure, beneficial for ionic transport, and due to its ability to act as a solid solvent for many metal salts, poly(ethylene oxide) (PEO) is among the most extensively used polymers for fabricating solid state polyelectrolytes.[1, 2, 5, 14, 15, 35, 40, 43, 46, 49, 63-67] Poly(ethylene oxide) is prepared industrially by the ring-opening polymerization of ethylene oxide.[68] The ethylene oxide monomer is nothing more than an epoxide ring, where two corners of the molecule consist of -CH_2- linkages and the third corner is an oxygen, -O-. In the presence of a catalyst the monomer forms a chain having the repeat unit -CH_2-CH_2-O-.[69, 70] The driving force for the ring opening of cyclic monomers, such as ethylene oxide, is the relief of bond-angle strain and/or steric repulsions between atoms crowded into the center of the ring. Because of these characteristics, the enthalpy change for the ring-opening of ethylene oxide is negative. [70]

The initiators used in cationic ring-opening polymerization are strong protonic acids (e.g. H_2SO_4, CF_3SO_3H, CF_3CO_2H) and Lewis acids used in conjunction with co-catalysts (e.g. $Ph_3C^+PF_6^-$, $CH_3CO^+SbF_6^-$). In the cationic ring-opening polymerization of ethylene oxide, initiation takes place by addition of R^+ to the epoxide oxygen atom to yield a cyclic oxonium ion, which is in equilibrium with the corresponding open-chain carbocation:

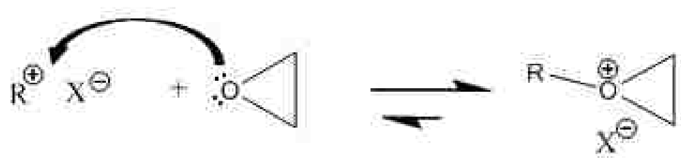

(1.1)

The propagation takes place via ring-opening of the cyclic oxonium ion upon nucleophilic attack at a ring carbon atom by the epoxide oxygen atom of another monomer molecule:

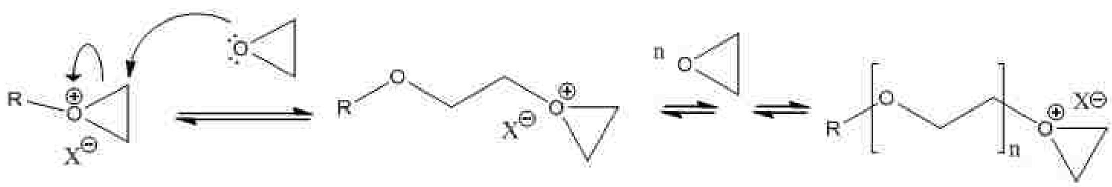

(1.2)

Termination occurs to varying degrees by combination of the propagating oxonium ion with either the counterion or an anion derived from the counterion.

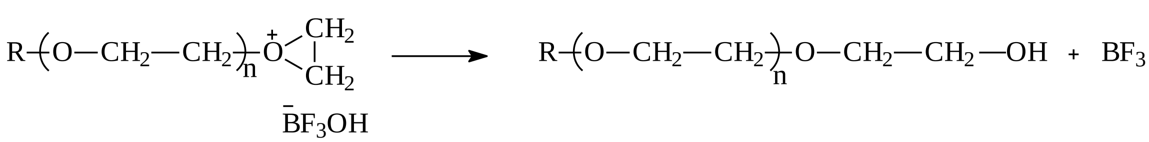

(1.3)

Transfer of an anion from the counterion occurs to varying degrees depending on the stability of the counterion. Thus, counterions such as PF_6^- and $SbCl_6^-$ have little tendency to bring about termination by transfer of a halide ion, while counterions of aluminium and tin have appreciable transfer tendencies; others such as BF_4^- and $FeCl_4^-$ are intermediate in behavior.

Poly(ethylene oxide) is water soluble in all proportions at moderate temperatures.[71] When dissolved in water, PEO is characterized by hydrophilic interactions between the water molecules and the oxygen atoms of the polymer, as well as by hydrophobic interactions between water and the -CH_2CH_2- group.[72, 73] The hydration layers around the PEO chains have been studied[72, 73] and models have been presented that show cage-like structures, where the -CH_2CH_2- groups are shielded from contacting water molecules similarly to hydrated structures.[74] The solubility of PEO in water decreases with increasing temperature, and phase separation occurs above a lower critical solution temperature (LCST) that depends on the polymer molecular weight. [72] Upon continued heating, miscibility will occur again, due to the existence of an upper critical solution temperature (UCST). Introduction of a salt into an aqueous PEO solution changes the phase-separation temperature. This alteration varies considerably in magnitude depending on the kind of electrolyte introduced and on its concentration. [73]

Poly(ethylene oxide) polymers with molecular weights of 10^5-10^6 find applications that take advantage of the high viscosity of their aqueous solutions. This includes flocculation, denture adhesives, packaging films for pesticides and herbicides, thickening of acid cleaners, water based paints, and friction reduction.[69] In the past decade there has been a considerable effort aimed at using ethylene oxide polymers and copolymers, complexed with ionic salts, as the electrolyte in all-solid rechargeable batteries.

1.5 Rheological Overview of PEO-Laponite Dispersions

In aqueous solutions and gels, PEO strongly adsorbs to the charged laponite nanoparticles which may lead to unpredicted rheological behavior. The viscoelastic properties of the gels are strongly dependent on parameters such as the PEO polydispersity index (PDI) and molecular weight (Mw), chemistry and size of laponite, the purity of all components including the water used, the solvent loss during sample preparation, sample mixing time, laponite degradation at low pH, change in pH with time, storage temperature etc. On a nanometer length scale one can imagine that randomized orientation of the polymer covered clay aggregates under flow will disrupt the flow, thus affecting the viscosities. At the same time free, unconfined polymer chains are capable of disturbing the overall flow behavior, where any coiled and entangled PEO chains can counteract shear thinning. The individual polymer-clay interactions of the gels under shear are complex and in general difficult to determine. Changing ionic strength in the gel further complicates understanding of interactions. It has been shown that the water molecules interact strongly with -CH_2CH_2O- units of the PEO through intermolecular hydrogen bonding.[73, 75] Addition of ionic salts to such systems screens the interactions between water and PEO chains to an extent proportional to the amount of salt added.[75] As a consequence of the hydrogen-bonding disruption with addition of salts, the overall coordination of PEO oxygens to the surface of the clay platelets is radically improved, leading to the formation of stronger networks.

Both strain-controlled and stress-controlled shear-flow rheometers have been used by numerous researchers to study the rheological properties of laponite-PEO dispersions. Addition of low molecular weight (Mw) PEO slows the dynamics of clay-gelation, causing a decrease in the elastic moduli, whereas the absorption of high Mw PEO increases the elastic moduli as a result of a PEO-clay network formation.[29] Other rheological results published by Daga et al have shown that addition of laponite to concentrated PEO solutions increases the relaxation times but decreases the elastic moduli.[76] The authors have attributed this behavior to polymer absorption and bridging. Meanwhile, Loiseau et al have studied gels above a critical volume fraction where the elastic moduli increase with a power law of the frequency.[10] Structural information obtained from shear-SANS and flow-birefringence studies by Schmidt et al demonstrated that upon shear the clay platelets orient along the flow direction.[33, 34] Overall, the unique rheological behaviors observed for these systems have been attributed to the formation of transient PEO-laponite networks in which adsorbed polymer chains form bridges between the laponite nanoplatelets, with various degrees of cross-linking. [29, 33, 34, 76]

1.6 Polymer-Clay Multilayered Films

The fabrication of polymer-clay multilayered films from PEO-laponite gels requires the control of polymer dissolution, clay exfoliation and knowledge of polymer-clay interactions on a nanometer length scale.[5, 67, 77] In solution the clay particles can only adsorb a maximum amount of polymer until all the clay surfaces are covered.[41] Under certain conditions, the network formed by the PEO and clay is interpenetrated by a sub-network of interconnecting pores containing excess polymer and water.[41] The mesh size of these networks and the orientation of the clay platelets in solution strongly influence the structure formation of the dried films. Knowledge of structure and viscoelastic properties of the gels is important to film fabrication.

A variety of approaches can be used for the fabrication of polymer-clay films from solution.[78,79] Highly ordered nanocomposite films can be prepared using a layer-by-layer spreading and drying technique. During the drying process the polymer-clay network usually collapses and the platelets are shear oriented, preferentially in the spread direction, as indicated by Figure 1.5. As the water leaves the system clay-clay interactions play a critical role in determining the final orientation in response to shear, favoring the positioning of platelets with the surface parallel to the plane of the film.[77] The reintercalation of clay platelets in films made from exfoliated polymer-clay solutions opens the door to generating supramolecular order and hierarchical structures, which may provide a useful route in the preparation of novel materials.

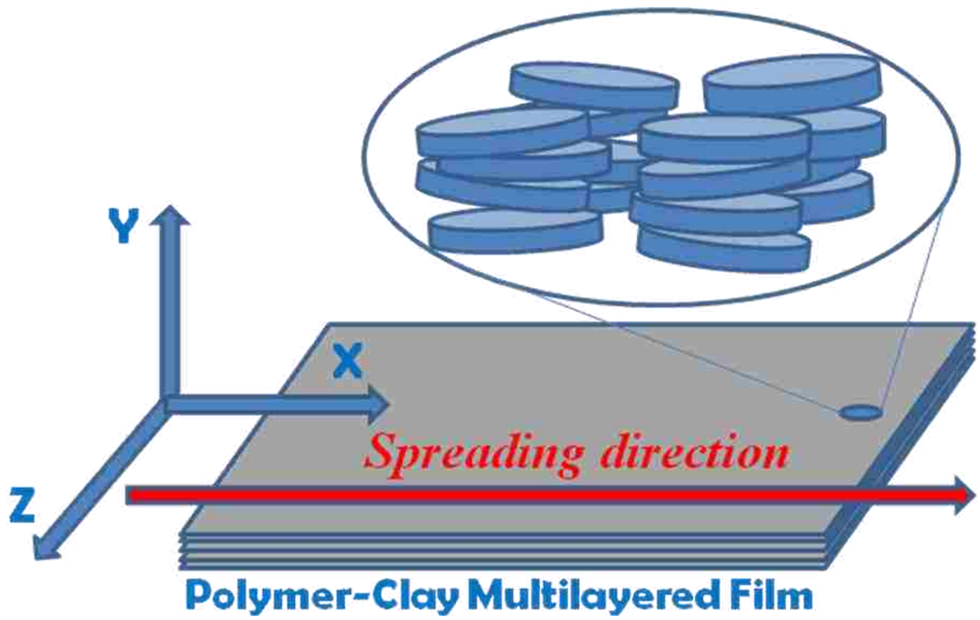

Figure 1.5: A schematic of the general clay platelet orientation in a multilayered polymer-clay nanocomposite film is presented along with the definition of planes.

1.7 Research Objective

Our interest is focused on nanocomposite dispersions with various polymer and clay concentrations, where the entangled poly(ethylene oxide) chains are in a dynamic adsorption-desorption equilibrium with the clay particles and form a network. We aim to understand how ionic strength, sample composition, humidity, polymer Mw, clay size, clay chemistry, and rheological properties of gels influence the structure of nanocomposite thin films, and why some spreading and drying techniques produce multilayered films with micrometer and nanometer layers while others do not. The overall objective of the research presented here is to understand the nanoscopic and microscopic structures that exist in these PEO-laponite and PEO-montmorillonite dispersions and to correlate their shear responses with the final structure and properties of multilayered nanocomposite films prepared from these dispersions. A sequence of shear and elongational rheological measurements is used to provide a more complete physical picture on the structure of polymer-clay hydrogels, while a combination of techniques such microscopy (SEM, AFM, PLOM), XRD, DSC, TGA, DMA is used to study the structure and thermo-mechanical properties of the multilayered nanocomposite films. The principles and methods utilized to study the polymer-clay systems are summarized in **Chapter 2**.

In **Chapter 3**, we aim to provide an efficient method that would help to quantify the orientational levels occurring in polymer-clay dispersions subjected to elongational flow. The extent of internal orientation developed in salt containing Poly(ethylene oxide)-montmorillonite gels is investigated combining shear and elongational rheology methods. Entropic changes indicate that the strength of the transient network present in each gel affects the orientational ability of clay particles and polymer chains. We also want to find how the variation of Hencky strain of the hyperbolic die affects the calculated entropy change of the material.

In **Chapter 4**, the preparation and characterization of polymer-clay nanocomposite gels and films containing various ratios of laponite and montmorillonite are described. The aim is to understand how clays with different chemistry, sizes and surface areas interact with each-other and affect the structure and characteristics of polymer based nanocomposites in the form of both gels and multilayered films. The rheological behavior of the gels is compared to the spreading process and the resulting film structures and properties are analyzed.

In **Chapter 5**, we investigate the multilayered structures of poly(ethylene oxide) montmorillonite nanocomposite films made from solution. The shear orientation of a polymer-clay network in solution combined with simultaneous solvent evaporation leads to supramolecular multilayer formation in the film. The resulting films have highly ordered structures with sheet-like multilayers on the micrometer length scale. We examine the crystallinity of the polymer in the film as well as the overall orientation of the polymer-covered clay stacks.

In **Chapter 6**, the structures and thermal properties of a series of new nanocomposite poly(ethylene oxide)-laponite films are investigated by differential scanning calorimetry and thermogravimetric analysis and complemented by microscopy and X-ray diffraction experiments. The crystalline structures of the nanocomposite multilayered films can be tuned by controlling the composition, polymer Mw and the water content. We also study the concentration, polymer Mw and humidity dependence of polymer crystallinity in selected nanocomposite multilayered films.

Finally, in **Chapter 7**, the data presented are summarized and conclusions are drawn with an outlook to future directions in this field.

CHAPTER 2
METHODS AND PRINCIPLES

2.1 Rheology

Rheology is the study of the deformation and flow of materials.[80, 81] The term rheology comes from the Greek verbs rhei, to flow, and logos, to study. The ability of a system to store deformation energy, under the action of an external force, and to regain the initial shape after being deformed is called *elasticity*. The ability of a material to resist flow and to dissipate deformational energy is measured through the property called *viscosity*.[80] A simple substance, such as water, at a temperature above its freezing point, is a low-viscosity Newtonian fluid of which mechanical properties are specified by its shear viscosity, η.[82] The relationships between stress and deformation of complex fluids like polymers, biological systems, emulsions, suspensions, pastes and other compounds differ from Newton's law of viscosity. Such complex materials are termed *viscoelastic*.[81] In the following section two of the most widely used shearing-flow geometries are described.

2.1.1 Shearing-Flow Geometries

The parallel-disks geometry is usually preferred for the study of small quantities of material. [81] A schematic of the parallel-disks (plates) is presented in Figure 2.1 along with some important parameters. In this schematic R represents the radius of the plates, h is the distance (gap) between the plates and Ω is the constant angular velocity of the disk in rotation. The material to be tested is placed between the two plates and, after adjusting the gap to a known value, is forced to shear by the constant rotation of one plate. If the inertial forces are neglected, the shear strain (γ), shear rate ($\dot{\gamma}$) and shear stress (τ) can be written as described by equations 2.1, 2.2 and 2.3 respectively:[80]

$$\gamma(r) = \frac{r\theta}{h} \qquad (2.1)$$

$$\dot{\gamma}(r) = \frac{r\Omega}{h} \qquad (2.2)$$

$$\tau(r) = \frac{M}{2\pi R^3}\left[3 + \frac{d\ lnM}{d\ ln\dot{\gamma}(r)}\right] \qquad (2.3)$$

In the above equations θ is the angular displacement, r is the distance from the axis of rotation, and M is the measured torque.

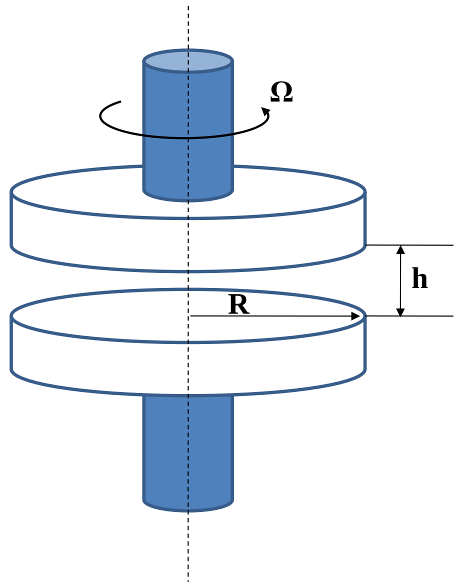

Figure 2.1: Schematic representation of the parallel-disks geometry

Another rheological device very often used in rheology is the cone-and-plate geometry. The main advantage of the cone-and-plate over the parallel-disks is that the former device eliminates the problem with the radial dependence of the shear rate and shear strain.[81] If small angles (Θ_0) are used on the cone-and-plate geometry a homogeneous flow of no radial dependence can be achieved. [82] A sketch of a cone-and-plate device of radius R and an angle Θ_0 is presented in Figure 2.2. If the curvature of the flow lines is neglected when the cone is rotated at a constant angular velocity (Ω), the shear strain (γ), shear rate ($\dot{\gamma}$) and the viscosity (η) in the cone-and-plate flow can be obtained from equations 2.4, 2.5, and 2.6 respectively: [81]

$$\gamma = \frac{\Omega t}{\Theta_0} \tag{2.4}$$

$$\dot{\gamma} = \frac{\Omega}{\Theta_0} \tag{2.5}$$

$$\eta = \frac{3M\Theta_0}{2\pi R^3 \Omega} \tag{2.6}$$

where *t* represents the time and *M* represents the torque on the bottom plate.

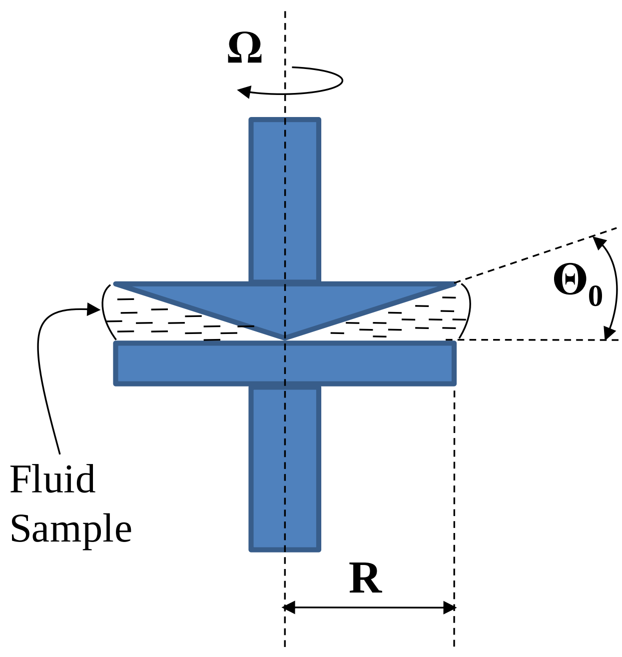

Figure 2.2: Schematic representation of the cone-and-plate geometry

2.1.2 DMA Geometry: Torsion Rectangular Tool

Extensively used in polymer characterization, the principle of dynamic mechanical analysis (DMA) consists in applying an oscillating force to a solid sample and analyzing the material's response to that force. When subjected to such a force, also called stress (σ), a composite material exhibits a deformation or strain, γ. The relationship existent between stress and strain is a measure of material's stiffness or modulus. In DMA, three different moduli can be calculated from the response of the material to the sinusoidal wave: complex modulus, E^*, elastic (storage) modulus, E', and imaginary (loss) modulus, E".[83] The relation between the three moduli is given by the equation $E^* = E' + iE''$, where $i = \sqrt{-1}$.

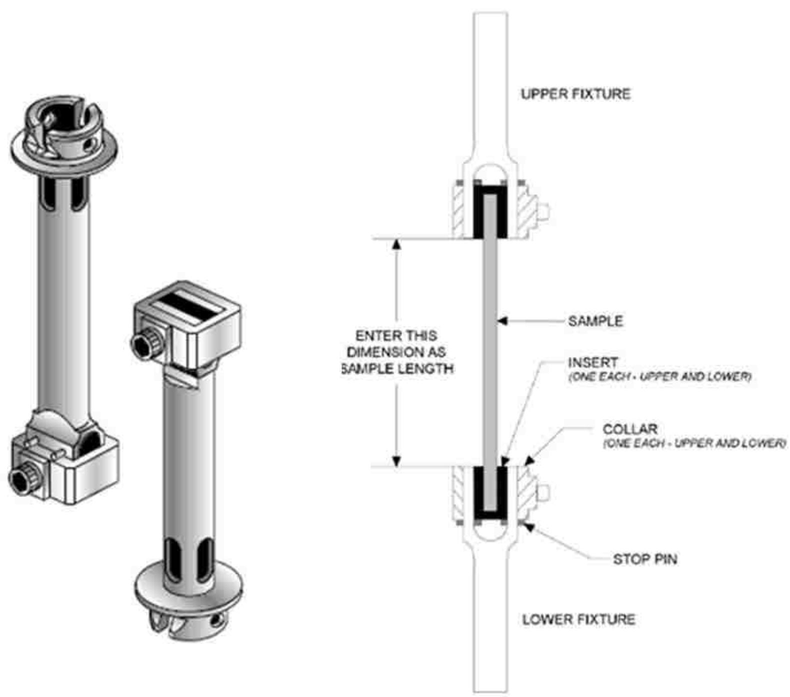

Figure 2.3. The two individual components of the ARES torsion rectangular tool are shown on the left. A schematic of the mounted tool containing the sample is presented on the right. Individual parts of the tool are indicated by arrows (right). *Adapted from ARES user manual*.

Most shear-flow rheometers on the market have the capability of performing dynamic mechanical analysis (DMA) measurements on solid samples. The Rheometrics Scientific

"Advanced Rheometric Expansion System" (ARES) is a sophisticated strain controlled rheometer that has the ability of carrying out DMA measurements. The Torsion Rectangular tool of ARES instrument is used for testing solid materials with high modulus, including thermosets, thermoplastics and elastomers. The sample is held in tension between the upper and lower tool. Several inserts are provided to accommodate samples of varying thicknesses. The geometry setup is presented in Figure 2.3 along with important characteristics of the tool.

2.1.3 Elongational Flow

Even if most rheological measurements are made in shear flow, elongational flow is of critical importance for many industrial processes such as fiber spinning, bubble inflation or coating.[81, 84] Although very important, elongational flow properties are very difficult to measure. The very rapid and large deformation of fluid elements is one of the most important features of the elongational flow. Because of this characteristic the generation of elongational flow becomes a real challenge in industrial processes. The section that follows describes the ACER elongational rheometer along with the hyperbolic convergent die used to generate elongational flow.

2.1.4 Elongational Flow Rheometer

When passing a material through a hyperbolic convergent die in an elongational rheometer, high degrees of order are induced in the material, and the entropy changes, indicative of orientation, can be calculated.[85-87] A schematic showing the advanced capillary extrusion rheometer (ACER) as well as the hyperbolic convergent die is presented in Figure 2.4(a,b).

The main advantage of the hyperbolic convergent die over the cylindrical die is that the elongational strain rate generated by the former is constant throughout the core of the material. As a result of the constant elongational strain the material flows uniformly throughout the core of the hyperbolic convergent die,[88] as indicated in Figure 2.5. On the other hand, the flow generated by the cylindrical capillary die, although unidirectional, is a non-uniform Poiseullie-type flow [81] that does not allow the determination of entropy changes. The Hencky strain, ε_H, of the hyperbolic convergent die is defined as the natural logarithm of the area reduction of the die, as indicated in equation 2.7:

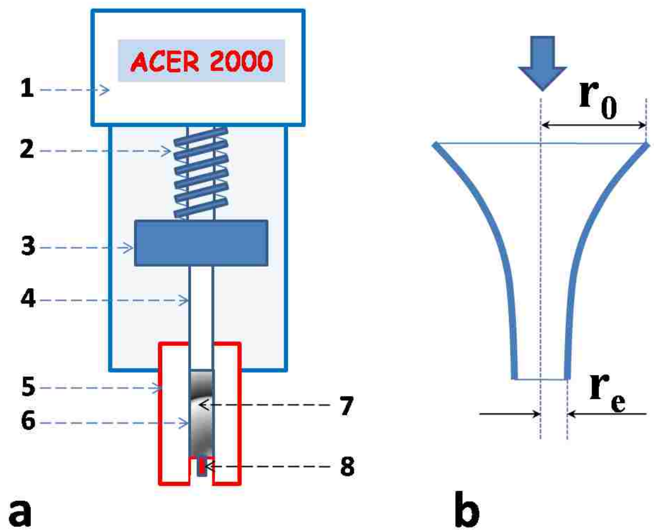

Figure 2.4: a) General schematic of the advanced capillary extrusion rheometer (ACER): 1) drive mechanism, 2) action screw, 3) piston joint, 4) piston, 5) barrel, 6) pressure transducer, 7) polymer-clay gel, 8) hyperbolic capillary die. b) Schematic of the hyperbolic convergent die.

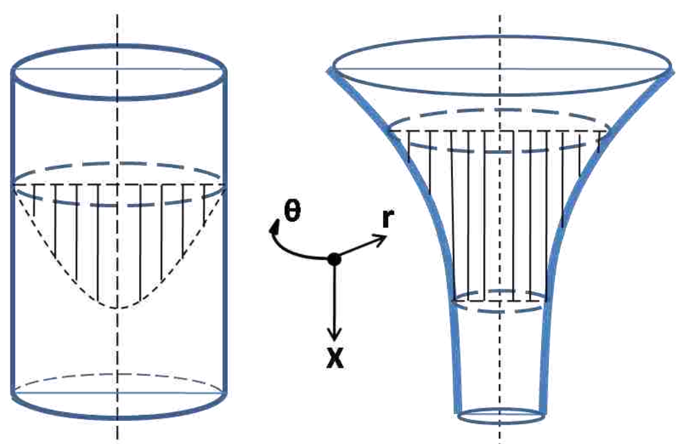

Figure 2.5: Flow profiles in cylindrical (left), and hyperbolic convergent (right) dies. The cylindrical coordinates for capillary flow (**x**, **θ**, **r**) are also indicated, were **x** is the flow direction, **r** is the radius of the die, and **θ** is the angular coordinate.

$$\varepsilon_H = 2ln\frac{r_0}{r_e} \tag{2.7}$$

where r_0 and r_e are the inlet and outlet radii of the die respectively.[86] As demonstrated by Collier et al,[87] the enthalpy change per unit volume, ΔH, necessary for calculating the variation of entropy, can be expressed as:

$$\Delta H = -\varepsilon_H \dot{\varepsilon}(\eta_{ef} - 3\eta_s) \tag{2.8}$$

In equation 2.8 $\dot{\varepsilon}$ is the elongational strain rate, η_{ef} is the effective elongational viscosity, and η_s represents the shear viscosity of the fluid, obtained from shear rheology measurements. Numerical simulations showed that η_{ef} provides a good approximation of η_e,[89] for which reason in this study we consider η_e = η_{ef}. The term η_e represents the elongational viscosity as given by the elongational rheometer. Combining the Gibbs free energy relation, ΔF=ΔH-$T\Delta S$ (at ΔF =0) with equation 2.8, the entropy change, ΔS, indicating the degree of orientation developed in the fluid dispersion can be written as:

$$\Delta S = \frac{-\varepsilon_H \dot{\varepsilon}(\eta_e - 3\eta_s)}{T} \tag{2.9}$$

where T is the temperature expressed in Kelvin.

2.2 Differential Scanning Calorimetry (DSC)

Differential Scanning Calorimetry (DSC) is one of the most widely used thermal analysis techniques.[90] The term “differential” underlines an important characteristic of this technique: two identical sensors are used for measuring thermal changes of the sample and a reference. The concept behind this measurement is to obtain information on the thermal changes in the sample by heating or cooling it next to the inert reference.[91] Because of this differential feature the signal represents entirely the thermal change to be studied, since possible undesired instrumental thermal effects influence equally both sensors.[90] A block diagram of important DSC instrument components is presented in Figure 2.6.

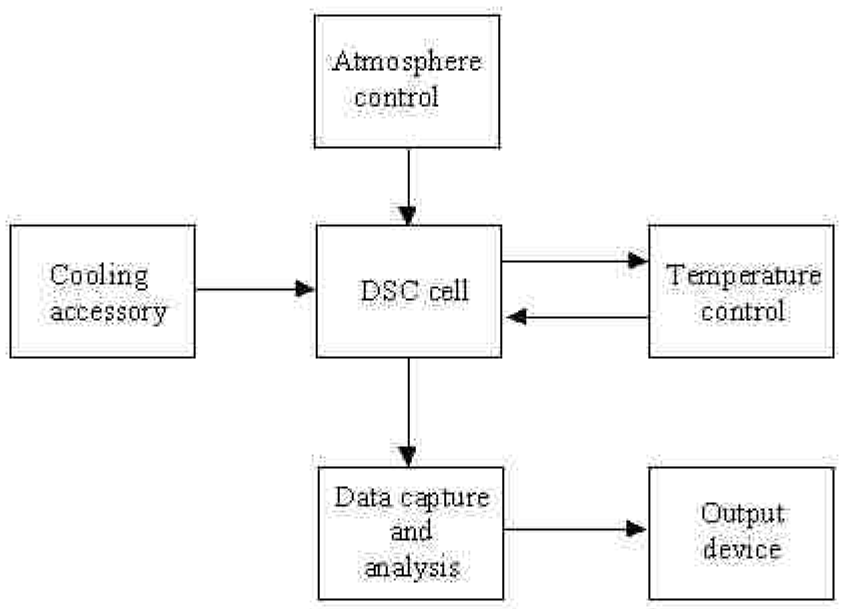

Figure 2.6: Block diagram of important DSC instrument components

Both sample and reference are enclosed in the DSC cell, which incorporates also the temperature sensors and the means of heating. A computer is used to control various parameters of the system, to capture the data and to analyze it. From the practical point of view the main difference between DSC and Differential Thermal Analysis (DTA) consists in the nature of signal produced by the two instruments. For DSC the signal is proportional to the difference in thermal power required to maintain the sample and reference at the same temperature, while for DTA the signal is proportional to the temperature difference between the sample and the inert reference.[91] The more recent DSC has progressively replaced DTA because of its quantitative calorimetric advantages that DTA measurements do not provide.[90]

2.2.1 Enthalpy and Heat

When performing thermal analysis, energy itself is not a convenient function for practical use because it cannot be measured. Instead of it, heat (*Q*), and work (*W*) are measured and they give valuable information about the energy of the system.[90,91] A perfect quantity to use in thermal analysis would be a function of which increase equals the amount of heat Q supplied to the system. The first law of thermodynamics can be written

$$Q = dU - W \tag{2.10}$$

where U represents the internal energy of the system. In equation 2.10 it can be assumed that only volume work is present, resulting

$$Q = dU + p \cdot dV \tag{2.11}$$

At constant pressure the relation becomes

$$Q_p = dU + p \cdot dV + v \cdot dp \tag{2.12}$$

or

$$Q_p = d(U + pV) \tag{2.13}$$

U, p and v are state functions, and they have a fixed value when a certain state of the system is given. Results that $U + pV$ is also a state function.[91] The new state function can be written introducing the name enthalpy and the symbol *H*:

$$Q_p = dH_p \text{ (only volume work)} \tag{2.14}$$

or for a finite process

$$Q_p = \Delta H_p \tag{2.15}$$

Heat capacity, C_p, of a pure substance is defined as an increase in temperature with a unit when the supplied heat increases with a unit. Under certain circumstances (p constant, only volume work) heat is equal to dH . Knowing that H is a function of state

it results that heat capacity is a function of state and can be written as a partial derivative of H with respect to T:

$$C_p = \left(\frac{\partial H}{\partial T} \right)_p \qquad (2.16)$$

If the volume, instead of pressure, is kept constant in equation 2.11 results

$$Q_V = \Delta U_V \qquad (2.17)$$

and thus

$$C_p = \left(\frac{\partial U}{\partial T} \right)_V \qquad (2.18)$$

Knowing that C_p and C_V of a pure substance can never be negative, the supply of heat to a pure substance can never result in a decrease in temperature.[91]

2.2.2 Oscillatory DSC (ODSC)

Oscillatory DSC (ODSC) is often referred to as Modulated Temperature DSC (MTDSC). The technique represented a breakthrough in thermal analysis with a huge impact in the field. Its advantages over conventional DSC have made ODSC to become an indispensable technique in the study of polymeric materials.[90, 92]

$$dQ/dt = C_p(dT/dt) + K(T,t) \qquad (2.19)$$

In this equation Q represents the amount of heat evolved, Cp the thermodynamic heat capacity, T the absolute temperature, t the time, and K is a kinetic response function of any physical or chemical transformation. The DSC-Cp term depends upon both T and t, while the DSC-K term depends only upon temperature, i.e. $K(T,t) = K(T)$. Reversing the sign of the time variable ($t \rightarrow -t$) and multiplying both sides by -1 the following relation is obtained:

$$dQ/dt = C_p(dT/dt) - K(T) \tag{2.20}$$

A comparison of the above equations shows that the *Cp* component is reversible while the kinetic one is irreversible. The heat flow *dQ/dt* depends on the instantaneous heating or cooling rate. The non-deconvoluted oscillating thermogram of LRD60-PEO40 100k presented in Figure 2.7A demonstrates that although the overall heating trend is linear, the oscillating temperature program generates short-term sinusoidal variations. The composite data is separated into three different signals (Figure 2.7B) by applying a Fourier transform. The three different signals are the deconvoluted or normal DSC (*DSC-D*), the reversible DSC (*DSC-Cp*), and the nonreversible DSC (*DSC-K*). Between the three components the following relation applies:

$$[DSC\text{-}D]=[DSC\text{-}Cp]+[DSC\text{-}K] \tag{2.21}$$

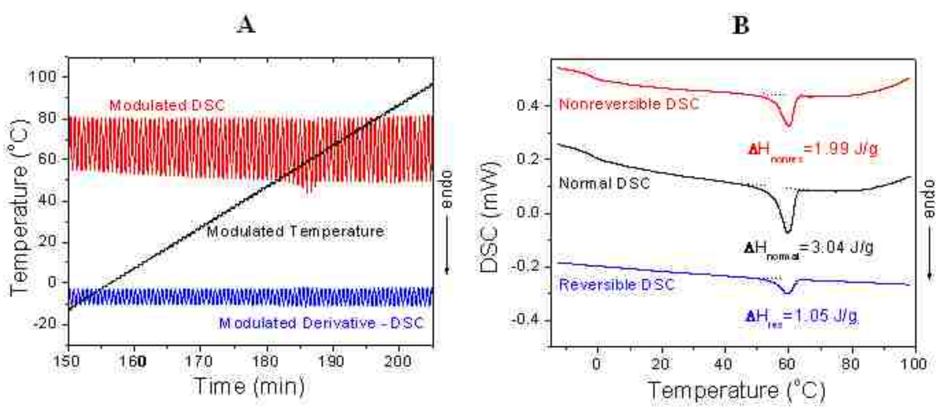

Figure 2.7: Complex ODSC thermogram (A) and resolved components of the ODSC thermogram (B) of LRD60%-PEO40% 100k (2^{nd} heating run)

In ODSC the ability of the sample to follow the temperature oscillation greatly depends on the sample size and the period of modulation. [92] The need for a careful selection of the period and amplitude of modulation makes the choice of experimental conditions far more critical in ODSC than in conventional DSC. In general, during the thermal event of interest 4-6 cycles are desirable. The experimentally measured modulated heating flow and the modulated heating rate can be used to judge at the end of experiment if the chosen parameters are the optimal ones. A smooth modulation should be obtained when the modulated heat flow is plotted against temperature.

2.3 Thermogravimetry (TG)

Thermogravimetry (TGA or TG) is an experimental procedure in which the mass change of a substance is measured and recorded as a function of temperature when a rigorously controlled temperature programme is applied.[90,93] When a volatile component is lost during the experimental procedure the mass loss can be observed. Results are normally presented as mass, *m*, versus temperature, *T*, (Figure 2.8A) although representations of mass versus time, *t*, are also possible. The weight loss appears as a step in the curve, as can be seen in Figure 2.8A. Even if most of the sample's mass is lost around one specific temperature the shape of the curve appears sigmoid, because some reactions start before the main reaction temperature.

Another possibility of presenting the thermogravimetric data is to plot the derivative curve of the original data as a function of temperature (Figure 2.8B). This Derivative Thermogravimetry (DTG) plot gives information about overlapping reactions or about slow reactions concurrent with fast reactions that may take place during the heating process. Many TG experiments are carried on raising the temperature at a constant rate. Such experiments are known as non-isothermal or scanning. An alternative isothermal measurement is also possible when the temperature is maintained constant and the mass loss (or gain) is observed at a function of time for the chosen temperature. This type of measurements is often used in kinetic studies. [93]

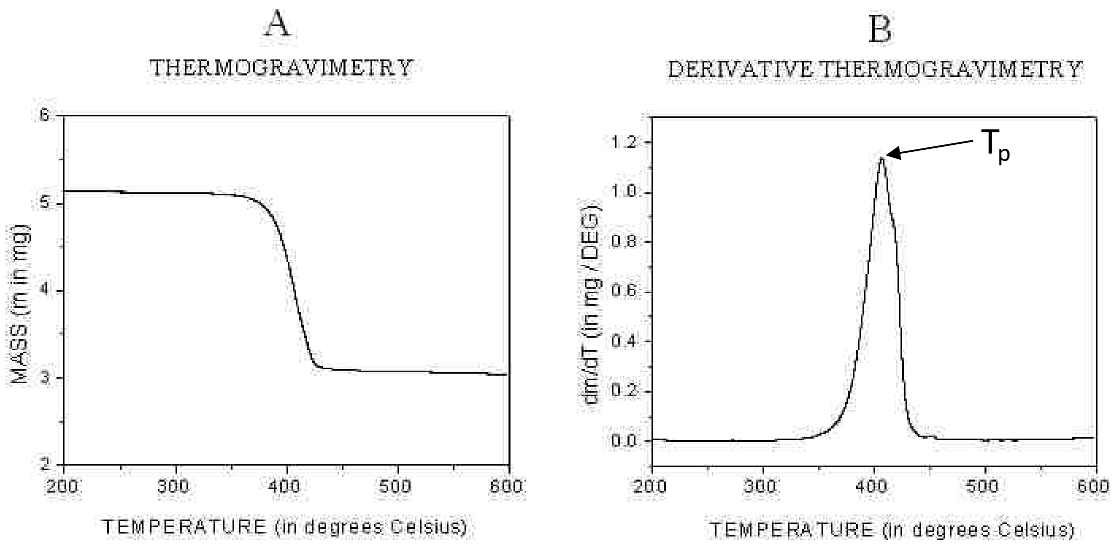

Figure 2.8: Typical thermogravimetric results, (A) TG curve, (B) DTG curve

2.3.1 Effect of Experimental Variables

Because a reaction in the solid state is relatively slow compared to gas or solution reactions, a thermogravimetric trace of such a transformation may be seen to occupy a wide span of temperature. Although other factors may be involved in some cases, the rate of reaction is often controlled by the rate of heat transfer to or from the reaction interface.[90] Since the reaction evolves in time and the temperature always increases with respect to time, a graphical representation will show the reaction covering a spread of temperature. Because of this spread of reaction over time a careful definition of "decomposition temperature" must be elaborated.[93]

Figure 2.9 presents a typical thermogravimetric trace where mass loss is involved. A very fast and easy way to define the decomposition temperature would be to consider the peak temperature T_p that can be observed in a DTG curve (shown in Figure 2.8B). However, this T_p does not indicate the start of reaction when bonds start to break in the sample; this temperature is in fact only the point where the reaction is the fastest. For this reason heat flow properties, sample size and packing will influence the value of T_p.

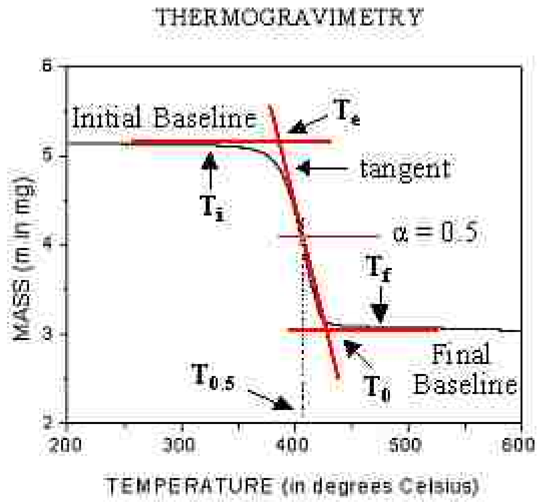

Figure 2.9: Definition of decomposition temperature on a TG curve.

The initial temperature of decomposition, or the onset temperature, is represented with T_i in Figure 2.9. T_i depends on the sensitivity of the thermobalance and it may be promoted by traces of impurities in the system that may start decomposing ahead of the main reaction. An extrapolation of the onset point will better define the beginning of the reaction, and this temperature point is marked with T_e in the figure. In order to find T_e the tangents to the curve at the baselines have to be sketched followed by the tangent to the steepest part of the curve. T_e will be very different from T_i for a reaction that starts slowly and speeds up later. For this reason, sometimes the start of the reaction is better indicated by the temperature $T_{0.05}$ where the fraction reacted $\boldsymbol{\alpha}$ is 0.05.[90]

For kinetic studies the reaction temperature may also be defined as the temperature when the reaction is half over. When the fraction reacted is $\alpha = 0.5$ the reaction temperature is named $T_{0.5}$. Final temperature T_f and the extrapolated offset temperature T_0 are also marked in the figure to show the complete temperature range for reaction. Just like T_i, T_f is very difficult to pick up accurately since it depends on the sensitivity of the balance and on the amount of "noise" seen.[90,93]

2.3.2 Glass Transition Temperature (Tg)

The temperature at which the amorphous domains of a polymer undertake the characteristics of the glassy state is called glass transition temperature, *Tg*.[68, 69] When a polymer is subjected to a decrease in temperature below its *Tg*, the long-range chain motions disappear and the polymer becomes very rigid and brittle. At this point if the system is provided with enough thermal energy the polymer segments slowly start moving and a transition from the glassy state to a rubbery-like state occurs.[70] This transition is an important feature of polymers since it marks dramatic changes in the polymer properties, such as hardness and elasticity. The properties changes are completely reversible, however, since they depend on the molecular motion of the system, and not on the polymer structure. Besides hardness and elasticity, changes can be observed also in the specific volume, the modulus, the heat capacity, and the refractive index of a polymer when a transition from the glassy state to a rubbery-like state occurs.[71]

Certain factors such as chain flexibility, molecular structure, molar mass, branching and cross-linking influence *Tg*. High *Tg* values are found when the mobility of the chains is low and the rigidity is high. High secondary forces decrease mobility of the amorphous polymer leading to high *Tg* values.[69] Poly(ethylene oxide) PEO, of which repeating unit is [-CH_2-CH_2-O-], is a polymer with rather flexible chains since it does not contain any cyclic structures in the main chain or any bulky side groups. Although oxygen is a polar group, strong secondary forces do not characterize PEO. For these reasons PEO is one of the polymers with low, negative *Tg* (-66°C).[68]

The determination of glass transition temperature of amorphous polymers was found to be dependent on the cooling/heating rate used in the experiment. Faster cooling rates will result in higher *Tg* values of the polymer in discussion. Figure 2.10 shows the dependence of Tg on the cooling rate as resulted from a dilatometric experiment. In this experiment the polymeric sample is placed in a glass bulb, which is filled with mercury so that the sample is completely immersed in the liquid. The glass bulb is connected to a capillary tube that will easily measure changes in the height of mercury in the capillary when changes in the specific volume of the polymer will appear as a result of temperature modification. Similar results of the dependence of *Tg* on the cooling/heating rate can be obtained using diverse methods that measure other properties of polymers.

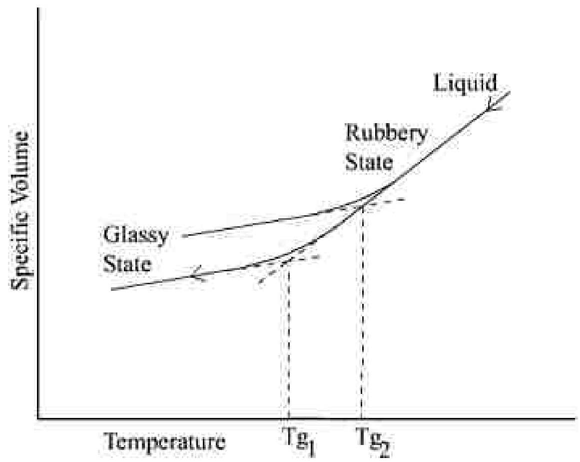

Figure 2.10: Dependence of glass temperature Tg on the cooling rate. *Adapted from: http://plc.cwru.edu/ tutorial/enhanced/files/polymers/therm/therm.htm*

2.3.3 Melting (T_m) and Freezing (T_f) Temperature

The melting temperature *Tm* of a polymer is the temperature at which the crystalline domains start melting. The size and the perfection of the crystallites in the polymer will influence the range of temperatures that will cover melting of the polymer.[68,69] This range of temperatures is a useful indication on the sample crystallinity. Completely crystalline polymers will exhibit only a *Tm*, while completely amorphous polymers will show only a *Tg*. However polymers are never perfectly crystalline because of crystallization defects and varying sizes of the crystallites.

Semicrystalline polymers, containing both crystalline and amorphous domains, will show both *Tm* and *Tg*.

In the vicinity of *Tm* the segmental motion is too great to allow the formation of stable nuclei. As the temperature drops from *Tm* the translational, rotational, and vibrational energies and the diffusion rate of the macromolecules decrease, giving the chains the possibility to rearrange and form crystallization nuclei.[68] This means there will be an optimal temperature of crystallization also called freezing temperature T_f. Because crystallization is a very complex process that involves formation of nuclei and the growth of crystalline areas the freezing temperature will also be an interval of temperatures.

When cooling a crystalline material (1) from melt an abrupt change in specific volume takes place when T_f is reached, as Figure 2.11 shows. As opposed to this case, no abrupt change in the specific volume can be seen when an amorphous material (2) is subjected to cooling form the liquid state. However, a change in slope of the specific volume curve can be noticed when *Tg* is reached. The apparatus used to obtain this information was described when Figure 2.10 was discussed.

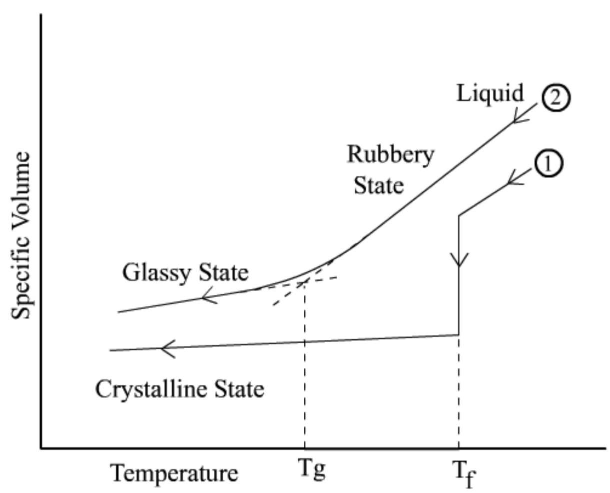

Figure 2.11: A comparison of the melting behaviors of a crystalline material (1) and an amorphous material (2). *Adapted from http://plc.cwru.edu/tutorial/enhanced/files/polymers/therm/therm.htm)*

The *Tm* of crystalline polymers is generally affected in the same manner as *Tg* by factors like molecular symmetry, structural rigidity and secondary forces of polymer chains.[69] High *Tm* values will be found in rigid polymers and in polymers with high secondary forces due to polarity or hydrogen bonding. Depending on their number and identity, substituents will affect differently the *Tm* values. Because poly(ethylene oxide) is not characterized by a tightly packed structure, a high rigidity or by strong secondary forces the Tm value of PEO is quite low (66^{o}C).[69, 71]

2.4 X-Ray Diffraction (XRD)

X-ray diffraction is a technique used especially in crystallography in which an X-ray beam is projected against a crystalline structure and the pattern produced by the diffraction of rays through the closely spaced grate of atoms is recorded and analyzed in order to characterize and identify the structure in discussion.[94,95] This technique is able to provide information about “volume” properties of the entire population of a crystalline sample, information that can be averaged over as many as probably 10^{11}–10^{12} unit cells or billions of crystals. Being a part of the electromagnetic spectrum, X-rays exhibit the characteristics of both waves and particles.[94] When an electromagnetic beam falls on an atom, three processes may occur: the beam’s energy will be partly transmitted, partly refracted and scattered, and partly adsorbed. Just like discrete particles, the photons can bounce and transfer momentum, but they also have measurable wavelengths and they can be diffracted by patterns of appropriate size, displaying characteristics of waves.[96]

X-radiation can be produced in an X-ray tube by emittion of electrons, from a tungsten filament (the cathode), electrons that are accelerated in vacuum and forced to strike a metal target (the anode). The resulted X-radiation is of two different variety types: one type is characterized by a broad, continuous spectrum of wavelengths, called white or continuous radiation, and the other type, called characteristic radiation, is characterized by very sharp peaks of discrete wavelengths, and they are typical to the material used to serve as anode.[96, 97]

2.4.1 Interference of waves

When two or more waves superimpose a new wave is formed. This resultant wave depends on the frequency, amplitude and relative phase of the two or more initial waves.[95] The interference can be constructive, when the two rays are in phase, or destructive when the two waves are out of phase. Figure 2.12 shows an example of constructive and destructive interference, where λ is the wavelength and a is the amplitude vector of the rays.

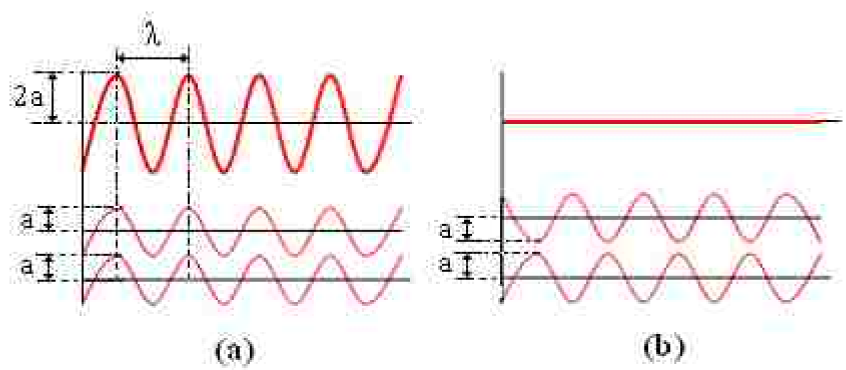

Figure 2.12: Summation of waves for constructive interference (a) and for destructive interference (b).

In all the cases the amplitude vectors of the two or more waves add to create the amplitude of the final wave. When the two rays are in phase (Figure 2.12a), both vectors have the same sign, and the resultant amplitude is given by the sum

$$A = 2a = |a + a| \tag{2.22}$$

When the two waves are 180° out of phase (Figure 2.12b), the amplitude vectors bear different signs, and the amplitude of the final ray will be:

$$A = |a - a| = 0 \tag{2.23}$$

A diffracted beam is produced only when constructive interference occurs. To be practically useful in X-ray diffraction, a diffracted beam must be composed of an enormous number of mutually constructive rays.[96, 97]

2.4.2 Bragg's Law

The law was developed in 1913 by the English physicists Sir W.H. Bragg and his son Sir W.L. Bragg in order to explain why the X-ray beams were reflected at angles of certain degrees of incidence by the faces of the crystals, when irradiated.[95] The observation is in fact an example of X-ray wave interference also known as X-ray diffraction, and it served as a proof for the periodicity of the atomic structure of crystals.

The situation for two planes of atoms reflecting an X-ray beam at relatively large angles is presented in Figure 2.13. The two rays *1* and *2* travel towards the ray of atoms in phase. Rays *1`* and *2`* have to be also in phase in order to have a diffracted beam. *R* and *S* are the two planes of atoms in discussion, and *X-X`* and *Y-Y`* segments represent the wavefronts. The normal *N* to the reflecting plane, the incident beams *1* and *2*, and the diffracted beams *1`* and *2`*, are all in the same plane. As can be seen ray *2* travels a longer distance than ray *1* to reach the wavefront *Y-Y`*. This extra distance is marked in the figure with dashed line and is given by the sum of the segments *AB* and *BC*. If the two rays *1* and *2* are to arrive at *Y-Y`* in phase, than the distance *AB + BC* has to equal some whole number or integer of wavelengths. In order to derive the Bragg's law few variables have to be defined. The distance between atoms *Z* and *B* is in fact the distance between atomic layers in the crystal and is commonly indicated with ***d*.** θ is the angle of incidence, λ is the wavelength of the incident X-ray beam and *n* represents an integer, where

$$n\lambda = AB+BC \qquad (2.24)$$

Using trigonometry in the right triangle *ABZ*, *d* and θ can be related to the distance (*AB* + *BC*). The distance *AB* is opposite θ so,

$$AB = d\sin\theta \qquad (2.25)$$

But AB = BC in which case equation 2.24 becomes

$$n\lambda = 2AB \qquad (2.26)$$

Substituting equation 2.25 in equation 2.26 results,

$$n\lambda = 2d\sin\theta \qquad (2.27)$$

Equation 2.27 is in fact the Bragg's law and is of crucial importance for the use and understanding of X-ray diffraction. [94, 96, 97]

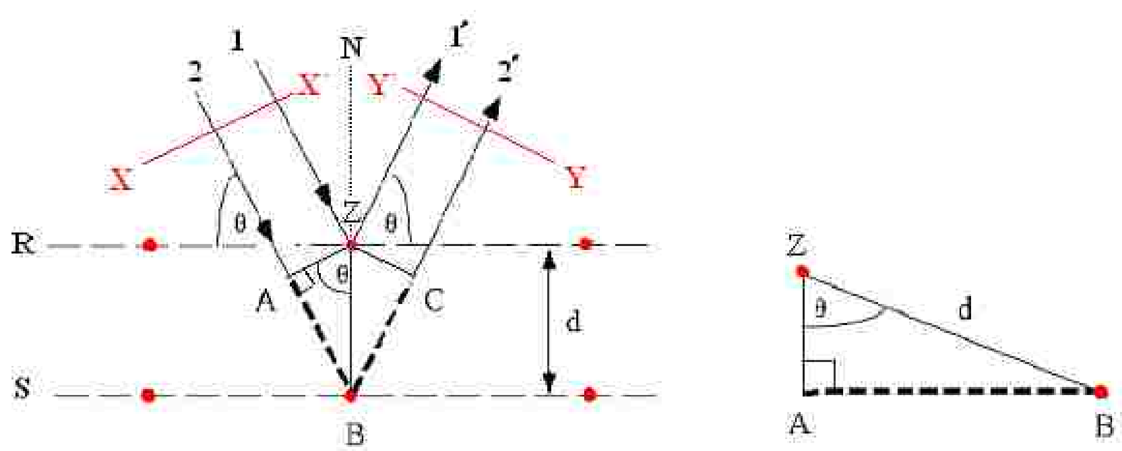

Figure 2.13: Diffraction from two rows of atoms illustrating Bragg's law. *Adapted from: http://www.eserc.stonybrook.edu/ProjectJava/Bragg/*

2.5 Scanning Electron Microscopy (SEM)

Scanning Electron Microscopy (SEM) is a powerful technique that allows the observation and characterization of a variety of organic and inorganic materials from the nanometer (nm) to the micrometer (µm) scale.[98] The possibility of obtaining greatly detailed three-dimensional-like images of the studied surfaces makes SEM one of the most popular techniques available today.[99]

In a typical SEM the area to be analyzed is irradiated with a beam of electrons, usually emitted from a tungsten cathode, beam that may be driven across the surface of the sample in order to find relevant spots for analysis. Because the sample needs to be electrically conductive it is coated usually with gold, palladium or iridium, although the use of amalgams of these metals is also possible.[100] As a result of the interaction between the sample and the primary electrons the signal is produced in the form of secondary electrons, backscattered electrons and some characteristic X-rays.[98, 99] In this way important information is obtained regarding surface topography, crystallography and the composition of the sample. Due to large depth of the field of secondary electrons the image appears to be three dimensional as can be observed in Figure 2.14.

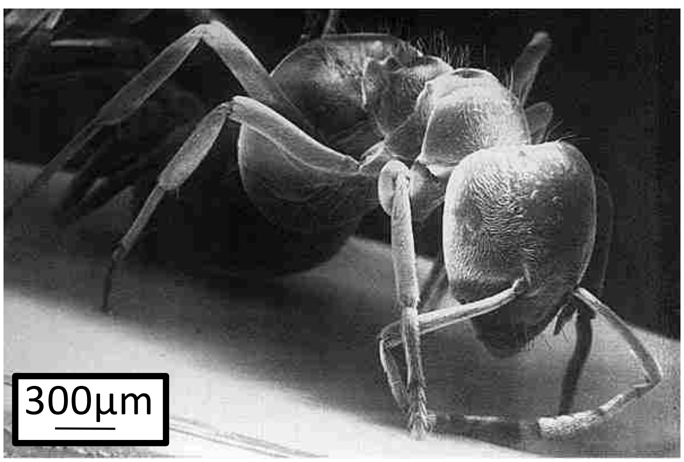

Figure 2.14: Three-dimensional appearance of an ant as detected by SEM. *Adapted from:* *http://mse.iastate.edu/images/microscopy/ant.jpg*

2.6 Atomic Force Microscopy (AFM)

Atomic Force Microscopy is a technique that provides information about surfaces with an unprecedented clarity. The microscope uses a physical probe to scan the specimen line by line, and the probe-surface interactions are recorded as a function of position.[101] The field of view ranges from the atomic and molecular scale up to around 125μm, and the topographic contrast provided is superior to that of the SEM. Sufficiently rigid surfaces can be investigated either in air or in a liquid media. Large samples can be placed directly in the microscope without cutting. No metallic coating of the surface is necessary in AFM, since the sample does not have to be electrically conductive.[102]

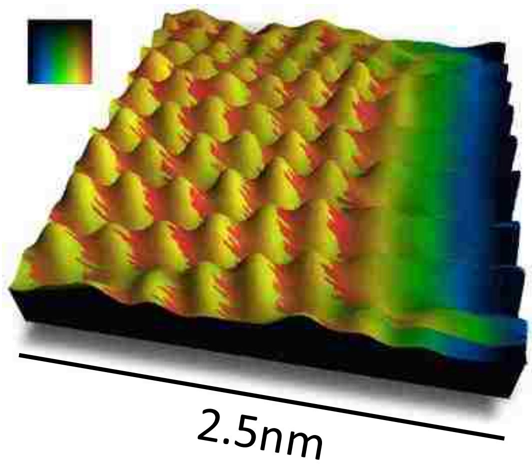

Figure 2.15: 2.5 x 2.5 nm simultaneous topographic and friction image of highly oriented pyrolytic graphic; The bumps represent the topographic atomic corrugation, while the coloring reflects the lateral forces on the tip. The scan direction was right to left. *Adapted from: http://stm2.nrl.navy.mil/how-afm/how-afm.html*

Besides imaging the surfaces, atomic force microscopes can measure the force at the nano-newton scale, and also can provide quantitative height information as shown in Figure 2.15. While the up and down deflection of the cantilever is used to obtain topographic images, friction-imaging uses the torsional deflection of the probe. An incorrect choice of the probe tip for the required image resolution can lead to image artifacts.[101, 102]

2.7 Polarized Light Optical Microscopy (PLOM)

Unlike regular optical microscopy, polarized light optical microscopy offers useful information about structure and composition of materials exploiting the optical properties of anisotropy.[103] More precisely the technique is based on the capacity of isotropic materials to split the light beams and to divide the rays into two different components situated in perpendicular planes. As the split light components are reunited along the optical path due to birefringence of the analyzed material, the microscope senses the occurrence and creates a characteristic image on the screen. The samples can be analyzed in air or in liquid medias and the area of interest can be magnified one hundred to one thousand times. Modern instruments are equipped with digital cameras that offer the possibility of recording pictures or movies of the analyzed materials. An example of a picture recorded with a camera attached to an optical microscope is presented in Figure 2.16. This image shows the formation of a liquid crystalline phase in a cellulose solution sheared between two microscope-slides.

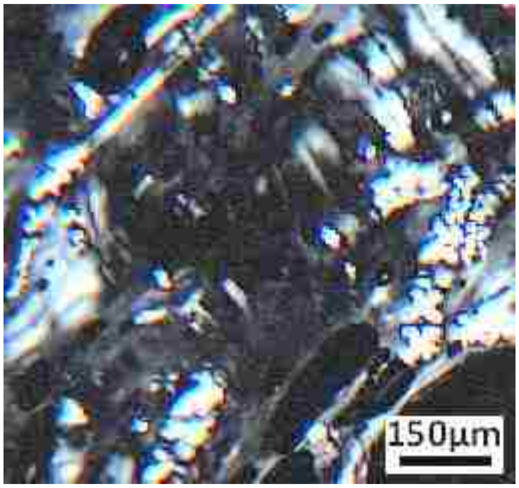

Figure 2.16: Anisotropic phases of a cellulose solution observed under cross polarizers. *Unpublished data*

CHAPTER 3
ORIENTATIONAL EFFECTS IN PEO-MONTMORILLONITE DISPERSIONS SUBJECTED TO ELONGATIONAL FLOW*

In this chapter the extent of internal orientation developed in salt containing poly(ethylene oxide)-montmorillonite gels is investigated combining shear and elongational rheology methods. Entropic changes indicate that the strength of the transient network present in each gel affects the orientational ability of clay particles and polymer chains. The Hencky strain of the dies used in the elongational experiments is varied to observe the variation in the calculated entropy change of each material.

3.1 Experimental Procedures

3.1.1 Sample Preparation

In this study montmorillonite clay, cloisite Na^+ (CNA), (a gift from Southern Clay Products) was used as received without any further purification. Poly(ethylene oxide) (PEO) with a molecular mass of 1000 kg/mol (Mw/Mn=1.5) was used as received from Polysciences Inc. Exfoliated gels were prepared by the addition of PEO and montmorillonite to deionized water, followed by continuous mixing for 4 days. The components (PEO, CNA, salt, and water) were introduced in a 250 mL round-bottom flask. The dispersion pH was controlled by addition of NaOH (pH ≈ 9) to ensure a good stability of the clay. An overhead mixer was employed to mix each sample. The round-bottom flask was immersed in a water bath, as presented in Figure 3.1, at a temperature of 50 ^{o}C in order to decrease the viscosity of the systems and increase the rpm of the mixer. After 4 continuous days of mixing the dispersions appeared completely

* Reproduced in part with permission from Macromolecular Materials and Engineering, E. A. Stefanescu, S. Petrovan, W. H. Daly, and I. Negulescu, Elongational rheology of polymer/clay dispersions: Determination of orientational extent in elongational flow processes, **2008**, 293, 4, 303-309, Copyright © 2006 Wiley-VCH Verlag GmbH & Co. KGaA, Weinheim

homogeneous to the eye (no flocculated particles or clusters). All PEO-montmorillonite gels were self-supporting, as indicated in Figure 3.2. The exact sample preparation was used for all samples. Following this procedure three gels/dispersions (150 mL each) with a composition of 6% montmorillonite (CNA) and 4% PEO (90%water) were produced containing three different metal salts: NaCl, LiCl, and Li_2SO_4. The salt amounts were adjusted in the gels to ensure a ratio of EO/Na^+=8, and EO/Li^+=8 respectively (where EO represent the ethylene oxide groups). All gels were stored less than 3 days prior to determination of the shear and elongational viscosities in order to prevent the occurrence of any possible time-dependent transitions in the systems.

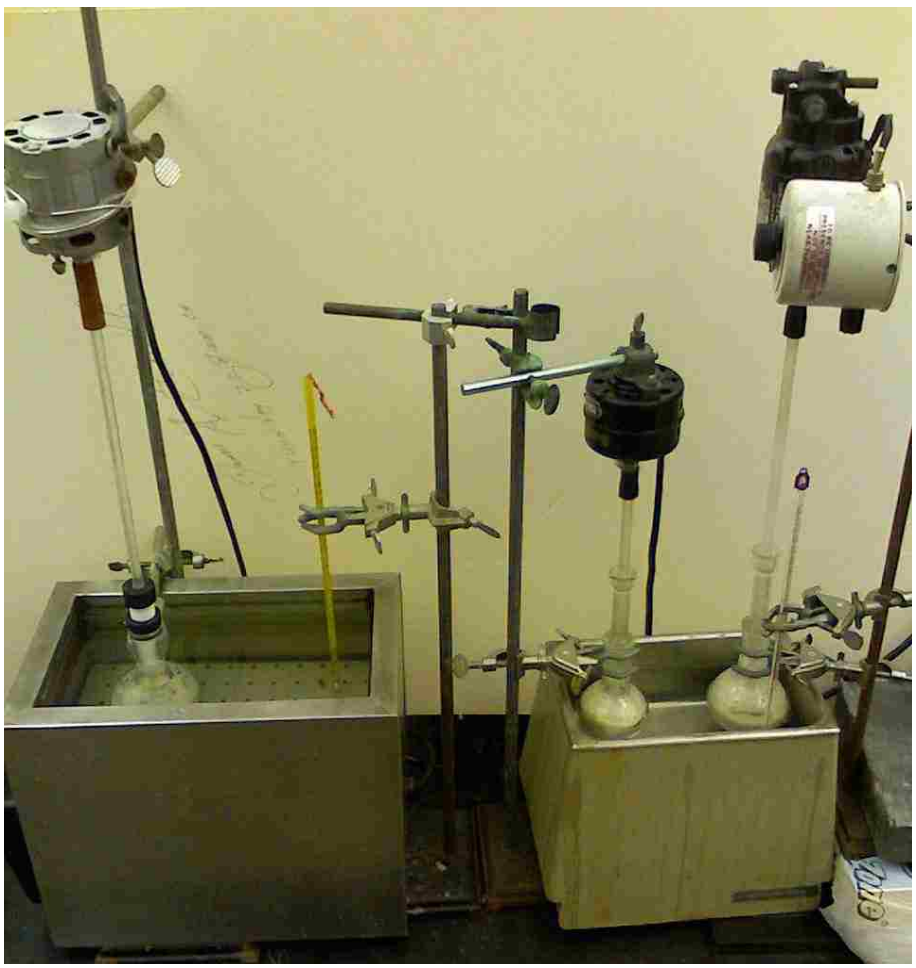

Figure 3.1: The setup used for the preparation of CNA6%-PEO4% dispersions. The three round bottom flasks are immersed in two water baths, of which temperature is recorded using mercury thermometers. On top of each flask there is an overhead mixer.

Figure 3.2: A picture showing the 3 vials containing the CNA6%-PEO4% dispersions before (left) and after (right) inversion. As observed on the right, at rest all gels are self supporting (no flow even after 24 hours)

3.1.2 Shear Flow and Oscillatory Experiments

Shear flow and oscillatory measurements were performed on a TA Instruments AR-1000 stress controlled rheometer. Measurements were obtained using a cone-and-plate geometry with a diameter of 40 mm, a gap of 27 μm, and a cone angle of $1^{o}56'$. The instrument was equipped with a solvent trap to prevent water evaporation. All shear flow and oscillatory measurements were conducted at a temperature of 25 ^{o}C. To check for reproducibility of results, duplicate measurements were taken with a new sample. Steady state values were reproduced within a relative uncertainty of ≈ 5 %.

3.1.3 Elongational Flow Experiments

The determination of the uniaxial elongational rheological properties of nanocomposite gels was measured using a Rheometric Scientific Advanced Capillary Extrusion Rheometer (ACER 2000) by replacing the capillary cylindrical die with hyperbolic converging axis-symmetric dies. These electrodischarge-machined hyperbolic convergent conical dies were designed to generate a constant elongational strain rate throughout the core of the material. For the purpose of this work three conical dies were used with Hencky strains of 5, 6, and 7. The elongational strain rates were achieved in steps of ram speeds, with each strain rate corresponding to a fixed ram speed. All elongational rheological measurements were conducted at a temperature of 25 ^{o}C. Duplicate measurements showed excellent reproducibility, with a relative uncertainty of ≈ 5%.

3.2 Results and Discussion

3.2.1 Elongational Flow Experiments

Figure 3.3a&b shows the elongational viscosity of salt containing CNA-PEO nanocomposite gels as a function of elongational strain rate at a temperature of 25^{o}C. It can be observed that elongational viscosity values of all dispersions gradually decrease with increasing the elongational strain rate. In Figure 3.3a is presented the elongational viscosity of gels containing three different salts at a Hencky strain $\varepsilon_H = 5$. The results suggest that gels containing Li^+ salts exhibit elongational viscosities higher than gels containing equivalent amounts of Na^+ salts of the same counter-ion (in this case Cl^-). Furthermore Figure 3.3b reveals that elongational viscosities of polymer-clay dispersions increase with increasing the Hencky strain of the capillary die. Due to the relatively large amount of sample needed in the rheological experiment it is difficult to perform elongational viscosity measurements of polymer-clay nanocomposite dispersions at strain rates higher than 100 s^{-1}. This problem becomes even more severe when dies of small Hencky strain (smaller than $\varepsilon_H = 6$) are used, and/or gels with a strong shear thinning behavior are studied.

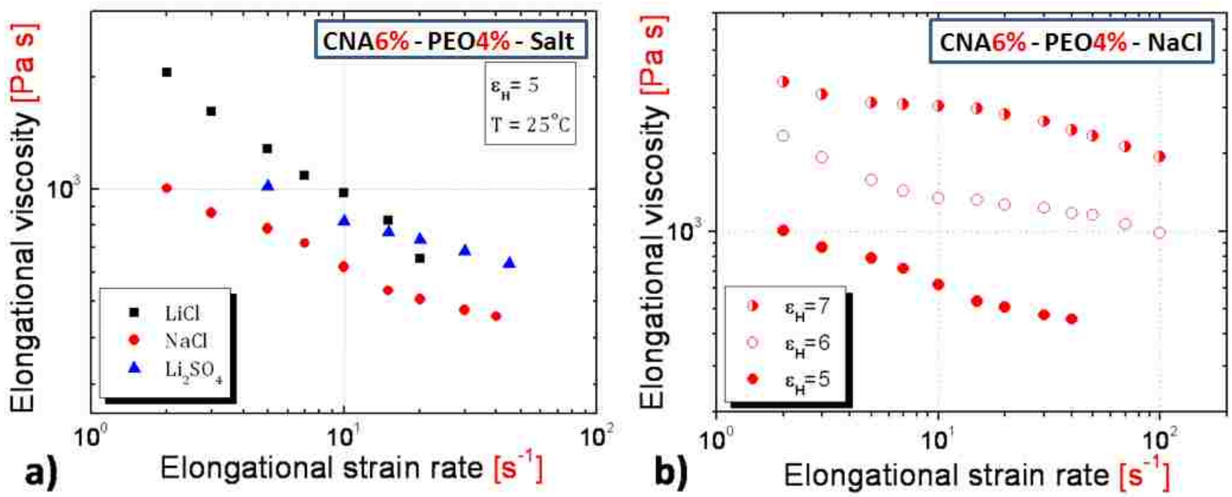

Figure 3.3: Elongational viscosity of: a) CNA-PEO gels containing different salts at Hencky strain ε_H =5, b) CNA-PEO gel containing NaCl at three different Hencky strains. Relative uncertainty for the measurements is ≈ 5%.

3.2.2 Shear Flow and Oscillatory Experiments

Shear viscosity values of salt containing CNA-PEO nanocomposite gels as a function of shear rate are presented in Figure 3.4a. Note that the range of shear rates presented in Figure 3.4a is equivalent to the range of elongational strain rates presented in Figure 3.3a, to allow calculation of entropy changes. Shear thinning behavior is observed over the entire range of shear rates studied, with a linear relationship between the $log(\eta_s)$ and $log(d\gamma/dt)$ (indicated by the solid lines on most of the shear rate range, except at higher values for NaCl and Li_2SO_4 samples - Figure 3.4a). This indicates that over the shear rate dependent region the solutions are power law fluids. The power law relation can be expressed as $\eta_s = m(d\gamma/dt)^{(n-1)}$, where η_s is the shear viscosity (Pa*s), $d\gamma/dt$ is the shear rate (s^{-1}), m is the consistency index, and n is the power law index and has values comprised between 0 and 1. Higher degrees of shear thinning result in n values closer to 0, while n values closer to 1 indicate a dispersion behavior approaching the one of Newtonian fluids. [82] Power law indexes were found to be n = 0.5(+/-0.02) for dispersions containing LiCl and NaCl, and n = 0.3(+/-0.02) for dispersions containing Li_2SO_4.

Frequency dependent oscillatory shear experiments of the three polymer-clay nanocomposite dispersions are presented in Figure 3.4b at 25 ^{o}C. All data were taken at a strain percent of 1%. The storage modulus (G') of the samples is larger than the loss modulus (G") for the entire range of studied frequencies, indicating elastic behavior. All samples show frequency dependence of the storage modulus, G', which increase with increasing frequency. No crossover frequency, indicating a change from an elastic solid-like behavior to a viscoelastic one, could be observed for any of the samples.

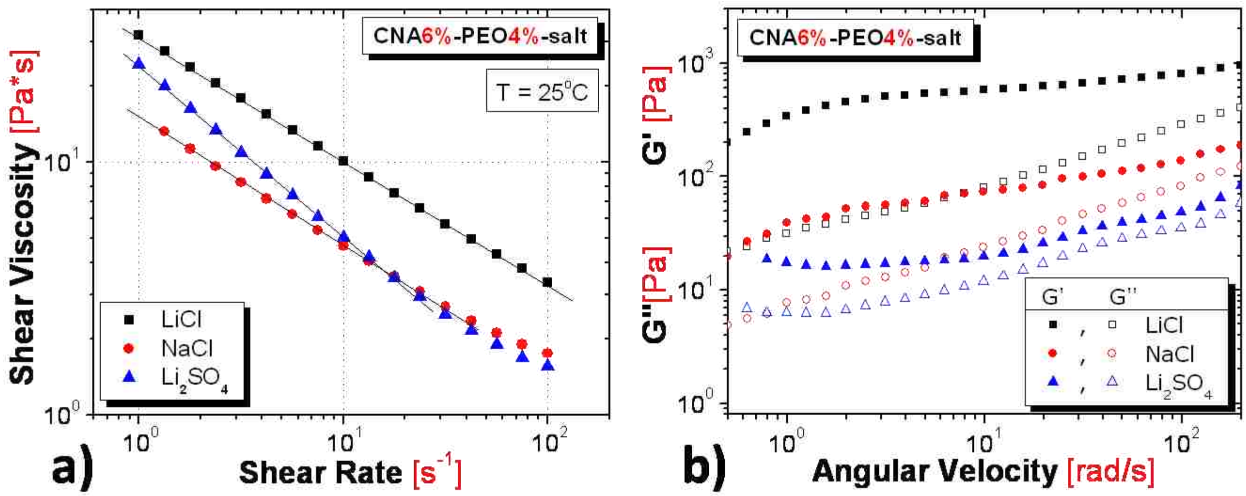

Figure 3.4: a) Shear viscosity of CNA-PEO gels containing different salts at 25 ^{o}C. b) Storage (G') and loss (G") moduli of CNA-PEO gels containing different salts at 25 ^{o}C. All gels contain 90% water. Relative uncertainty for the measurements is ≈ 5%.

3.2.3 Calculated Entropy Changes

The calculated entropy changes of salt containing CNA-PEO nanocomposite dispersions are presented in Figure 3.5a&b. Note that the number of points in Figure 3.5a is limited by the number of points resulted from the elongational rheology measurements (Figure 3.3a). Even though dispersions containing NaCl and LiCl display considerable differences between their elongational and shear viscosity values, we observe an identical behavior of the entropy change for the two gels, with a good superposition of data. The more pronounced entropy change observed for the sample containing Li_2SO_4 indicates that the overall orientational alignment in this system takes place to a greater extent than in the systems containing NaCl and LiCl. The entropy change also varies with the Hencky strain of the hyperbolic die used in the process, where an increase in the Hencky stain results in a higher variation in the calculated entropy of the material (Figure 3.5b).

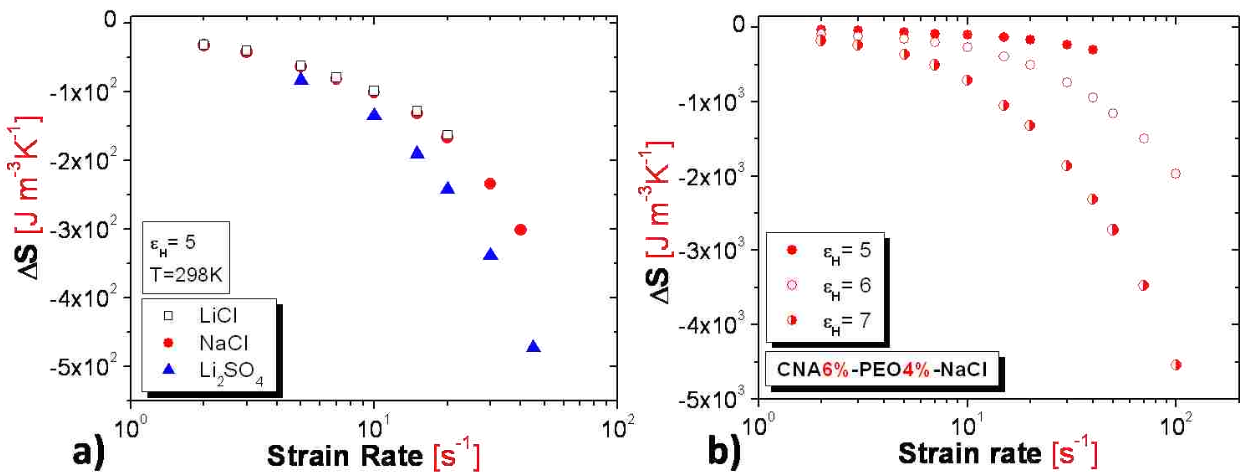

Figure 3.5: Entropy change from rheology for: a) CNA-PEO gels containing different salts at Hencky strain ε_H =5; b) CNA-PEO gel containing NaCl at three different Hencky strains. Relative uncertainty for the measurements is ≈ 5%.

3.2.4 Data Interpretation

An efficient way to stabilize colloidal dispersions is to graft or adsorb polymer chains to the surfaces of particles, producing a steric barrier to flocculation. [82] From previous studies we know that polymers that are long enough to form inter-particle bridges promote formation of a reversible polymer-clay network that dominates the rheological response of the system.[34] At rest, all polymer-clay samples consist of a network between randomly oriented clay platelets and PEO chains with polymer chains acting as dynamic cross-links between the platelets. The rheological behavior of mixtures of particles and adsorbing polymers in a solvent is similar to the one of polymeric physical gels. [82] The shear thinning behavior of our gels typically indicates the occurrence of an overall orientation of the macrostructures and/or nanostructures in the gel. Under shear the clay platelets orient along the flow direction with the surface normal to vorticity direction.[32] The overall orientational alignment in the system is a competition between flow alignment and configurational relaxation, where the flow alignment is induced by orientation of platelets and stretching of polymer chains under shear.

In addition to the polymer-clay interactions, it has been previously shown that in solution a network structure forms between water molecules and polyethylene oxide chains corresponding to two or three water molecules associated with each $–CH_2CH_2O$- unit through hydrogen bonding.[73, 75] When ionic salts are added to the polymer solution the hydrogen bonding is disrupted by the ions.[72] This effect has been observed as a reduction of the viscosity of ion-doped polymer solutions compared to that of undoped polymer solutions.[75] The disruption of the PEO-water network allows the polymer chains to better interact with the montmorillonite platelets. Elongational and shear viscosity results (Figures 3.3a & 3.4a) indicate that the size of the cation introduced in the system (Li^+ vs. Na^+) affects significantly the strength of the transient polymer-clay network. Li cations can spread in the system and coordinate to oxygen containing groups more strongly and uniformly due to their smaller ionic radius and increased diffusion ability when compared to Na cations. Using pair correlation functions Bujdak et al demonstrated that the free cations are primarily coordinated to water molecules and that the PEO chains reside far away from the coordination shell of cations in PEO-montmorillonite-water-salt systems. [1] In such systems the normal water structure is rearranged in the electric field of the cation which leads to a state where the thermal motion of water molecules in the neighborhood of cations is less than in the bulk. [72] Due to the stronger interaction with the water molecules, Li cations are capable of screening the water-PEO hydrogen bonding to a greater extent than Na cations, triggering the improvement of the polymer-clay interactions. Being far away from the coordination shell of the free cations and having most of the “water” hydrogen bonding removed, more PEO oxygens can coordinate to the metals from the surface of montmorillonite platelets. Higher degrees of coordination (cross-linking) are responsible for the increase in the viscosity of the system, as well as for the formation of stronger networks.

When a precursor polymeric solution is cross-linked to form a gel the rheological properties change from those of a viscous liquid to those of an elastic solid.[82] Although our gels contain 90% water, a viscoelastic solvent, all exhibit solid-like behavior for the entire range of studied frequencies (Figure 3.4b). The viscoelastic properties of the gels are strongly dependent on parameters such as the origin of PEO and montmorillonite, the purity of all components (including the water used), the solvent loss during sample preparation, sample mixing time, change in pH with time, storage temperature etc. When all these parameters are kept the same for all systems, we observe that the gel containing the bulky sulfate anions (from the salt) forms a weaker network than the gels containing the chloride anions. The presence of a weak network is revealed by the low storage modulus (G’) values of the Li_2SO_4 sample in Figure 3.4b. Furthermore, the entropic changes indicate that the strength of the network, triggered by the size of the anion (Cl^- vs. SO_4^{2-}), affects the orientational ability of clay particles and polymer chains (Figure 3.5a).

In CNA-PEO dispersions physical gelation occurs as a result of intermolecular associations, which are produced by weak van der Waals forces, electrostatic attractions or hydrogen bonding, and are greatly dependent on the distance between molecules participating in the gelation process.[82] Such associations can be easily reversed if the distance between participating molecules is increased. The free anions introduced in the system (Cl^- & SO_4^{2-}), can as well coordinate to the surface of montmorillonite platelets. Because of their large specific volume, the sulfate anions coordinated to the surface of the clay platelets will act as a barrier in the way of incoming polymer chains approaching the platelets, limiting in this way the polymer-clay interactions. In the same time, any free, uncoordinated SO_4^{2-} ions have the ability to act as spacers for the polymer chains and prevent chain entanglements during the elongational flow process.[75] The two effects explain the presence of weak networks and higher degrees of orientation in polymer-clay systems containing SO_4^{2-}-based salts (Figures 3.4b & 3.5a).

The calculated entropy of the CNA-PEO dispersion containing NaCl is presented in Figure 3.5b at different Hencky strains. The entropy change is observed to increase in magnitude as stain rate increases. At 25 °C (298 K) and 4 x 10^1 s^{-1} (the highest strain rate in the $\varepsilon_H = 5$ curve), the entropy change for the flow induced transformation ranged from -3 x 10^2 J $m^{-3}K^{-1}$ to -9.5 x 10^2 J $m^{-3}K^{-1}$ and -2.3 x 10^3 J $m^{-3}K^{-1}$ for dies with ε_H of 5, 6 and 7, respectively. At 1 x 10^2 s^{-1} the entropy change for ε_H of 6 and 7 reach even lower ΔS values (-1.9 x 10^3 J $m^{-3}K^{-1}$ and -4.5 x 10^3 J $m^{-3}K^{-1}$), indicating a higher degree of orientation developed in the sample. At strain rates below 2 x 10^0 s^{-1} the ΔS values are essentially zero and then they develop a dependence upon elongational strain rate.

3.3 Conclusions

The transformation of polymer-clay gels into highly ordered fluid dispersions under shear has been previously suggested by other authors. [10, 62, 76] SANS measurements under shear even allowed for visualization of platelet orientation in discrete areas of such oriented dispersions.[32, 40] However, to our knowledge, nobody has attempted to quantify the overall extent of orientation occurring in such nanocomposite systems subjected to elongational flow. Calculating the entropy changes developed during elongational flow can help identifying those gels that exhibit the highest degrees of orientation in the process. Since the structure and properties of polymer-clay films are strongly dependent on the structure of precursor dispersion/gels, the method that we describe here can provide a useful route to obtaining highly anisotropic films with improved ionic conductivities and mechanical properties.

CHAPTER 4
A MECHANICAL STUDY ON PEO-CLAY NANOCOMPOSITE GELS AND THIN FILMS

In this chapter the preparation and characterization of polymer-clay nanocomposite gels and films containing various ratios of laponite and montmorillonite is described. The aim is to understand how clays with different chemistry, sizes and surface areas interact with each-other and affect the structure and characteristics of polymer based nanocomposites in the form of both gels and multilayered films. The rheological behavior of the gels is compared to the spreading process and the resulting film structures and properties are analyzed.

4.1 Experimental Procedures

4.1.1 Sample Preparation

In this study laponite-RD (LRD), a synthetic Hectorite type clay, and montmorillonite clay, cloisite Na^+ (CNA), (both Southern Clay Products) were used as received without any further purification. The LRD clay platelets, which are about 30 nm across and ca. 1nm thick charged discs, produce a clear suspension in water. The CNA platelets produce an opaque suspension of predominantly exfoliated platelets that range on average in diameter from 75 to 100 nm across and are ca. 1nm thick. Poly(ethylene oxide) (PEO) with a molecular mass of 1000 kg/mol (Mw/Mn=1.5) was used as received from Polysciences Inc. Exfoliated dispersions were prepared by the addition of PEO and laponite and/or montmorillonite to deionized water, followed by systematic shaking, mixing and centrifuging for at least 4 weeks. The solution pH and ionic strength were controlled by addition of NaOH (pH $\approx$ 9) and NaCl ($5.5*10^{-2}$M) respectively. At rest and room temperature all dispersions are gels. Each multilayered film was prepared by manually spreading the hydrogel on a glass slide with a spatula. Every 1.5 to 2 hours one layer was spread and dried under ambient conditions. Overnight, samples were dried in desiccators. On average, 5 layers were spread every day.

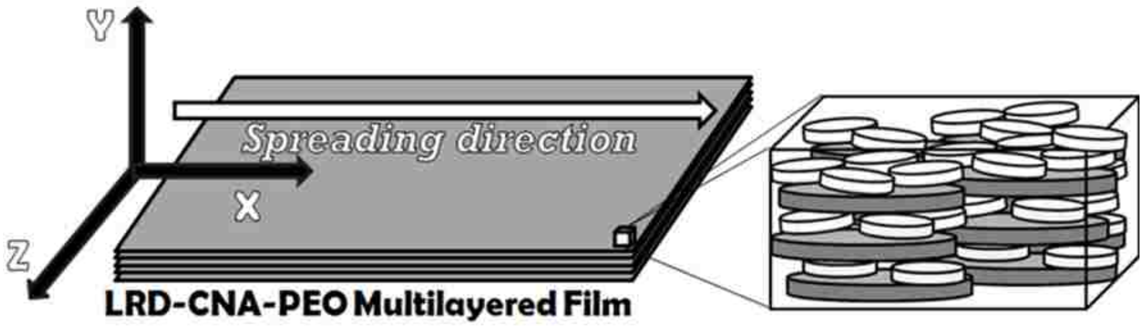

Figure 4.1: General idealized clay platelet orientation in a multilayered polymer-clay film presented along with the definition of planes. The large discs represent the montmorillonite platelets, while the small ones indicate the laponite platelets. Note that the diameter of montmorillonite particles is 3 to 4 times larger than the one of the laponite particles.

The general clay platelet orientation in a multilayered film is presented in Figure 4.1 along with the definition of planes. While one spread and dried film (7μm ± 2 μm) already produces multilayers we used sequential deposition to obtain thicker films simply for better investigation and handling.[5, 67, 77, 104] Films with the same spreading direction (Figure 4.1) were dried layer by layer one on top of another until a total thickness of about 0.2 mm was obtained for the multilayered film. After the last layer was spread and half dried the thin multilayered film was placed in a vacuum oven and dried overnight at 25^{o}C. The sample was then removed from the oven and placed in a desiccator for storage and further drying. Following this procedure a set of five LRD-CNA-PEO gels was prepared with compositions described by Table 4.1. All gels contain 95% water, 2% PEO and 3% clay, where the only difference from a sample to another consists in the ratio of laponite/montmorillonite used to prepare each gel. By evaporating the water in the drying process the final films result with compositions of 40% polymer and 60% clay, being also characterized by different laponite/montmorillonite ratios as illustrated in Table 4.1. The same sample preparation procedure has been used for all five samples.

Table 4.1: Nanocomposite gels and films: composition and crystallinity

	SAMPLE NAME [1]	LRD Conc. (%)	CNA Conc. (%)	PEO Conc. (%)	Crystallinity (%)
LRDX%-CNA(3-X)%-PEO2% - gels (gels contain 95% water)					
1.	LRD**0**-CNA**3**-PEO**2**	0	3	2	N/A
2.	LRD**0.75**-CNA**2.25**-PEO**2**	0.75	2.25	2	N/A
3.	LRD**1.5**-CNA**1.5**-PEO**2**	1.5	1.5	2	N/A
4.	LRD**2.25**-CNA**0.75**-PEO**2**	2.25	0.75	2	N/A
5.	LRD**3**-CNA**0**-PEO**2**	3	0	2	N/A
LRDX%-CNA(60-X)%-PEO40% - films (after water evaporation)					
1.	LRD**0**-CNA**60**-PEO40	0	60	40	30
2.	LRD**15**-CNA**45**-PEO40	15	45	40	21
3.	LRD**30**-CAN**30**-PEO40	30	30	40	10
4.	LRD**45**-CNA**15**-PEO40	45	15	40	1
5.	LRD**60**-CNA**0**-PEO40	60	0	40	0

4.1.2 Rheological Experiments

Oscillatory and steady state shear rheology measurements of nanocomposite gels were performed on a stress controlled TA Instruments AR1000 Rheometer. A cone-and-plate geometry with a diameter of 40 mm, a gap of 27 μm, and a cone angle of $0^{o}59'54''$ was used for all determinations. The instrument was equipped with a solvent trap to prevent water evaporation. All rheological measurements were conducted at a temperature of 25 ^{o}C. Duplicate measurements for both viscosity and moduli (G', G") measurements show good reproducibility with a relative uncertainty of ≈ 7%.

4.1.3 DSC and TGA Experiments

DSC measurements were performed on a TA 2920 MDSC instrument. Samples of 8-10 mg were subjected to analysis using a heating rate of 10 ^{o}C/min in two successive heating cycles. For all DSC curves negative features correspond to endothermic processes. For each

[1] The samples were abbreviated LRDx-CNAy-PEOz, where x, y, and z denote the weight fraction of Laponite, Montmorillonite and Poly(ethylene oxide), respectively, either in solution or in the multilayered film.

measurement, a virgin nanocomposite sample was used in the first heating run followed by cooling and a second heating run. TGA measurements were performed in nitrogen atmosphere with a heating rate of 10 ^{o}C/min using a TA 2950 thermo-balance. Only fresh samples of 7-10 mg were subjected to thermogravimetric analysis. TA Universal analysis software was used for the integration and processing of all curves resulted from DSC and TGA instruments.

4.1.4 DMA Experiments

The glass transition temperature (Tg) and complex, storage and loss moduli (E^*, E', E'') of the thin nanocomposite films were determined via DMA measurements using a Rheometrics Scientific ARES instrument equipped with a torsion rectangular tool, a heating oven and a liquid nitrogen controller.

Figure 4.2: ARES instrument (right), equiped with a tortional tool (left), a heating oven and a liquid nitogen controller, performing DMA measurments on nanocomposite thin films at negative temperatures.

The instrument setup is presented in Figure 4.2. Samples of 0.18 - 0.2 mm thickness and 6 - 7 mm width were subjected to various oscillatory tests. Results were normalized to the same transversal section, 1mm^2, to allow comparison. All DMA measurements were conducted at 25^{o}C except for the glass transition temperature measurements. Duplicate measurements show very good reproducibility with a relative uncertainty of ≈ 5%.

4.2 Results and Discussion

4.2.1 Characterization of Nanocomposite Gels: Rheological Measurements

The rheological behavior of nanocomposite gels was studied to identify the relationship existing between gels composition and their performance under shear, as well as to observe the variation of storage and loss moduli as a function of clay type in the nanocomposite dispersions. Viscosity experiments are presented in Figure 4.3a in an attempt to correlate the shear orientation in the gels with the final orientation in the dried films. As observed in previous work for similar gels, shear thinning behavior is observed over a wide range of shear rates. It can be noticed that at the same clay/PEO ratio laponite clay leads to the formation of gels more viscous than the ones containing only montmorillonite clay. Gradually replacing laponite with equivalent amounts of montmorillonite decreases the viscosity of the gel. This decrease in viscosity is more evident at low shear rates. A remarkable feature in Figure 4.3a is the occurrence of a transition in the system at shear rates higher than $10^{-1}s^{-1}$. The transition shifts to higher shear rates as more laponite is added to the gel, replacing montmorillonite. For LRD0-CNA3-PEO2, LRD0.75-CNA2.25-PEO2 and LRD1.5-CNA1.5-PEO2 samples the transition (indicated by arrows) results in a sudden increase in viscosity, the magnitude of which decreases with the increase of the laponite percent. For gels containing laponite amounts higher than 1.5% (laponite-to-montmorillonite ratio > 1) the transition does not lead to an increase in viscosity but rather to a decrease in the magnitude of the shear thinning behavior. The transition is also temperature dependent, as indicated for LRD0-CNA3-PEO2 in Figure 4.4a, where an increase in temperature shifts the transition peak to higher shear rates. In addition to shifting the transitions shear rates, temperature has also an effect on the magnitude of the transition, where higher temperatures result in larger transitions.

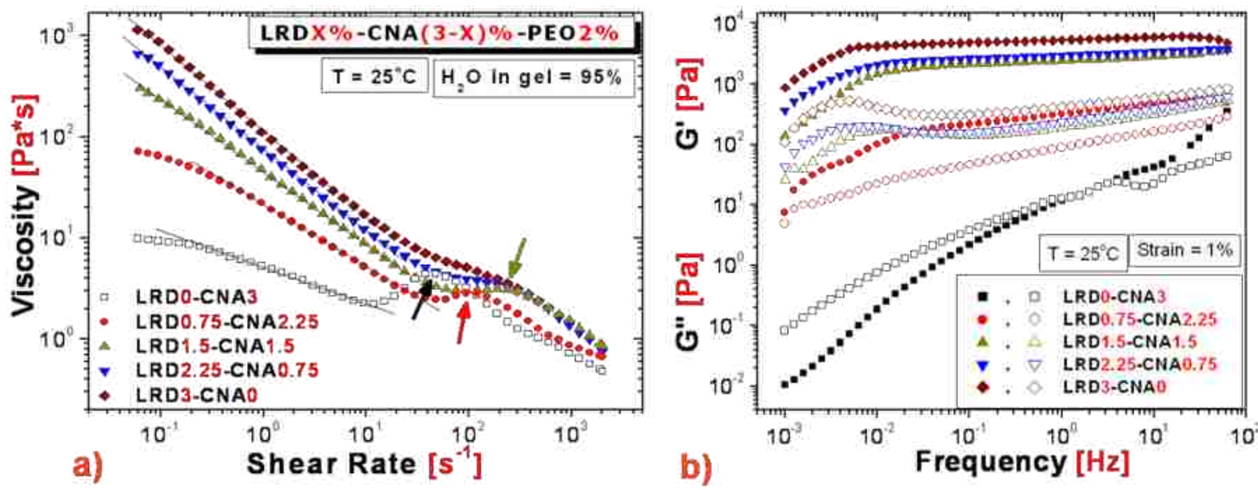

Figure 4.3: **(a)** Viscosity values as a function of shear rate for LRDX-CNA(3-X)-PEO2 nanocomposite gels (95% water) at 25°C; **(b)** Frequency dependence of G' and G" for LRDX-CNA(3-X)-PEO2 gels of various laponite-montmorillonite compositions; G' data is represented with filled symbols and G" data is shown with empty symbols. All gels contain 2% PEO and 95% water. Relative uncertainty for the measurements is ≈ 7%.

At lower shear rates, before reaching the transition domain, there is a near linear relationship between the log(η) and log(dγ/dt), as evidenced by the solid lines in Figure 4.3a. This indicates that over the shear rate dependent region the solutions are power law fluids as described in chapter 3. Power law indexes are in the range of: n = 0.2(+/-0.03) for LRD3-CNA0-PEO2 and LRD2.25-CNA0.75-PEO2, n = 0.3(+/-0.03) for LRD1.5-CNA1.5-PEO2, n = 0.4(+/-0.03) for LRD0.75-CNA2.25-PEO2 and n = 0.5(+/-0.03) for LRD0-CNA3-PEO2. Clearly the shear thinning behavior is enhanced as the concentration of laponite in the clay mixtures increases.

Frequency dependent oscillatory shear experiments of LRD*X*-CNA(3-*X*)-PEO2 samples are presented in Figure 4.3b. The data were taken at strains within a relatively broad viscoelastic range. Although all gels contain 95% water, a viscoelastic solvent, the storage modulus G' always appears larger than the loss modulus G" (except for LRD0-CNA3-PEO2 at low frequencies) indicating elastic behavior. All samples show some frequency dependence of the modulus G’, which increases with increasing frequency. Both moduli G’ and G” are observed to increase when increasing the percent of laponite in the sample. No crossover frequency could be observed for any of the laponite-containing samples. For LRD0-CNA3-PEO2 sample the crossover of G’ with G’’ occurs at a frequency of 2 Hz, indicating a transition from a viscoelastic to a solid-like behavior for this sample with increasing the frequency.

From previous studies we know that polymers that are long enough to form inter-particle bridges promote the formation of a reversible polymer-clay network that dominates the rheological response.[34] All polymer-clay samples consist of a network between randomly oriented clay platelets and PEO chains with polymer chains acting as dynamic cross-links between the platelets. Although several parameters such as surface chemistry, dimensional polydispersity, degree of exfoliation, impurities or affinity of PEO to the clay may affect the rheology of gels, here the major contribution to the viscosity behavior exhibited by the gels is brought by the differences in the surface area of the two types of clay. Due to their small diameter, for a given mass, completely exfoliated laponite platelets provide a very large effective surface available for coordination with the incoming PEO chains. Having diameters three to four times larger, exfoliated montmorillonite platelets provide a much smaller coordination surface, for the same mass. This decreased effective surface leads to the formation of fewer polymer-clay cross-links in the system, which further leads to the appearance of weaker polymer-clay networks, with many free uncoordinated PEO chains. The weaker network is the reason why montmorillonite rich gels exhibit viscosities and shear moduli lower than laponite rich gels (Figure 4.3).

Shear thinning of our gels typically indicates the occurrence of an overall orientation of the macrostructures and/or nanostructures in the gel. Under shear the clay platelets orient along the flow direction with the surface normal to vorticity direction.[32] The overall orientational alignment in the system is a competition between flow alignment and configurational relaxation, where the flow alignment is induced by orientation of platelets and stretching of polymer chains under shear. At high shear rates, where the PEO chains are fully stretched, the adsorption/desorption equilibrium is broken and desorption of chains from the platelets surface occurs at a higher rate than adsorption does. The desorbed polymer chains, now floating free in the system, will recoil in order to reach a more favorable energy state, impairing the flow in the gel. In this way the configurational relaxation gradually increases with the shear rate and negatively affects the overall orientational alignment in the system, leading to the appearance of a transition. Since montmorillonite rich networks are much weaker than laponite rich networks the configurational relaxation for the former systems occurs at lower shear rates, and to a greater extent, making the larger transition-peak shift to the left (Figure 4.3a).

The change in the rheological properties with temperature is due to several factors, among which the most important is that relaxation times decrease strongly as the temperature increases.[81, 105] Due to these smaller relaxation times the onset and the peak shear rates of the unsteady shear flow transitions are shifted to higher values as the temperature increases. In addition to this, the increase of the overall entropy in the gel with temperature, which translates into an amplified disorder in the system, triggers the increase in the magnitude of the transition at higher temperatures (Figure 4.4a).

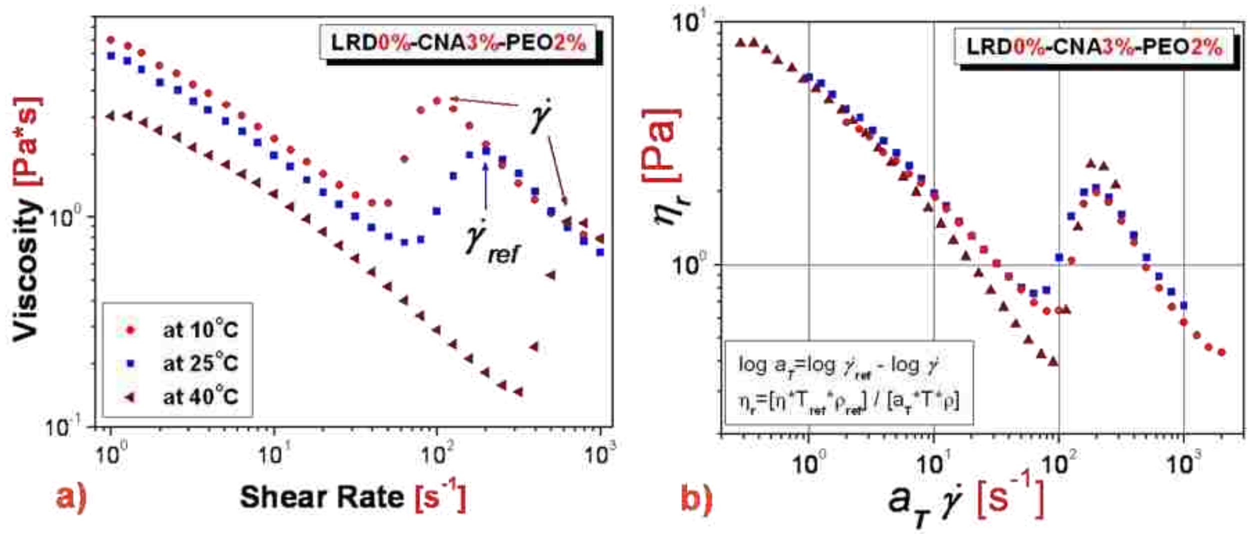

Figure 4.4: **(a)** Viscosity values as a function of shear rate for LRD0-CNA3-PEO2 at different temperatures**; (b)** LRD0-CNA3-PEO2 master curve of reduced shear viscosity η_r versus reduced shift factors. Relative uncertainty for the measurements is ≈ 7%.

In order to verify the agreement and accuracy of our data, and to rule out any instrument artifacts that might have been present in the measurements at high shear rates, the curves from Figure 4.4a were combined into a master curve presented in Figure 4.4b. In this figure the curve at 25°C was used as a reference for shifting the other two shear viscosity curves. The shift factors, a_T, were determined based on a relation described by Young and Lovell: [70]

$$\log a_T = \log \omega_{ref} - \log \omega \qquad (1)$$

where a_T is the shift factor and represents the temperature dependence of the relaxation times, ω_{ref} and ω represent angular frequencies in the reference and non-reference curves. Combining the equivalence of ω with $\dot{\gamma}$, introduced by the extended Cox-Mertz rule,[76, 81, 84] with relation (1) the following equation was obtained:

$$\log a_T = \log \dot{\gamma}_{ref} - \log \dot{\gamma} \qquad (2)$$

where $\dot{\gamma}_{ref}$ and $\dot{\gamma}$ ($\dot{\gamma}=d\gamma/dt$) represent shear rate values for the reference and non-reference curves. Relation (2) was used to calculate the shift factors in this work. In this relation $\dot{\gamma}_{ref}$ and $\dot{\gamma}$

were chosen to be the shear rates of the reference and non-reference curves for which the viscosity of the transition peak was maximum (indicated by arrows in Figure 4.4a). The Williams-Landel-Ferry (WLF) equation, widely used for polymer melts and solutions,[81, 84, 105] does not hold for our systems when constants C_1=17.4 and C_2=51.6 are considered, due to the very high clay amounts present in these polymer solutions. After finding the shift factors the reduced viscosity was calculated using the relation described by Morisson: [81]

$$\eta_r = [\eta(T)^{*}T_{ref}{}^{*}\rho_{ref}]/[a_T{}^{*}T^{*}\rho] \qquad (3)$$

where η_r is the reduced viscosity, T_{ref} (K) is the polymer glass transition temperature, Tg(K), ρ_{ref} is the polymer density at Tg, T(K) is the reference temperature used for shifting the curves, and ρ is the density of the polymer solution at the shifting temperature. The PEO glass transition was considered Tg=207K,[68] ρ_{ref} = 1.1g/cm^3,[76] and ρ solution at 25^{o}C (T=298K) was considered 1g/cm^3, since our gels contain 95% water.

The resultant master curve shows a very effective shifting technique, despite its simplicity. Not all the points of the shifted curves can overlap the reference curve, since the flow transitions have different magnitudes at different temperatures. Shifting a low temperature data onto a higher temperature data extends the reference into higher shear rate domains, and consequently shifting a high temperature data onto a lower temperature data extends the reference curve into lower shear rate domains. Besides verifying the accuracy of the data the master curve also expands the reference curve into a larger experimental window.

4.2.2 DSC and TGA Measurements on Multilayered Films

To better understand the intimate relationship between composition of nanocomposite films and their mechanical properties, we have observed the polymer crystallinity in the systems by means of DSC (Figure 4.5a and Table 4.1). Although extensive studies have been previously done on the crystallinity of various bulk PEO nanocomposites at low clay concentration,[1, 2, 106] here we focus on anisotropic materials at high clay concentrations. Measurements that were done on LRD*X*-CNA(60-*X*)-PEO40 nanocomposites (Figure 4.5a and Table 4.1) indicate that gradually replacing montmorillonite clay with equivalent amounts of laponite results in a gradual decrease of crystallinity up to a point where all the polymer becomes completely amorphous in the sample (LRD60-CNA0-PEO40 sample). If we consider the pure PEO to be 100% crystalline then our results from the LRD0-CNA60-PEO40 sample indicate that 30% of the total polymer is crystalline. The extent of crystallinity decreases in increments proportional to the percent clay replaced in the system (Table 4.1). We expect the clay confined polymer to be amorphous since the coordination of PEO oxygens to various cations from the surface of the platelets disrupts the chains order and limits their possibility to move and rearrange.[49, 107] Our results suggest that the high surface/gram ratio, triggered by the small size of laponite platelets, provides the PEO chains with a confinement area large enough to totally suppress their crystallinity (LRD60-CNA0-PEO40 sample). At the opposite side, the large montmorillonite platelets from the LRD0-CNA60-PEO40 sample are only enough to suppress 70% of the pure polymer crystallinity.

When polymer chains are adsorbed to the clay layers, water molecules initially present on the silicate surfaces and galleries are displaced to accommodate the polymer chains. Although the nanocomposite films have been dried in vacuum, some water molecules may still be trapped in the films, as indicated by TGA measurements (Figure 4.5b). Displaced water molecules from the clay surfaces, or water molecules from the precursor solutions, are likely trapped within PEO crystallites, shifting the melting transition to lower temperatures (Figure 4.5a).[44]

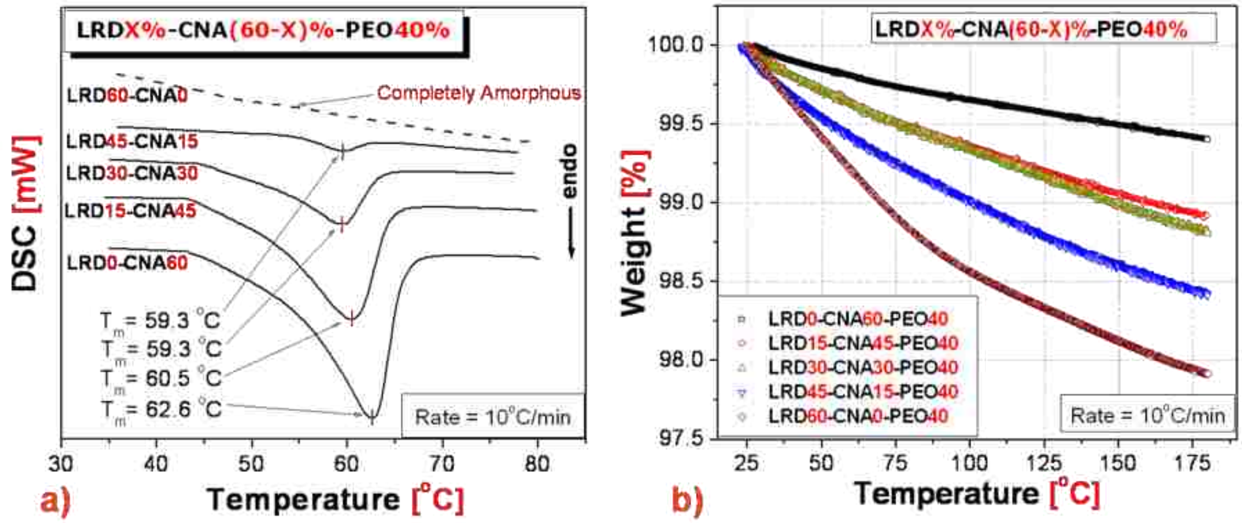

Figure 4.5: DSC **(a)** and TGA **(b)** traces for LRDX-CNA(60-X)-PEO40 nanocomposite thin films at a heating rate of 10°C/min. All films contain 40% PEO.

The trend observed in the TGA plot also indicates that laponite rich films retain higher amounts of water than montmorillonite rich films. The high affinity of PEO chains towards water makes complete removal of these small molecules from the dried films very difficult, even when films are stored in desiccators for several weeks. One can see that a higher PEO crystallinity results in a lower polymer affinity for water molecules (Figure 4.5b).

4.2.3 DMA Measurements on Multilayered Films

Very largely used in polymer characterization the principle of DMA consists in applying an oscillating force to a solid sample and analyzing the material's response to that force. When subjected to such a force, also called stress (σ), a composite material exhibits a deformation or strain, γ. The relationship existent between stress and strain is a measure of material's stiffness or modulus. In DMA, three different moduli can be calculated from the response of the material to the sinusoidal wave: complex modulus, E^*, elastic (storage) modulus, E', and imaginary (loss) modulus, E''.[83] The relation between the three moduli is given by the equation $E^*=E' + iE''$, where $i=\sqrt{-1}$. Although complex, elastic and loss moduli are dependent on many parameters, in this work we only study their behavior as a function of testing frequency, temperature and time.

The storage (E') and loss (E") moduli of the five nanocomposite films are presented in Figure 4.6a as a function of testing frequency. It can be observed that the progressive increase of the montmorillonite percent in the sample leads to a gradual increase of E' and E" values in the multilayered films. Furthermore, the relationship between storage moduli of nanocomposite films (E') and storage moduli of nanocomposite gels (G') is shown in Figure 4.6b. The plots, obtained by correlating the E' values from Figure 4.6a with the G' values from Figure 4.3a, for frequencies ranging from 10^{-2} Hz to 10^{1} Hz, are linear. The negative slope of the linear fittings indicates that both E' and G' increase with raising the frequency, while the gradual enlargement in the slopes' magnitude shows that E' elevates much faster than G' with increasing the amount of montmorillonite in the nanocomposites.

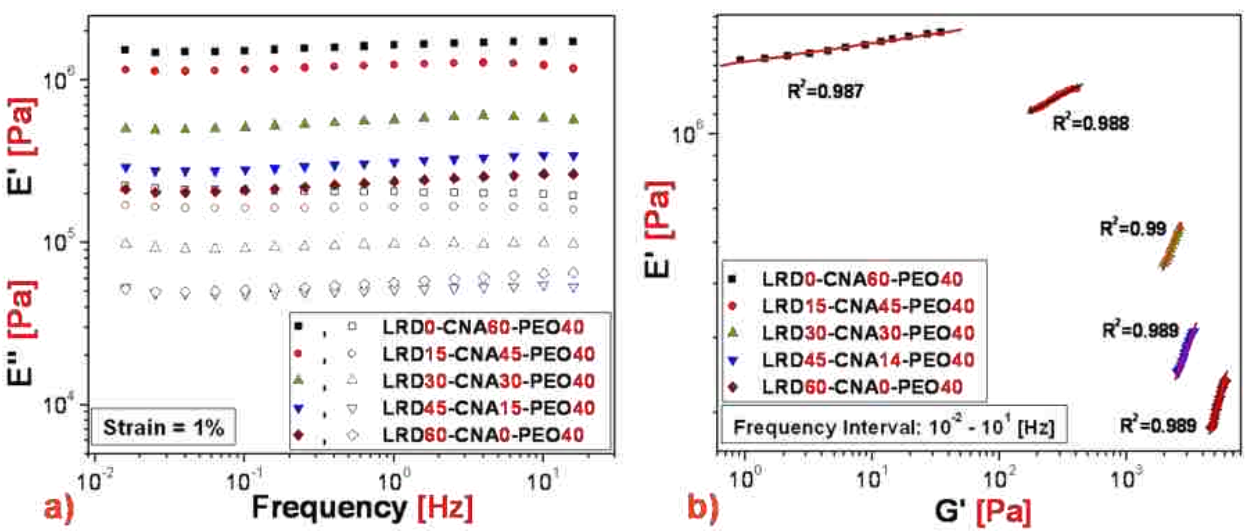

Figure 4.6: **(a)** Frequency dependence of storage modulus (E') and loss modulus (E") for LRDX-CNA(60-X)-PEO40 nanocomposite thin films. E' data is represented with filled symbols and E" data is shown with empty symbols. **(b)** Relationship between storage modulus of nanocomposite films (E') and storage modulus of nanocomposite gels (G'). Relative uncertainty for the measurements is ≈ 5%.

The complex modulus (E^*) values of the multilayered films are presented in Figure 4.7 as a function of frequency, at two different oscillation amplitudes (strain %). Comparing Figure 4.7a with Figure 4.7b, one can clearly see that an increase in the oscillating amplitude, from 0.1% to 1%, results in a considerable decrease of E^* for all the samples. Similar to the behavior observed for E' at 1% strain (Figure 4.6a), the E^* of the nanocomposites at this oscillating amplitude (Figure 4.7b) increases with increasing the montmorillonite fraction in the sample. However, at oscillating amplitudes of 0.1%, despite having a lower montmorillonite percent, the LRD15-CNA45-PEO40 sample shows a complex modulus higher than the one of LRD0-CNA60-PEO40 sample, for the entire frequency range studied here. Furthermore, at 10 Hz, the E^* of the completely amorphous LRD60-CNA0-PEO40 sample equals the one of the LRD45-CNA15-PEO40 sample, and it is expected to exceed this value at even higher frequencies (Figure 4.7a). Due to the instrument limitations, measurements at frequencies higher than 15 Hz could not be conducted.

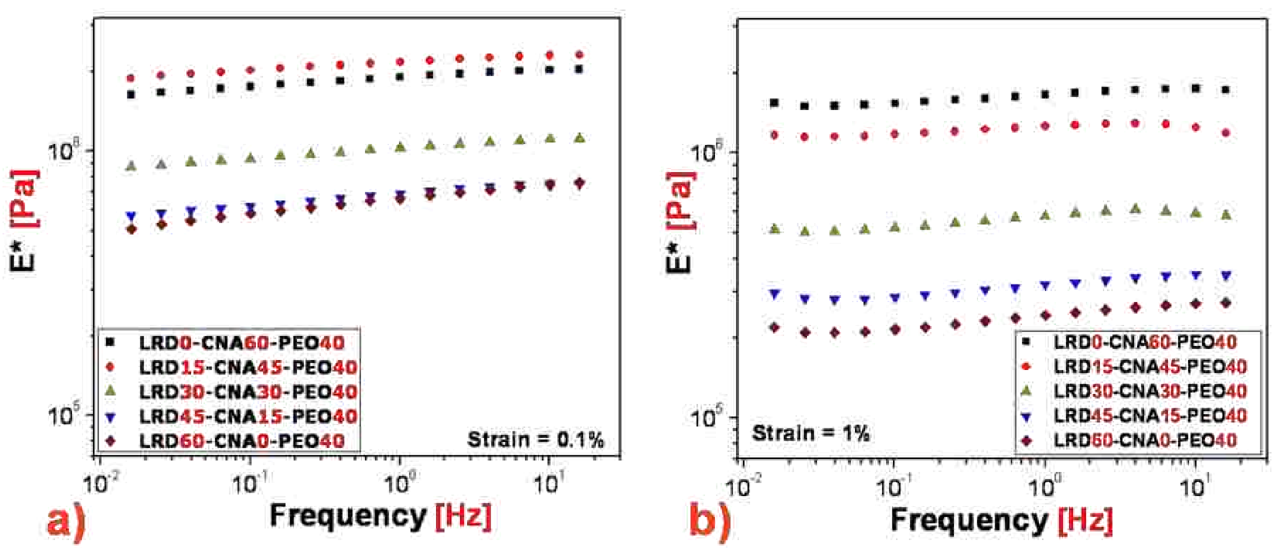

Figure 4.7: Dependence of complex modulus (E^*) for LRDX-CNA(60-X)-PEO40 nanocomposite thin films on frequency at 0.1% strain **(a)**, and 1% strain **(b)**. Relative uncertainty for the measurements is ≈ 5%.

The behavior of E’ and E” observed for the multilayered films in Figure 4.6a is totally opposite to the one observed for the storage (G’) and loss (G”) moduli of the precursor nanocomposite gels (Figure 4.3a). While the factor responsible for the elevation of G’ and G” in gels was the increase in the strength of the polymer-clay network, the reason for the elevation of E’ and E” in the films consists in the increase in crystalline fraction of the PEO in the nanocomposite. Since the strength of the network in solution is given by the fraction of PEO chains cross-linked to the clay platelets, which cannot rearrange and crystallize, it follows that the strength of the network is inversely proportional to the fraction of crystalline PEO in the film. The increase in the crystallinity of the samples is also responsible for the increase of E^* (Figure 4.7), given that at 25 ^oC E^* is essentially E’. In addition to crystallinity variations an important contribution to the overall behavior of E’ and E^* of the films could also be brought by the general orientation of nano-platelets in the composite multilayered films. One would expect highly oriented films to exhibit an increased toughness, and in consequence, an enhanced E’. The large aspect ratio of the montmorillonite clay may play a decisive role in maintaining the polymer covered platelets aligned in the same direction throughout several length scales. The much smaller laponite platelets have difficulties in maintaining the same direction in the film, and high amounts of this clay in the nanocomposite may lead to a decrease in the storage modulus, E’.

For the frequency dependence of E^* at 1% strain (Figure 4.7b) excellent reproducibility was achieved when measurements were each time repeated on a fresh sample. However, while attempting to do a second determination on samples already tested at this oscillating amplitude we observed that the thin films break and the results cannot be reproduced. To elucidate the behavior of nanocomposite films under prolonged stress a set of time dependent measurements of E^* was conducted, the results of which are presented in Figure 4.8. At the oscillating amplitude of 1% the nanocomposites experience severe deformations, which set off the appearance of small micro-cracks on the surface of the films. In time and under oscillating stress these micro-cracks grow bigger, link with each-other and form macro-cracks, which lead to an important loss of materials strength, triggering in this way the decrease in E^*.

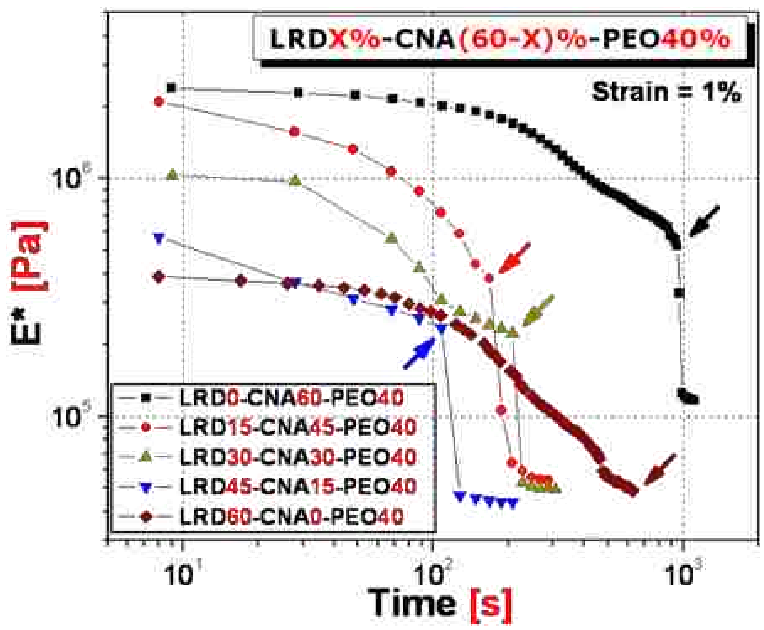

Figure 4.8: Dependence of complex modulus (E*) for LRDX-CNA(60-X)-PEO40 nanocomposite thin films on time at 1% strain and a frequency of 10 rad/s. Arrows indicate the failure points for the five nanocomposites. Relative uncertainty for the measurements is ≈ 10%.

Further deformations irreversibly lead to the fracture of the nanocomposite films (points indicated by arrows in Figure 4.8). One can notice that the nanocomposites containing only one type of clay, as is the case for LRD0-CNA60-PEO40 and LRD60-CNA0-PEO40, have a better resistance to fatigue than the rest of tested materials. We attribute this improved fatigue resistance of samples containing only one type of clay to an increased homogeneity of the systems, generated by a consistent size and surface area of the nano-platelets.

The temperature dependence of complex modulus of nanocomposite thin films is presented in Figure 4.9 for a frequency of 10 rad/s and a strain of 1%. A horizontal plateau followed by a gradual decrease of E^* with the temperature can be observed for all the samples.

The glass transition temperature, at which the decrease of E^* begins, was found to be -66°C, value that has been previously reported in literature for PEO.[68] Due to the small PEO percent in the nanocomposites (40%), and to the very small thickness of the films (0.18 to 0.2 mm), the loss modulus (E”) curves, and in consequence the tanδ curves, for all the studied samples resulted very noisy for the entire temperature range, even when measurements were repeated.

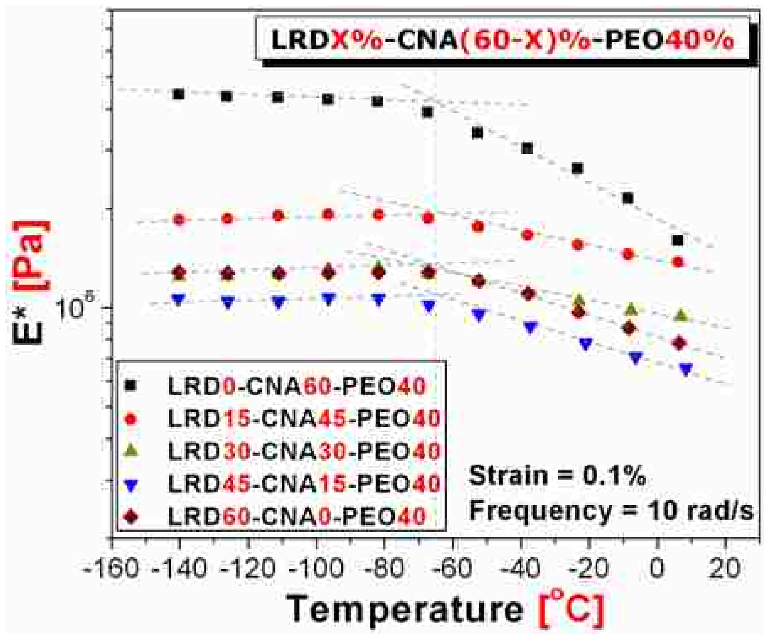

Figure 4.9: Dependence of complex modulus (E*) of LRDX-CNA(60-X)-PEO40 nanocomposite thin films on temperature. Relative uncertainty for the measurements is ≈ 5%.

For the temperature range presented in Figure 4.9 E^* is virtually the same with E’ due to the high rigidity of the samples at these temperatures. The small deformations used here (0.1% strain) allowed the measurements to be repeated on the same sample up to four times, without damaging the nanocomposite films. Surprisingly, E^* of the completely amorphous LRD60-CNA0-PEO40 sample shows values higher than the ones of the LRD45-CNA15-PEO40 sample, which contains a small fraction of crystalline polymer (Table 4.1). In the past we have shown that the high polydispersity of natural montmorillonite (CNA) clay leads to heterogeneities and more defects in orientation compared to the low disperse synthetic laponite (LRD) clay.[14] The more compact structure of the montmorillonite-free LRD60-CNA0-PEO40 film is able to compensate for the lack of polymer crystallinity and to exhibit a complex modulus higher than the one of LRD45-CNA15-PEO40 sample at this range of temperatures.

4.3 Conclusions

In this chapter we have shown that the mechanical behavior of polymer-clay nanocomposite dispersions and multilayered films can be tuned by controlling the ratio of laponite-to-montmorillonite in the materials. While the shear thinning behavior is enhanced and the viscosity is increased as the concentration of laponite increases in gels, the progressive increase of the montmorillonite percent in the samples leads to a gradual increase in the storage and loss moduli, E' and E'', of the multilayered films. We observed that the factor responsible for the elevation of G' and G" in gels is the increase in the strength of the polymer-clay network. On the other hand, the elevation of E' and E" in multilayered films is due to the increase in crystalline fraction of the PEO in the nanocomposites. In the future we will study the influence of clay ratio (laponite-to-montmorillonite) on the ionic conductivity of the resulting nanocomposite multilayered films.

CHAPTER 5
SUPRAMOLECULAR STRUCTURES IN PEO-MONTMORILLONITE MULTILAYERED FILMS*

In this chapter we investigate the multilayered structures of poly(ethylene oxide) montmorillonite nanocomposite films made from solution. The shear orientation of a polymer-clay network in solution combined with simultaneous solvent evaporation leads to supramolecular multilayer formation in the film. The resulting films have highly ordered structures with sheet-like multilayers on the micrometer length scale. Results from SANS and XRD that provide information on the structure of these films are provided. Complementary AFM and SEM images that provide direct visualization of the nano and micrometer structures are also included.

5.1 Experimental Procedures

5.1.1 Sample Preparation

We have prepared viscoelastic solutions of the natural smectite type clay, montmorillonite, Cloisite NA+ (CNA), (Southern Clay Products)[108], and poly(ethylene oxide) (PEO), purchased from Polysciences Inc., (M_w = 1 x 10^6 g/mol, M_w/M_n ca: 1.5, $R_g \approx 100$ nm in H_2O).[109] The CNA clay produces an opaque suspension of predominantly "exfoliated" platelets (no peaks at high q in SANS)[110] that range on average in size from ca. 70 to 150 nm across and are ca. 1 nm thick (Atomic Force Microscopy). Several <10 nm and ca. >1-2 micron large platelets can also be observed thus the reported polydispersity of 30% for the platelet diameter[108] may not be accurate for every type of natural clay, but dependent on the batch and the source.

* Reproduced in part with permission from PCCP Owner Societies, E. A. Stefanescu, A. Dundigalla, V. Ferreiro, E. Loizou, L. Porcar, I. Negulescu, J. Garno, G. Schmidt, Supramolecular structures in nanocomposite multilayered films, **2006**, 8, 1739–1746, Copyright © 2006 Royal Society of Chemistry

Polydispersity also depends on the treatment and purification of CNA clay, especially if the purification process removes the smaller platelets or the largest ones. Discrepancies between measured sizes for natural clays from the same supplier are known.[110, 111]

Multilayered films were prepared from solution via gel/solution exfoliation while exfoliated and stable solutions were obtained for a particular polymer clay ratio, pH and ionic strength.[32-34, 67] Here multilayered films are discussed that have been prepared from an aqueous solution containing mass fractions of 3 % clay and 2 % PEO at ambient temperature. The solution pH and ionic strength were controlled by the addition of NaOH (pH = 9-10) and NaCl (1 mM), respectively. Using a pH >>10 or pH <<9 in solution leads to chemical breakdown of the clay over time.[112] Gels were spread onto glass slides layer-by-layer and dried at 25 °C in desiccators and under vacuum. While one spread and dried film (ca 3-7 microns thick) already produces multilayers as examined by SEM, the film thickness of one spread film is too small to be cut and thoroughly investigated by scattering and microscopic techniques used by us. Therefore we use a layer by layer spreading and drying technique to obtain thicker films for better investigation. SEM was repeatedly used to examine the interface between the spread layers but no interface could be detected indicating intermixing of spread layers. Multilayered films containing ca. 60 % of CNA clay and 40 % of PEO polymer (by mass fraction) were obtained (CNA60%-PEO40%). The shear-orientation combined with the drying procedure as well as control of the film thickness is absolutely necessary to obtain the highly ordered multilayers; simply drying the film is not sufficient.

5.1.2 SANS Experiments

SANS measurements were preformed on the 30 m SANS NG7 instrument at the Center for Neutron Research (NCNR), National Institute of Standards and Technology (NIST).[113] In a standard y-beam configuration, the incident beam is perpendicular to the spread direction of the film and the SANS intensity is obtained in the x-z plane. In the z-beam configuration, the incident beam is parallel to the spread direction of a 0.5 mm thick PEO-clay film (see Figures 5.1 and 5.2). The neutron beam in z-beam configuration provided SANS intensities in the x-y plane. The primary contrast in the SANS experiment is between the silicate and PEO. This allows SANS experiments to detect the overall orientation of the clay platelets in a polymer matrix (Figure 5.2).

5.1.3 Microscopy Experiments

Sample preparation for the AFM and SEM measurements included cryo-ultramicrotom slicing (Leica ultracut with FC4 from Reichert-Jung) and freeze fracture. All samples were cut at -120 °C, below the PEO glass transition temperature (T_g = -55 °C). The AFM images were recorded with a Nanoscope IIIa Dimension 3100 (Veeco Instruments).[114] AFM "phase imaging" can be used to distinguish clay particles from the PEO matrix due to their difference in mechanical properties. SEM experiments were performed using a Cambridge 260 Stereoscan Electron Microscope. Many fractures in all three planes were investigated and only representative images are presented. Optical microscopy was also performed using an Olympus BX51TF microscope with crossed polarizers.

5.1.4 DSC and TGA Experiments

DSC measurements were performed on a TA 2920 MDSC instrument. Samples of 2.5-10 mg were subjected to analysis using a heating rate of 10 ^{o}C/min in two successive heating cycles. For all DSC curves negative features correspond to endothermic processes. For each measurement, a virgin nanocomposite sample was used in the first heating run followed by cooling and a second heating run. The collected data have been normalized to a PEO content of

1.0 mg. TGA measurements were performed in nitrogen atmosphere with a heating rate of 10 ^{o}C/min using a TA 2950 thermo-balance. Only virgin samples of 5-10 mg were subjected to thermogravimetric analysis. TA Universal analysis software was used for the integration and processing of all curves resulted from DSC and TGA instruments.

5.1.5 XRD Experiments

The X-ray diffraction measurements were done using a Simens-Bruker D5000 X-ray Diffractometer with a Cu Kα radiation of 1.54Å. Diffraction patterns were collected from $2\theta = 2^{o}$ to $2\theta = 50^{o}$ with steps of 0.02^{o} and a scan time of 2s per step. All collected data were normalized to the same baseline for a better comparison of final results. Samples were dried and kept in desiccators before each measurement.

5.2 Results and Discussion

5.2.1 Determination of Clay Platelet Orientation in the Film

The solution structure and fabrication conditions strongly influence the morphology of the multilayered dried films.[5] In solution the adsorbed PEO polymer is strongly attached to the clay and the excess polymer that is not adsorbed is stabilizing a sponge-like polymer-clay network.[41, 45, 46] The predominant orientation of CNA platelets in solution is with the flow and with the surface normal along the velocity direction.[104] The orientation of CNA platelets in the dried film is expected to be in the film plane. A simple physical picture of clay platelet orientation in the multilayered films as well as the definition of planes is shown in Figure 5.1.

The orientation of the clay platelets can be deduced from the SANS results (Figure 5.2). The isotropic SANS pattern in the x-z plane and the anisotropy observed in the x-y plane confirms the orientation of the platelets to be with the surface normal perpendicular to the film plane (x-z plane). From the 2D SANS patterns in x-z and x-y direction, the intensity as a function of q can be calculated in all three directions in space.

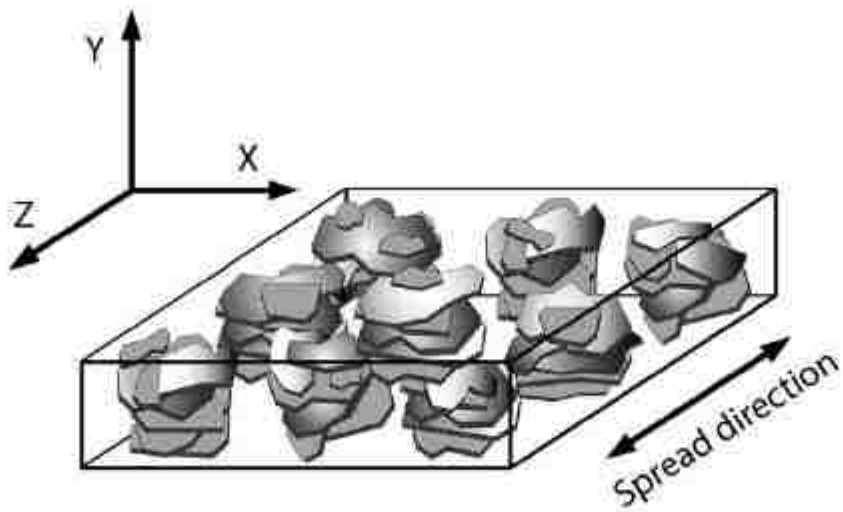

Figure 5.1: A physical picture of general clay platelet orientation in a multilayered polymer nanocomposite film is shown as well as the definition of planes.

Anisotropy is observed over at least 2 orders of magnitude in q which indicates orientation of clay platelets over the whole q range is detected. A change in slope between 0.001-0.01 and 0.01-0.1 reciprocal Angstroms or the hint of a shoulder that is observed around q= 0.01 reciprocal Angstroms ($2\pi/q \approx 60$ nm) may be correlated with the ca. 56nm thickness of layers detected by microscopy. Intensities in x and z directions as well as the x directions from both configurations overlap as expected. Since the SANS is averaged over the sample volume, the 2D SANS patterns shown in Figure 5.2 look similar to SANS patterns from other oriented nanocomposites studied in the past.[5, 39] However, results from microscopy show very unusual and unexpected structures.

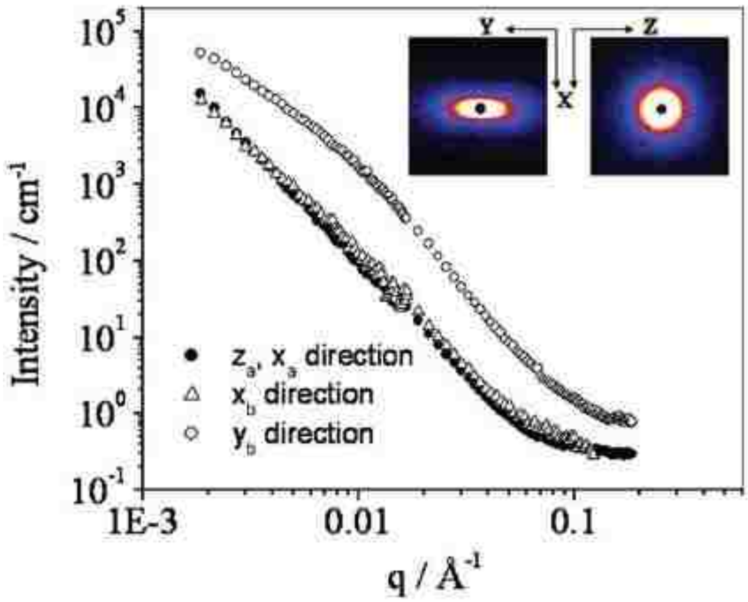

Figure 5.2: SANS intensity as averaged in 10 degree sectors for all three directions in space. 2D SANS spectra from a ca. 1mm thick multilayered film obtained in the x-z plane and in the x-y plane.

5.2.2 Visualization of Supramolecular Order: Microscopy Experiments

The polymer-clay morphoplogy and texture orientation as displayed from representative Atomic Force Microscopy (AFM) is illustrated in Figures 5.3 and 5.4. Compared to what is usually found in literature on polymer nanocomposite orientation, our results show an unusual and unexpected 3D ordered and layered structure of blob-like chains and layers. The orientation of individual CNA clay platelets with an average diameter of ca. 70-150 nm and a thickness of 1 nm does not easily explain the presence of ordered layers of elongated “blobs” (Figures 5.3 and 5.4). The average blob thickness is ca. 56 nm and the average blob length is ca. 100 nm (Figures 5.3) while a chain of blobs can be very long. The 56 (±16) nm blob chain thicknesses (y-direction) correspond to polymer wrapped clay stack layers as seen from the side (blob may contain several platelets). The high polydispersity of natural montmorillonite CNA clay (average size 70-150 nm) leads to heterogeneities and more defects in orientation compared to the low disperse synthetic laponite LRD clay (30 ± 5 nm diameter platelets).[5] Multilayered films shown in Figures 5.4a and 5.4b, strongly reflect the differences in polydispersity of CNA versus LRD clay. The average x-direction correlation length observed from several AFM images (such as Figure 5.3 and 5.4) is ca. 100 (±20) nm per blob for CNA60%-PEO40%. This blob length corresponds to an average clay diameter for CNA platelets which is around 100nm (Figure 5.4). For LRD60%-PEO40% shown in Figure 5.4b the correlation length of the blobs observed is much smaller, more uniform and on the order of 30-60nm.

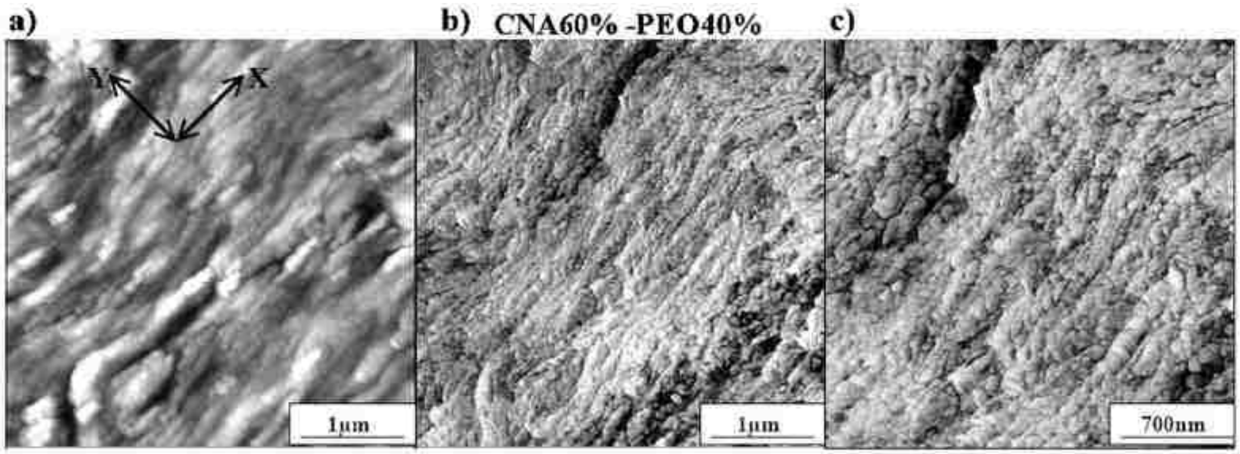

Figure 5.3: AFM **a)** height image and **b-c)** phase images from the x-y plane sections of CNA60%-PEO40% multilayered films.

If we assume that ca. 100nm is the correct average CNA clay platelet diameter then we may wonder what happened with the few large platelets that are >1 microns in size? AFM from pure and diluted CNA solutions suggests the presence of few large platelets >1 microns. It is possible that many of the large platelets are broken down during the sample preparation process and those few remaining form large defects that are not shown with AFM but may be visualized by optical microscopy. An alternate interpretation suggests that it is possible that the larger polymer covered platelets are arranged between the blob-like chains and layers since the length of some of these layers is on the order of several 1000nm. This interpretation is supported by the nm size layered structures we have observed for films at higher salt concentration studied by us in the past.[67] Here large amounts of excess PEO may cover up any blob like chains and lead to a different type of layered structure.[67] Due to higher polymer concentrations neither height nor phase imaging can distinguish between individual platelets at CNA40%-PEO60% concentrations studied in the past.[67] Although the 2D SANS data for both, the CNA40%-PEO60% films studied in the past[67] and the CNA60%-PEO40% films presented here look qualitatively very similar, the local morphology such as the interconnected blobs versus layers, is very different.

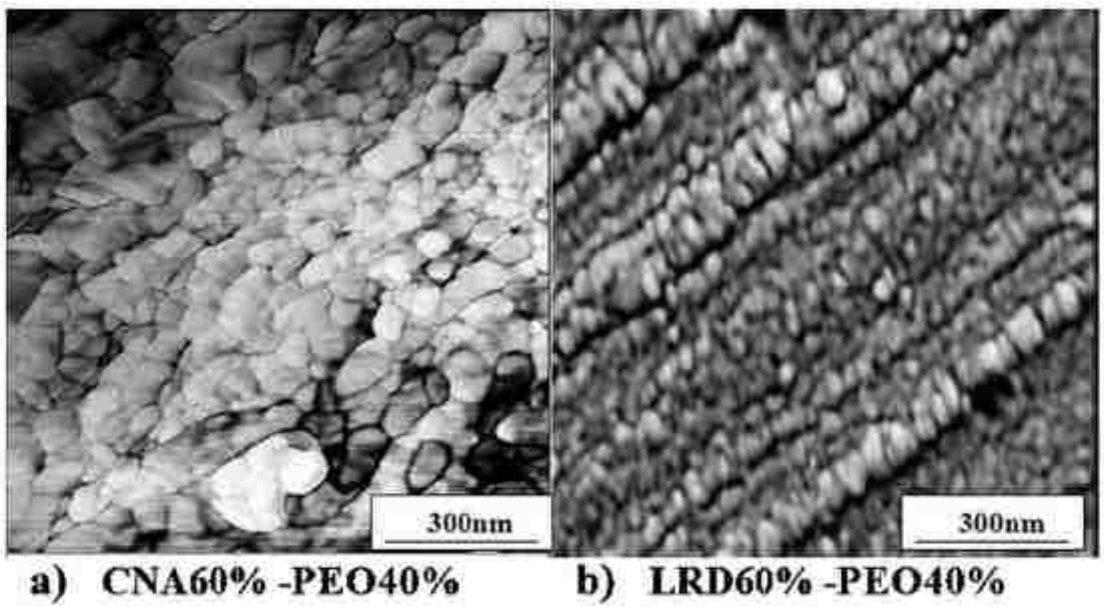

Figure 5.4: **a)** AFM images from the x-y plane sections of multilayered films for CNA60%-PEO40% and **b)** LRD60%-PEO40%, both phase images. For a) and b) the clay concentration is high enough as to distinguish individual or bundles of clay particles.

To better understand the film structure formation we need to know the polymer clay interactions in solution. In solution the clay particles can only adsorb a finite amount of polymer until all the clay surfaces are covered.[41] The polymer and the clay build a sponge-like network structure that is interpenetrated by a sub-network of interconnecting pores containing excess polymer and water.[41] Since the polymer adsorbed clay is completely exfoliated in solution (no peaks in diffraction patterns from solution) this solution-structure must collapse, reorder and re-intercalate into blob-like chains during the film formation process. The more or less uniform blob size observed in the film is highly reproducible and must be related in some way to the sponge like structure in solution.

For synthetic laponite clay the absorbed polymer layer has been measured before to be ca. 1.5 nm on each face.[41] In the film the excess polymer is wrapped around the stacked laponite clay platelets forming 30-60nm blobs (Figure 5.4b).[5] Montmorillonite (CNA) clay does the same except that the blobs observed are more polydisperse and elongated due to larger aspect ratio (ca 100nm long and 56nm PEO covered stacks of platelets) (Figure 5.4a). Our preliminary results from solutions also showed that the platelets within a polymer-clay network are interconnected over the edge more than over the face.[41]

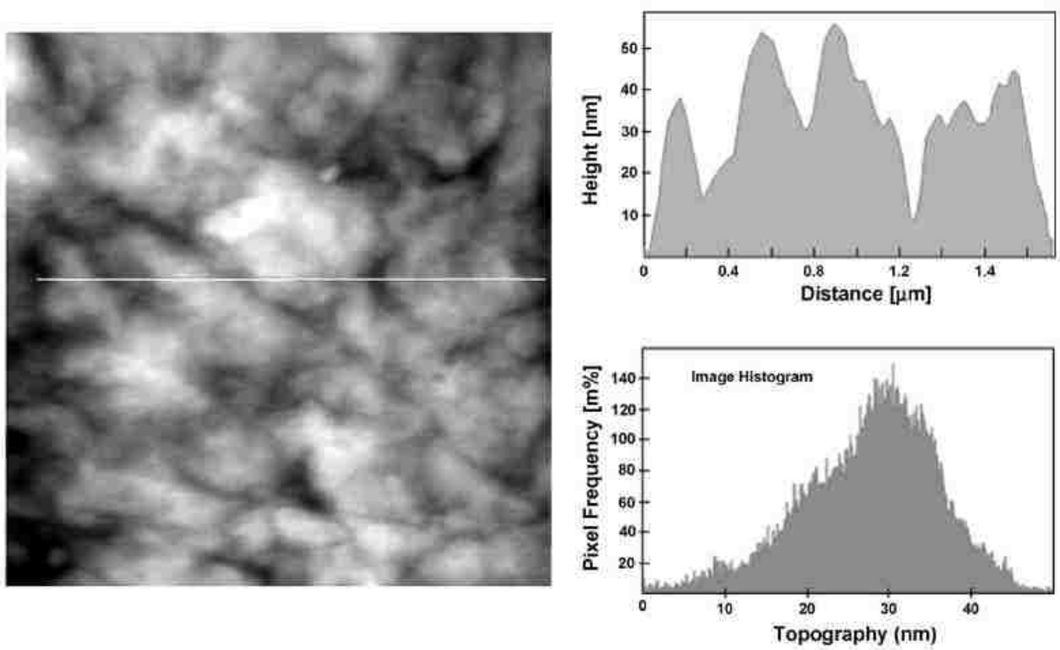

Figure 5.5: A representative AFM image is shown from the top plane of a multilayered film for CNA60%-PEO40%. Cursor profile and histogram are also shown. No layered structure is visible.

We hypothesize that when the network is stretched, and the solvent evaporates simultaneously, the network collapses, the clay platelets re-intercalate and the edge to edge connection in solution may favor the formation of blob-like chains and sheets in the film. The sliding of already existing blob chains and sheets of a sheared but not completely dried film may also influence the observed layered structures which are very similar to shear oriented liquid crystalline lamellar phases. As for the surface structure of the layers, AFM in the x-z plane shows many smooth and flat polymer covered areas as well as very few ca 70-150nm large polymer covered platelets (Figure 5.5).

Scanning Electron Microscopy (SEM) is used to determine the film morphology on the micron length scale (Figure 5.6). As mentioned previously, the aqueous CNA-PEO solutions can be described as interconnected networks.[104] When the sample is shear-oriented and the solvent evaporates simultaneously, the network collapses which leads to layered film structures that can be observed on several length scales. In the side section of the films (Figure 5.6), SEM was used to examine whether an interface exists between individual spread layers. Similar to other polymer-clay multilayered films that we have studied before[67] no boundaries between spreading layers (each 3-8 μm) could be detected, indicating substantial intermixing of spread layers. Nevertheless a highly ordered and layered structure of the films is observed in the x-y plane, while smooth and flat surfaces are observed in the x-z plane (not shown here). The layered texture observed in the x-y direction is not uniform and is calculated to have an average dimension of $d_{SEM} \approx$ 60-70 nm per layer (Figure 5.6c). Even though the exact shear rate during the spreading process cannot be controlled, SEM shows high reproducibility in data. According to AFM measurements each of the ca. 60-70 nm thick layers observed by SEM corresponds to the blob like chains and layers that are on average 56 nm thick (Figures 5.3 and 5.4). Discrepancies between data from AFM and SEM may be due to differences in resolution. Reference PEO films made from pure PEO solutions with the same salt concentration as the

CNA60%-PEO40% films showed no layered structures suggesting that the addition of salt to pure PEO solutions does not lead to any layer formation.

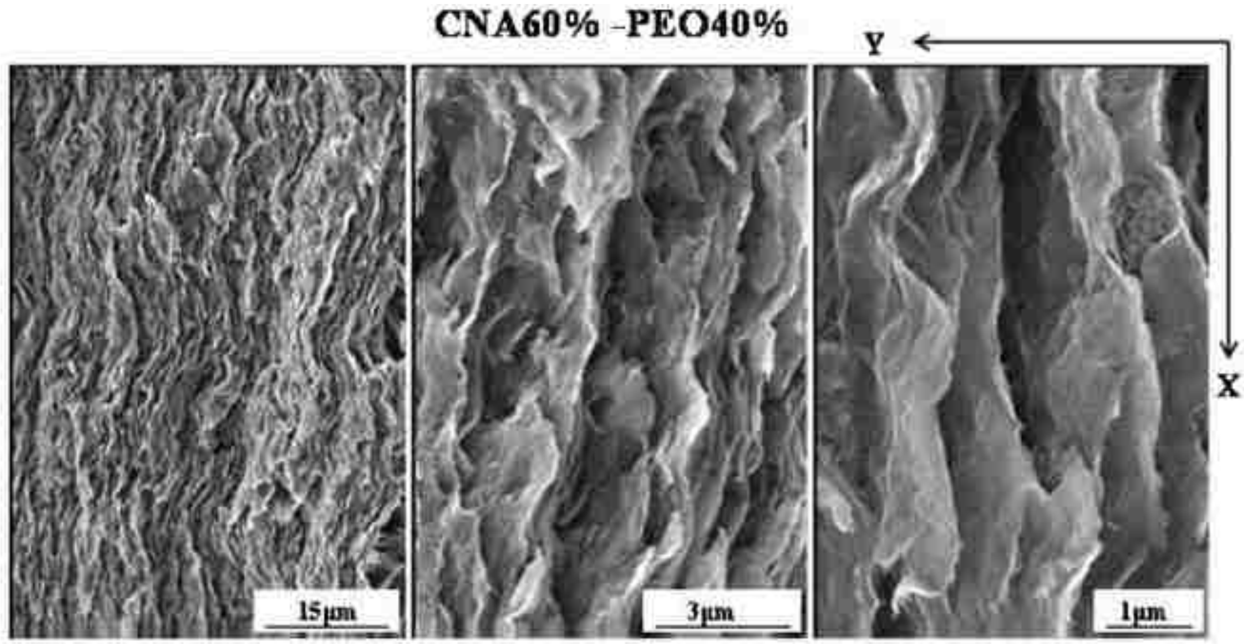

Figure 5.6. SEM images of freeze fractured x-y plane surfaces of CNA60%-PEO40% multilayered films at different magnifications. A distinct layered structure is visible.

On a micrometer to centimeter length scale, the CNA60%-PEO40% films presented here look different from the CNA40%-PEO60% films studied in the past[67]. The lower polymer concentration used here leads to a more open structure with less interconnected layers in the x-y plane (Figure 5.6) and completely smooth top surfaces. The CNA60%-PEO40% films presented here also look very different from the LRD60%-PEO40% films studied in the past.[5] At the same polymer, clay and salt concentrations, the larger CNA platelets (ca 100nm) lead to less oriented micrometer size layers compared to the smaller LRD platelets (ca. 30nm). Inspection of several SEM images suggests that the fractured CNA nanocomposite film does not break parallel to the layers while the LRD nanocomposite does.[5]

5.2.3 Birefringence Investigations

The microscopic structure of the multilayered films was characterized by polarized optical microscopy, which showed differences in birefringence in each plane (Figure 5.7). From our experience with other nanocomposite films such as LRD60%-PEO40% at the same salt concentration[5] we would expect to see no birefringence in the x-z plane and strong birefringence in the x-y plane which is predominantely coming from clay platelets that are hierarchical ordered on all length scales. For CNA-PEO films at higher polymer concentration and different salt concentration we would expect and observe birefringence in both planes resulting from both the polymer and the clay.[67] When comparing films ideally one would like to limit the number of parameters being altered in the films made from solutions. However this is often impossible due in large part to the very complicated phase diagrams of these complex systems in aqueous solutions that may require change of parameters (such as salt, excess polymer) to prevent the solution/dispersion from phase separation.[104]

The x-z plane (see Figure 5.1 for plane, Figure 5.7) for CNA60%-PEO40% films shows only few speckles which are due to the birefringence observed from predominantly single large clay platelets and clusters. With increasing temperatures in a range from 25 to 200 degree C the overall birefringence is only somewhat reduced probably due to melting of any oriented polymer. To the eye no significant differences in birefringence are visible. Observation of the exposed edge of the film, the x-y plane, shows a highly birefringent pattern even after annealing an hour at 200 degree C. The total birefringence of the film is dominated by the orientation of the clay platelets and the polymer within the sample. For CNA60%-PEO40% studied here the polymer contribution to the total birefringence is either small or “not visible” to the eye, suggesting that optical microscopy is not the best method for detecting PEO crystallites that may be confined between the layers.

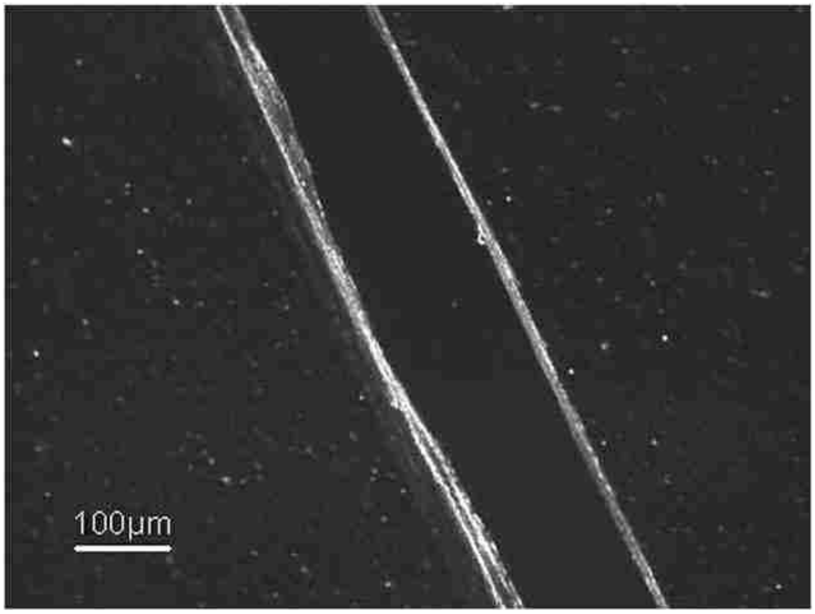

Figure 5.7. Representative optical microscopy image from a nanocomposite film with a cut surface. Crossed polarizers are used. A small section of a one layered film was removed to expose the side plane. The film is shown at room temperature after being heated and cooled. Birefringent speckles and birefringence of the side plane do not disappear at high temperatures. This film has been heated and cooled to remove any birefringence coming from additional shear effects during the scratching or cutting of the film.

5.2.4 PEO Crystallinity in the Film: DSC Experiments

While the crystallinity of various bulk PEO nanocomposites at low clay concentrations has been studied in the past extensively[1, 2, 115] here we focus on supramolecularly oriented and anisotropic materials at high clay concentrations. The polymer and clay composition of our multilayered CNA60%-PEO40% films is confirmed by DSC experiments. The pure CNA clay as obtained from Southern clay has ca. 2% of "impurities" based on the dry material that is detected in TGA thermograms as a weight loss in nitrogen atmosphere at around 150^{o}C.

DSC data shown in Figure 5.8 are normalized to 1 mg content of PEO; therefore the enthalpic change for PEO from the nanocomposite is corrected to 97 J/g (i.e., 39:0.4 ≈ 97). If we consider the pure PEO to be 100% crystalline[109] then our results from the nanocomposite films show that 52% of the total polymer content is crystalline and 48% is amorphous (Figure 5.8). These results suggest that the high clay concentration is sufficient to suppress 48% of the PEO crystallization in the film. We expected that the CNA clay adsorbed polymer could be amorphous since it is confined to the clay surface and cannot move easily. The excess polymer would then form most of the crystalline phase. However qualitatively none of the PEO crystallites are visible with optical microscopy thus PEO crystallites must be either too small as to be detected by optical microscopy or there is polymer crystallinity confined within the clay layers.

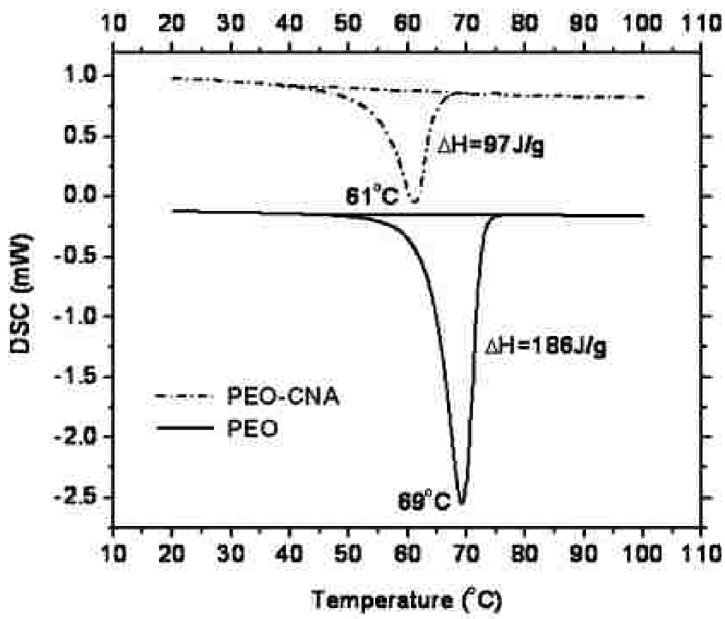

Figure 5.8: Normalized DSC plots for crystalline melting of the pure PEO polymer (y = DSC data) and of the polymer nanocomposite CNA60%-PEO40% (y = DSC+1.1mW shifted). The heating rate used was 5°C/min in nitrogen.

It has been found in previous work that montmorillonite clay can adsorb ca. 0.3 g PEO/g of CNA clay. For a film with CNA60%-PEO40% the adsorbed amount is then calculated to be 45% of the total polymer content.[2, 45, 46] This is more or less in agreement with our DSC results which give 48% for amorphous polymer. Since the presence of salt may influence the crystal formation of PEO as has been observed by other groups in the past[50, 51] we believe that discrepancies between the 45% calculated from literature and the 48% from our DSC data may result from the presence of salt. At the same time, examining the DSC traces shown in Figure 5.8 one may notice also that the melting temperature of PEO crystals in the clay composite was lowered significantly as compared to that of the pure PEO sample (consider for example the peak temperatures), pointing to an inhibitory effect of salt during PEO crystallization in the clay matrix. The difference in melting temperature however is too large to come from the presence of salt alone but may also be attributed to differences in crystalline structures.[49] These interesting peculiarities will be investigated in more detail in the future.

Differences in crystallinity of the CNA60%-PEO40% films presented here (52%) compared to the same composition LRD60%-PEO40% films studied in the past (near 0%)[5] show that clay size dependence leads to unexpected but reproducible phenomenology at the nanoscale.

5.2.5 XRD Experiments

X-ray diffraction patterns of CNA60%-PEO40% films and from pure CNA and pure PEO reference samples are shown in Figure 5.9. Although the polymer-clay solutions from which the nanocomposite films are made of, are completely exfoliated (no peaks visible) XRD confirms the dried multilayered films are highly structured. The XRD reflections predominantly correspond to the PEO intercalated clay suggesting the presence of stacked layers. Significant peaks from crystallized PEO are missing although DSC suggests the presence of PEO crystallinity. The first peak corresponds to a d-spacing of d = 17.8 Angstroms, a result in agreement with what has been found in literature for other polymer nanocomposites.[46] The XRD pattern of CNA60%-PEO40% looks similar to other melt intercalated PEO-montmorillonite nanocomposites (even those at other clay content) found in literature.[46] Similar to the SANS data shown in Figure 5.2, the XRD averages over the sample volume, thus both SANS and XRD do not show the hierarchical arrangements as microscopy does.

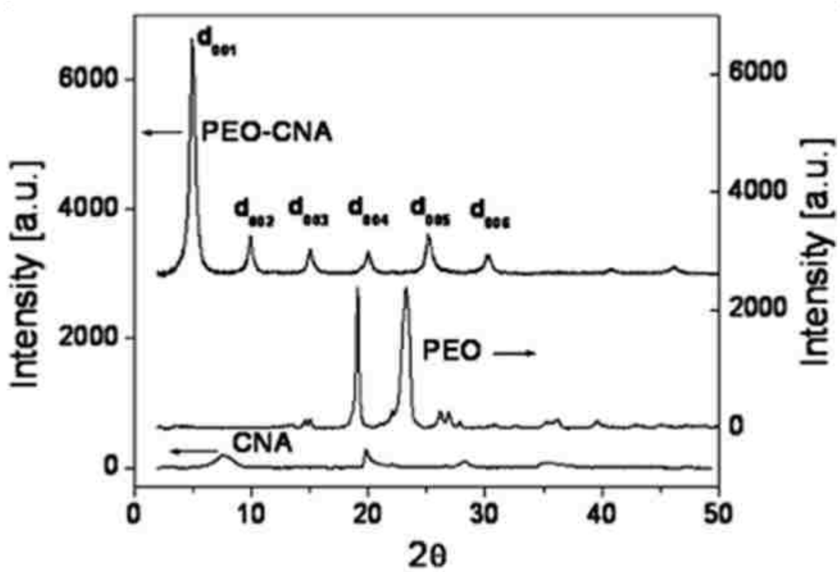

Figure 5.9: X-ray diffraction patterns of CNA60%-PEO40% film (shifted +3000 intensity units), presented along with the patterns of the pure CNA and the pure PEO reference samples.

5.3 Conclusions

The main difference between the nanocomposites obtained via melt and solution intercalation of previous studies[45, 46] and the nanocomposites studied here is this supramolecular order and hierarchical structuring we observe. On the nanometer length scale a high degree of order is reflected in the XRD pattern but AFM is necessary to visualize the supramolecular structure. Compared to work done in the past our nanocomposite films have highly anisotropic structure from the nanometer, via micrometer to the cm length scale while many previously reported nanocomposites have only local ordered structures. Overall our results suggest the re-intercalation of clay platelets in films made from exfoliated polymer-clay solutions as well as the possibility to supramolecular order and hierarchical structure on the nanometer, via micrometer to the centimeter length scale. The structure and properties of our multilayered nanocomposite films may provide a useful route in the preparation of novel materials such as anisotropic solid state electrolytes with enhanced ionic conductivity in only one direction.

CHAPTER 6
STRUCTURE AND THERMAL PROPERTIES OF MULTILAYERED PEO-LAPONITE THIN FILMS*

In this chapter the structures and thermal properties of a series of new nanocomposite poly(ethylene oxide)-laponite films are investigated by differential calorimetric and thermal analysis and complemented by microscopy and X-ray diffraction experiments. The crystalline structures of the nanocomposite multilayered films can be tuned by controlling the composition, polymer Mw and the water content. We study the concentration, polymer Mw and humidity dependence of polymer crystallinity in selected nanocomposite multilayered films. The exact sample preparation and history are important in controlling structure and properties and in developing new materials. Complementary microscopy is used to monitor the structural changes.

6.1 Experimental Procedures

6.1.1 Sample Preparation

Laponite-RD (LRD), a synthetic hectorite type clay (Southern Clay Products) was used as received without any further purification. Poly(ethylene oxide) (PEO) with molecular masses of 100 kg/mol, 300 kg/mol, 600 kg/mol, and 1000 kg/mol were purchased from Polysciences Inc. Multilayered films were prepared via gel/solution exfoliation as described in previous work.[4-6] Specifically for this work, gels and solutions were manually spread onto glass slides layer-by-layer and dried at 25^{o}C in desiccators and under vacuum. Following this procedure two distinct series of LRD-PEO multilayered films were produced: a first series comprised of samples containing PEO of 1000k Mw in different ratios with the LRD clay (LRD-PEO 60:40, 40:60,

---

* Reproduced in part with permission from Polymer, E. A. Stefanescu, P. J. Schexnailder, A. Dundigalla, I. Negulescu, G. Schmidt, Structure and thermal properties of multilayered Laponite/PEO nanocomposite films, **2006**, 47, 7339-7348. Copyright © 2006 Elsevier.

15:85) (Table 6.1), and a second series of samples containing 60% laponite clay and 40% PEO (w/w) of different molecular weights (100k, 300k, 600k, 1000k Mw) (Table 6.1). All the samples that were to be exposed to moisture at room temperature were placed under vacuum for 48 hours; the vacuum was removed by the use of argon as an inert media. Films were then transferred to desiccators containing a beaker with water as a source of humidity. The desiccator was hermetically closed and the films were removed after precise periods of exposure to humidity (e.g. 3h, 6h, 12h, etc).

6.1.2 Microscopy Experiments

Optical microscopy was performed using an Olympus BX51TF microscope with crossed polarizers. Scanning Electron Microscopy (SEM) experiments were performed using a Cambridge 260 Stereoscan Electron Microscope. Only representative images are presented. The layered textures of the selected x-y SEM images of LRD60%-PEO40%-X were not uniform. LRD60%-PEO40%-1000 was calculated to have an average dimension of $d_{SEM} \approx 0.3 \pm 0.17$ μm per layer. When sample preparation and history are kept the same then duplicate measurements on all instruments showed excellent reproducibility with a relative uncertainty of ca. 5 %.

6.1.3 DSC and TGA Experiments

DSC experiments were performed using a TA 2920 MDSC instrument. Samples of 6.5–10mg were subjected to analysis using a heating rate of 20^{o}C/min in two successive heating cycles. In all DSC traces, positive features correspond to exothermic processes, and negative features correspond to endothermic processes. For each measurement, a virgin nanocomposite sample was used in the first heating run followed by cooling and a second heating run. Thermogravimetric analyses (TGA) was performed in nitrogen atmosphere with a heating rate of 20^{o}C/min. Only virgin samples of ca. 7-11mg were subjected to thermogravimetric analysis. TA

Universal Analysis software was used for the integration and processing of all curves resulted from both instruments. Duplicate measurements on both instruments showed excellent reproducibility with a relative uncertainty of less than 5 % when sample preparation and history were kept the same.

6.2 Results and Discussion

6.2.1 Concentration Dependence of Structure and Thermal Properties

In a first series of experiments, we show the concentration dependence of DSC of representative nanocomposites with the same sample history (Figure 6.1 and Table 6.1). Measurements are shown for LRD-Y-PEO-Z-1000 films containing 60%, 37.5% and 15% of LRD by weight. As expected, a large difference in the heat of fusion results in different crystallinities (Table 6.1) and the peaks observed in Figure 6.1 shift to lower melting temperatures with increasing clay concentration. If we assume that any free excess polymer that is not attached to the clay is mostly crystalline then the crystallinity for LRD40%-PEO60%-1000 and LRD15%-PEO85%-1000 indicates that these two samples may contain very high amounts of excess polymer. The adsorbed and intercalated polymer is assumed to be mostly amorphous suggesting a maximum of 22% PEO, and 6% PEO that may be adsorbed to the clay surfaces. Figure 6.2 shows optical microscopy of the films discussed above as well as a reference pure polymer film. Complementary to the DSC results, the crystallinity increases with increased polymer concentration. In addition to the expected large spherulites that are observed for the reference pure PEO film (Figure 6.2d) small "dots" are visible for the nanocomposites (Figure 6.2b,c) suggesting differences in nucleation and growth of PEO crystals.

Table 6.1: Nanocomposite film composition and crystallinity as obtained from DSC measurements.

SAMPLE NAME	LRD Conc. (%)	PEO Mw kg/mol	% Crystallinity (+/-5%)
LRD60%-PEO40%-X			
LRD60%-PEO40%-100	60	100	1.93
LRD60%-PEO40%-300	60	300	1.12
LRD60%-PEO40%-600	60	600	1.20
LRD60%-PEO40%-1000	60	1000	1.57
LRD-Y-PEO-Z-1000k			
LRD60%-PEO40%-1000	60	1000	1.57
LRD40%-PEO60%-1000	40	1000	78
LRD15%-PEO85%-1000	15	1000	94

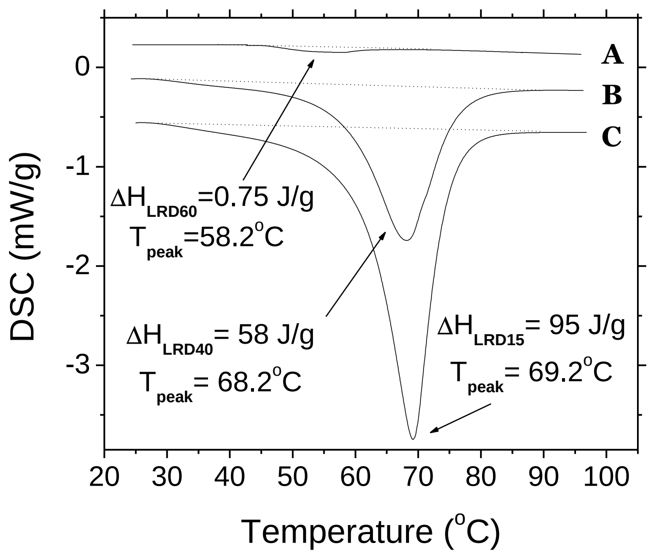

Figure 6.1: Normalized DSC traces for the melting of nanocomposite films with different composition. (A) LRD60%-PEO40%-1000 kg/mol, (B) LRD40%- PEO60%-1000 kg/mol, and (C) LRD15%-PEO85%-1000 kg/mol.

LRD60%-PEO40%-1000 films indicate very low crystallinity in DSC, which cannot be detected with polarized optical microscopy. This low crystallinity is due to the high clay content but is also influenced by the complete clay exfoliation and supramolecular structural orientation. The origin and specific structural details of LRD60%-PEO40% have been described elsewhere.[5]

Most recently we have discovered that crystallinity changes after ca. one year, especially after repeated exposure of films to humidity and UV. These long-term studies, however, are not the subject of this work.

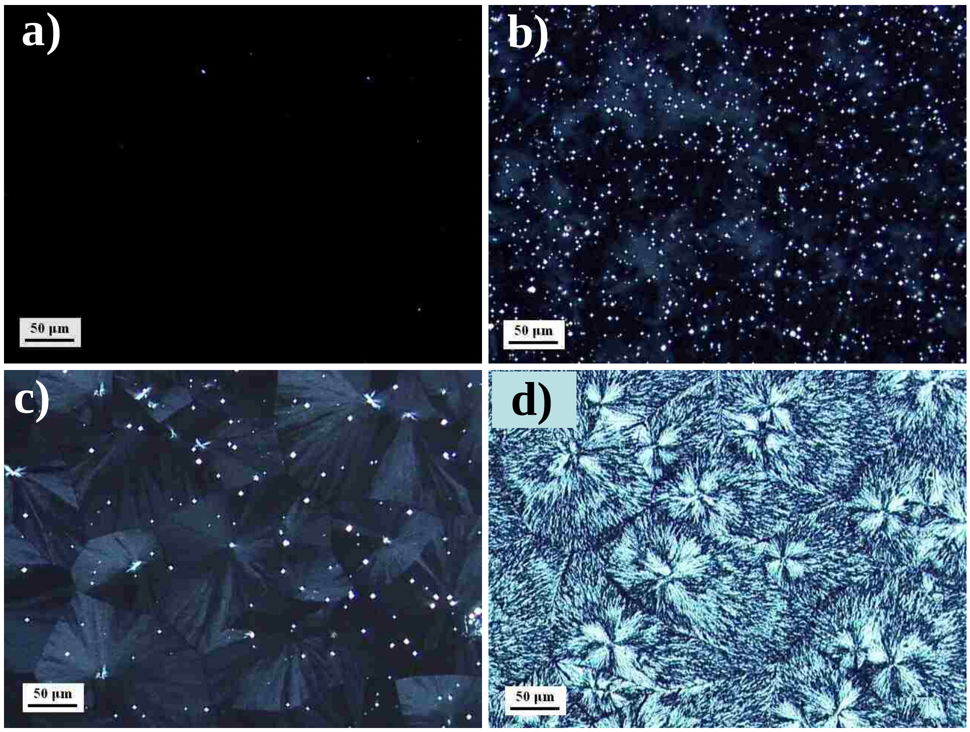

Figure 6.2: Polarized optical microscopy images from fresh made nanocomposite films of different composition. The top surface of films is shown. a) LRD-60%-PEO-40%-1000 Kg/mol, b) LRD-40%-PEO-60%-1000 kg/mol, c) LRD-15%-PEO-85%-1000 kg/mol, d) reference pure PEO-1000 kg/mol.

In Figure 6.3 we investigate the composition dependent structure as obtained from SEM. Images in the x-y plane (side surface fracture) show that the occurrence of micron size layers is strongly dependent on clay content. The definition of planes in Figure 6.3d is also shown for better comparison, but the physical picture of general platelet orientation as obtained from our past study[5] corresponds only to LRD60%-PEO40%-1000. Although all samples were made from exfoliated polymer-clay solutions, LRD40%-PEO60%-1000 and LRD15%-PEO85%-1000 exhibited fewer or no layers, suggesting the clay concentration is critical in layer production. X-Ray Diffraction (XRD) results are shown in Figure 6.4.

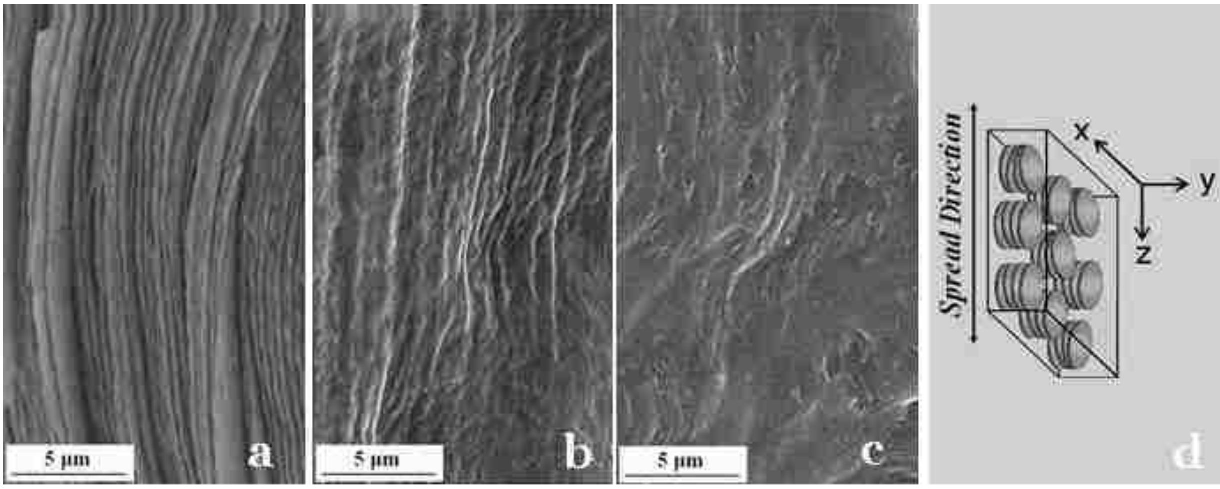

Figure 6.3: SEM images from fresh made nanocomposite films of different composition. The x-y plane (side surface) of films is shown. **a)** LRD-60%-PEO-40%-1000 kg/mol, **b)** LRD-40%-PEO-60%-1000 kg/mol, **c)** LRD-15%-PEO-85%-1000 kg/mol. The definition of planes is shown for better comparison of figures **(d)**.

At high clay concentrations and dense packing, platelets have no other choice than to stack and order, producing many regular XRD reflections that correspond to the PEO intercalated and stacked clay. Such regular reflections have been observed in the past for other clay nanocomposites. At higher polymer concentrations such as LRD40%-PEO60%-1000, XRD reflections still occur at the same q but their intensity is much weaker, suggesting the presence of fewer stacked clay domains in the polymer matrix. LRD15%-PEO85%-1000 shows no more regular reflections but instead peaks that can be correlated to reflections from the crystalline polymer (Figure 6.4b). LRD15%-PEO85%-1000 has exfoliated clay platelets in the polymer matrix but the clay platelets are too far apart and too randomized to produce higher order reflections. Nevertheless on the nanometer length scale as detected by Small Angle Neutron Scattering (SANS) we have shown that on average even these clay platelets orient in the spread direction.[67]

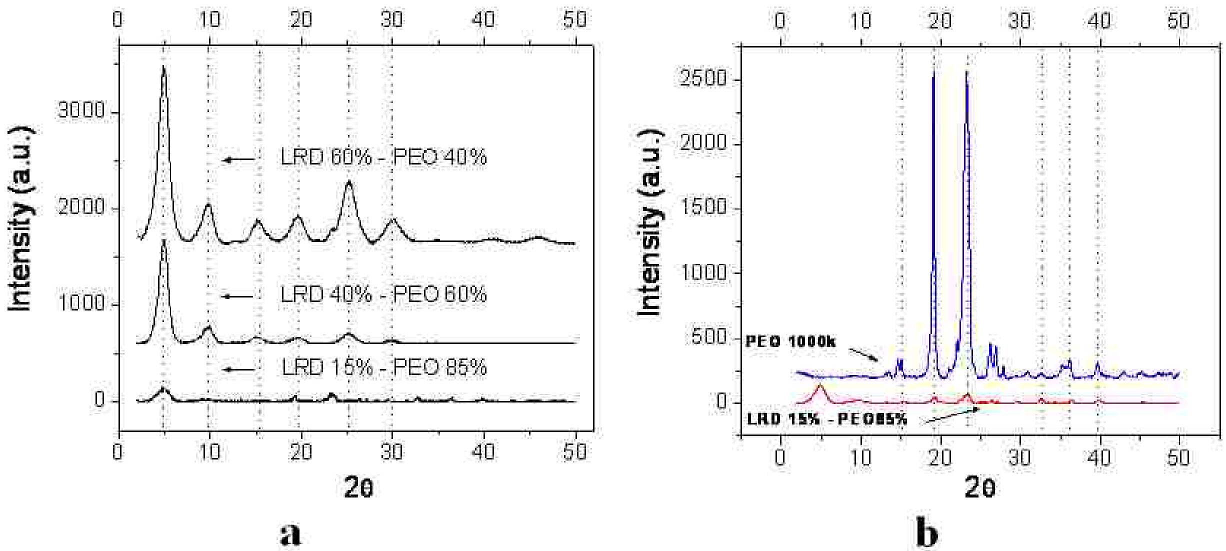

Figure 6.4: a) X-ray diffraction patters for LRD-60%-PEO-40%-1000 kg/mol, LRD-40%-PEO-60%-1000 kg/mol, and LRD-15%-PEO-85%-1000 kg/mol (see also Table 6.1); b) A comparison of the pure PEO 1000 kg/mol and LRD-15%-PEO-85%-1000 kg/mol X-ray diffraction curves.

6.2.2 Polymer Mw Dependence of Thermal Properties

We have studied the micro- and nano-structures of selected LRD60%-PEO40% nanocomposite films in the past and have shown that the solution structure and processing conditions strongly influence the overall morphology of the dried films.[5] The collapse of a polymer-clay network structure as the solution dries leads to either highly oriented thick layers in the dried film (Figure 6.5a) or very fine layers (Figure 6.5b). The number of multilayers can only be estimated since one single spread produces multiple layers on large length scales.[5] Only representative SEM images of multilayered films in the x-y planes (side surfaces) are shown in Figure 6.5. On the micron length scale, the layered structures are dependent on the polymer Mw.[5] Among many other parameters, we believe that the sample preparation and the resulting structure strongly influence the crystallinity. For example not completely exfoliated nanocomposites containing pure clay aggregates will also have more excess PEO that is not bound to the clay and that will crystallize.

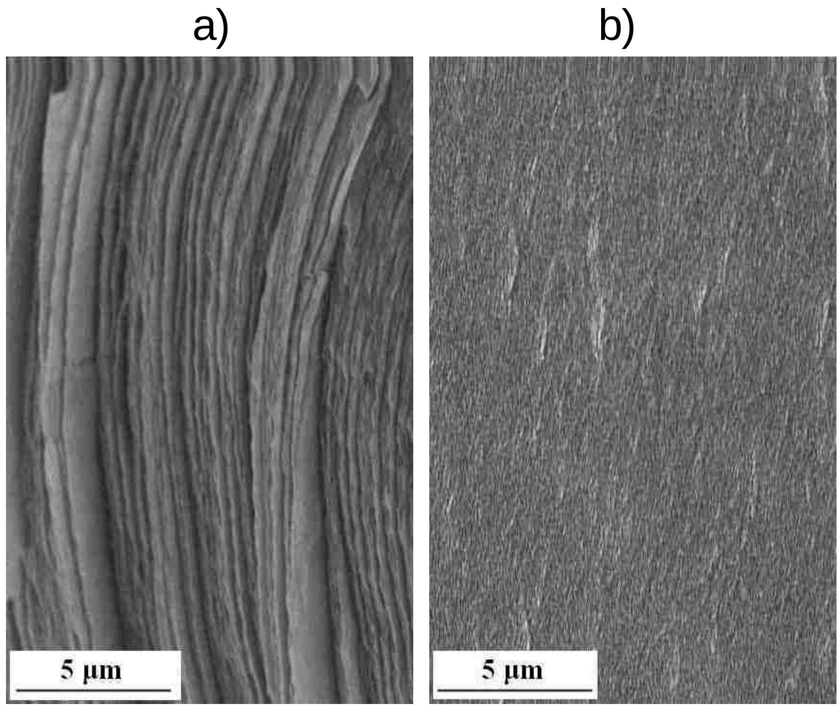

Figure 6.5: SEM images from nanocomposite films of same composition but different polymer Mw. The x-y planes (side surfaces) of films are shown: a) LRD-60%-PEO-40%-1000 kg/mol, b) LRD-60%-PEO-40%-100 kg/mol.

Figure 6.6 represents the polymer Mw dependence of DSC data from a) nanocomposite multilayered films at a constant composition of polymer and clay LRD60%-PEO40%-X and from b) reference pure PEO films (Table 6.1). All nanocomposite films have the same sample history regarding sample preparation. Comparison between our results and studies from literature are difficult due to different sample preparation techniques and sample history, which are some of the parameters that strongly influence adsorbed water content. The DSC curves shown have been normalized to the amount of 1mg LRD60%-PEO40%-X and shifted for better visualization. DSC thermograms were obtained in the second heating cycle of the DSC measurement to avoid artifacts that could influence the results. This procedure removes mechanical tensions that may originate from the layering process during film formation. The same trends are observed in the first heating cycle (not shown here) but with much larger fluctuations in crystallinity between the first heating cycles compared to the second ones.

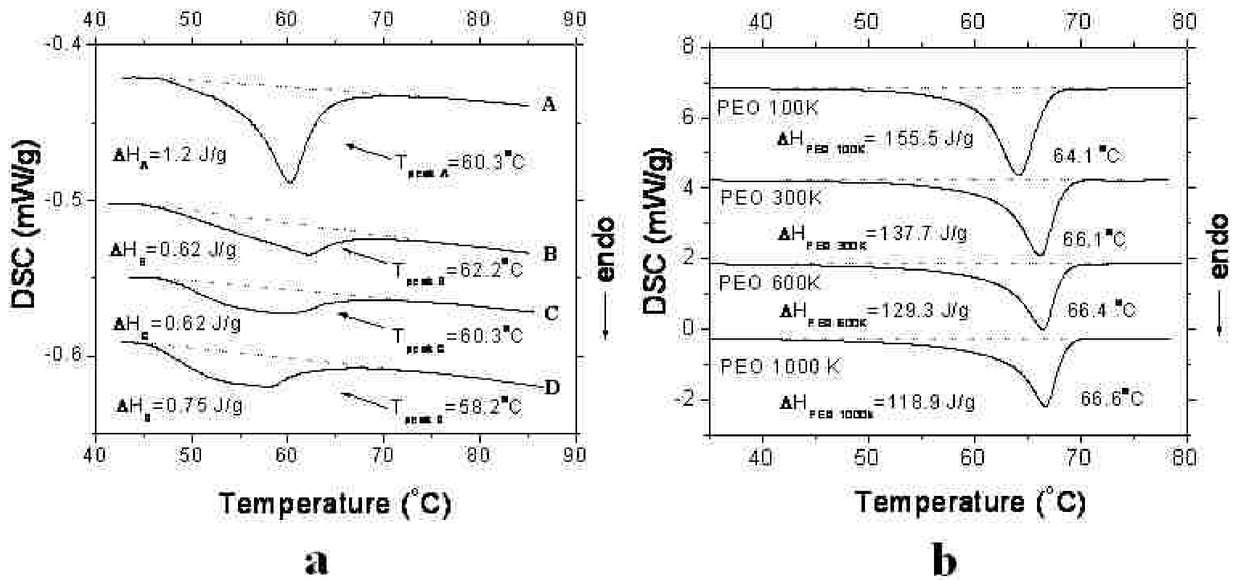

Figure 6.6: Polymer Mw dependence of normalized DSC traces for the melting of: **a)** LRD-60%-PEO-40% samples containing polymer of different molecular weights (A – 100 kg/mol, B – 300 kg/mol, C – 600 kg/mol, D – 1000 kg/mol) (see Table 6.1); and **b)** pure PEO polymer of different molecular weights.

From the DSC curves shown in Figure 6.6 the crystallinity of samples was calculated and included in Table 6.1. The melting temperature of the nanocomposites (Figure 6.6a) slightly decreases with the increase in polymer Mw, the only exception from this being the sample with LRD60%-PEO40%-100. From solution studies we know that LRD60%-PEO40%-100 is the only sample where the polymer chains are too short to interconnect the clay platelets in solution.[40] This sample does not show any significant shear-orientation of platelets or stretching of polymer chains in solution. During the film spreading and drying process LRD60%-PEO40%-100 does not build the type of supramolecular structured layers as the other samples do (see Figure 6.5). Since the polymer chains are not crosslinked to several platelets in solution, they do not remain elongated and stretched during the film spreading procedure. Any elongated polymer chains during shear will recoil back fast in solution. The predominant structural shear-orientation in the film that we have observed previously[67, 77, 104], comes from the collapse of the network structure in solution and the clay platelet orientation during solvent evaporation. The shear forces during the spreading process are not strong enough and too short to keep the polymer chains stretched. Thus these “100 kg/mol” long polymer chains have sufficient space and flexibility to recoil from any deformed position and crystallize. This may be one reason why LRD60%-PEO40%-100 does not follow the trend observed in Figure 6.6a and why we observe a higher crystallinity for the LRD60%-PEO40%-100 than for all other samples at the same composition (Table 6.1).

In the series LRD60%-PEO40%-X with X=300, 600, and 1000 kg/mol crystallinity is small but increases with increasing polymer Mw and polymer chain length (linear polymers). In all these samples, polymer chains are long enough to interconnect the clay platelets in solution. During the film spreading and drying process clay platelets are oriented, polymer chains are stretched, and supramolecular structured layers are observed on all length scales.[40, 41] Since the clay particles act as multifunctional cross-linkers, polymer chains may remain stretched during the film drying process. We do not know how many polymer chains and loops are attached to each clay platelet. These adsorbed chains and small loops will not crystallize but remain amorphous. Long polymer chains will have more interconnections with the clay particles than short polymer chains whose dangling ends are not network active and cannot be stretched during shear. Dangling ends may move more easily, they but cannot phase separate during the film drying process because they are connected to the clay. Short dangling ends may recoil thus increasing the number of defects in a developing PEO crystal, while long dangling ends may crystallize. Nevertheless as shown in Figure 6.6a, long polymer chains seem to better crystallize than the short chains.

Another interpretation of the results shown in Figure 6.6 takes into account potential water present in the nanocomposite films. When polymer chains are adsorbed to the clay layers, water molecules initially present on the silicate surfaces and galleries are displaced to accommodate the polymer chains. This adsorption takes place in the solution as well as during the drying of the films.[2] Although the nanocomposite films have been dried in vacuum, some water molecules may still be trapped in the films. Displaced water molecules from the clay surfaces, or water molecules from the precursor solutions, are likely trapped within the PEO crystallites; shifting the melting transition to lower temperatures.[2] The calculated values for crystallinity shown in Table 6.1 are very similar but trends can be reproduced when measurements are repeated on "freshly prepared" samples. It is possible that more water molecules are present in a nanocomposite film when the polymer Mw is high, which leads to a more pronounced shifting of the melting transition to lower temperatures. In the presence of clay nano-particles, high polymer Mw has a more disordered/amorphous structure and could accommodate more water molecules. However, since the overall differences in melting temperature are very small the amounts of incorporated water must be very small too.

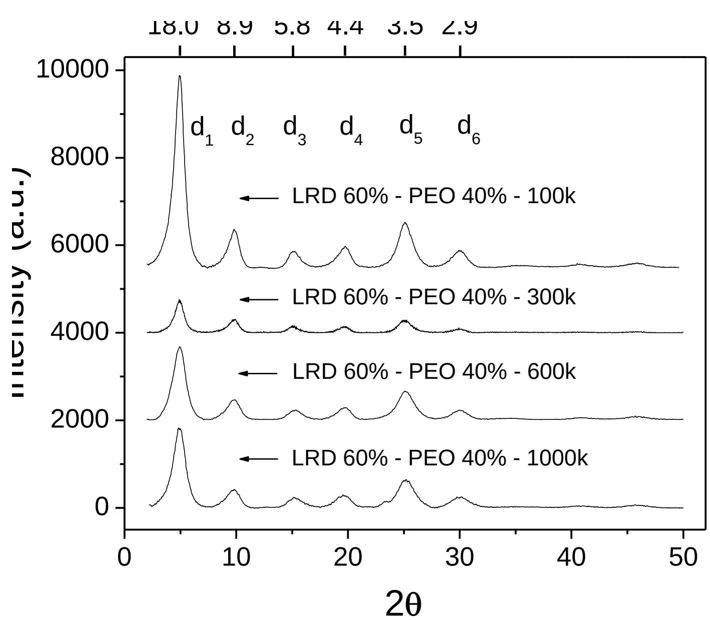

Figure 6.7: X-ray diffraction patters for LRD-60%-PEO-40%-X samples containing different Mw polymers (A – 100 kg/mol, B – 300 kg/mol, C – 600 kg/mol, D – 1000 kg/mol) (see Table 6.1)

Reference DSC experiments on pure PEO samples are presented in Figure 6.6b. As expected we observe a decrease in polymer crystallinity with increasing polymer Mw. Crystallinity decreases, because long entangled chains have difficulties in reaching and maintaining a proper alignment necessary for crystallization. With the increase of polymer Mw, the melting temperature of the polymer slightly increases due to a higher inertia of longer chains towards movement in the melting process. Figure 6.7 shows XRD from dry samples of LRD60%-PEO40%-X. Regular XRD reflections for all samples correspond to the PEO intercalated and stacked clay. Overall, the results suggest that there is not much polymer Mw dependence present. The first peak in XRD corresponds to a d-spacing of 17.8 Angstroms, a result in agreement with what has been found in literature. Such regular reflections have been observed in the past for many other clay nanocomposites.[46]

6.2.3 Humidity Dependence of Thermal Properties

While the nanoparticles certainly affect the motion of the adsorbed polymer chains in the nanocomposite film, the presence of the water molecules and the kinetics of water adsorption strongly influence the polymer crystallinity in the multilayered films. In an effort to understand these effects better, we have examined the kinetics of water adsorption as function of polymer Mw.

Figure 6.8a,b,c shows DSC curves for LRD60%-PEO40%-X samples exposed to humidity. The sample preparation, history and the exposure time to humidity were kept the same and duplicate measurements guaranteed reproducibility. Dry samples were exposed to humidity for 3, 6, 12, 24 and 48 hours. Overall, the same trends are observed for all nanocomposite films. Adsorption of water decreases crystallinity gradually until it disappears almost completely, leaving the polymer amorphous. A decrease in the polymer melting temperature can also be noticed with increased water adsorption. This may be due to smaller crystallite sizes but possibly also to the heat capacity of present water molecules surrounding the polymer.

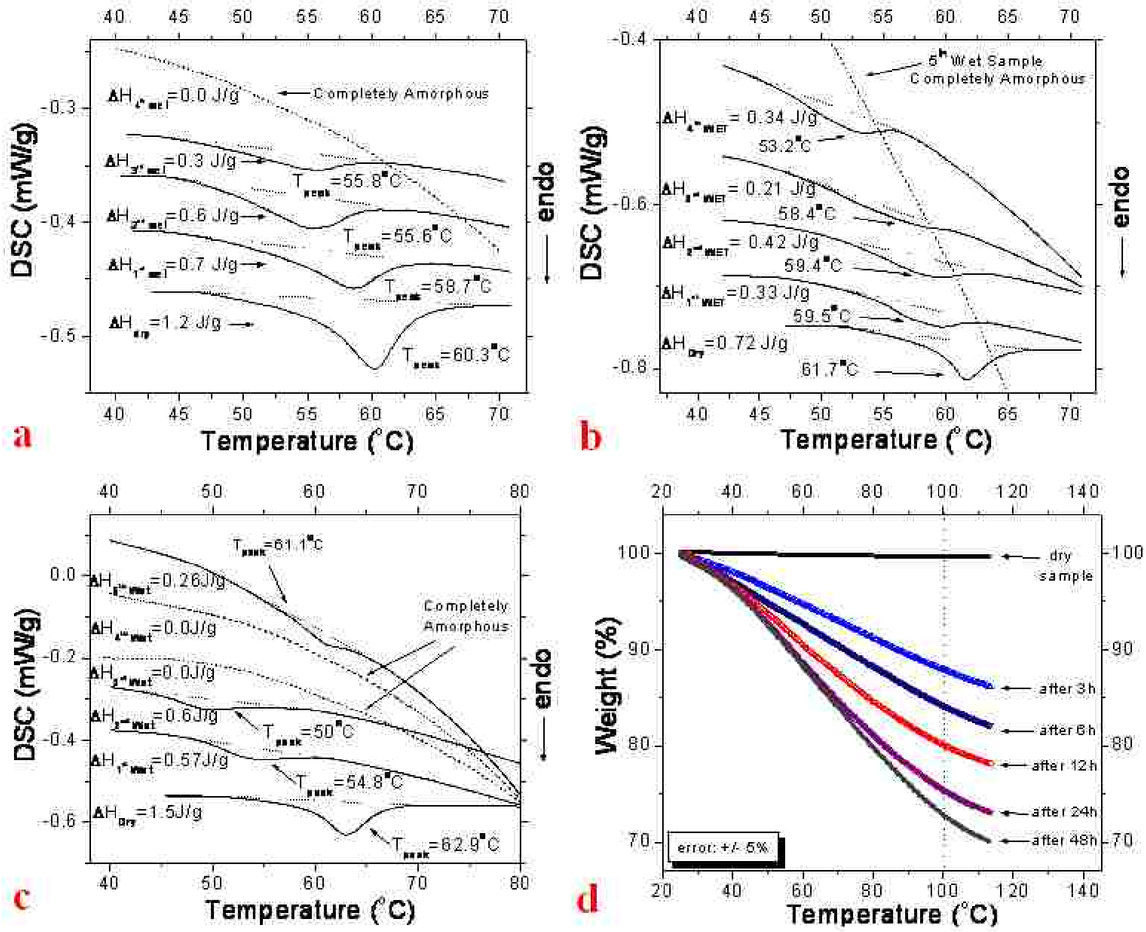

Figure 6.8: Thermal analysis of nanocomposites exposed to humidity ("dry" sample - not exposed to humidity, 1st wet sample after 3h exposure to humidity, 2nd wet sample after 6h exposure to humidity, 3rd wet sample after 12h exposure to humidity, 4th wet sample after 24h exposure to humidity, 5th wet sample after 48h exposure to humidity). **(a)** DSC traces for LRD-60%-PEO-40%-100 kg/mol, **(b)** DSC traces for LRD-60%-PEO-40%-300 kg/mol, **(c)** DSC traces for LRD-60%-PEO-40%-1000 kg/mol, **(d)** Thermogravimetric analysis of LRD60%-PEO40%-1000 kg/mol. exposed to humidity

Distinguishable differences in DSC curves for the individual samples are attributed to the polymer Mw which influences the water adsorption and the kinetics of the polymer to reach a completely amorphous state. Although the LRD60%-PEO40%-1000 sample reaches an amorphous state after 12 hours, we observe a small peak in the heating curve for this sample after 48 hours of exposure to humidity. This trend is reproducible when the experiment is repeated. It seems like this sample has gained back some crystallinity, which may be due to internal rearrangements of the PEO chains.

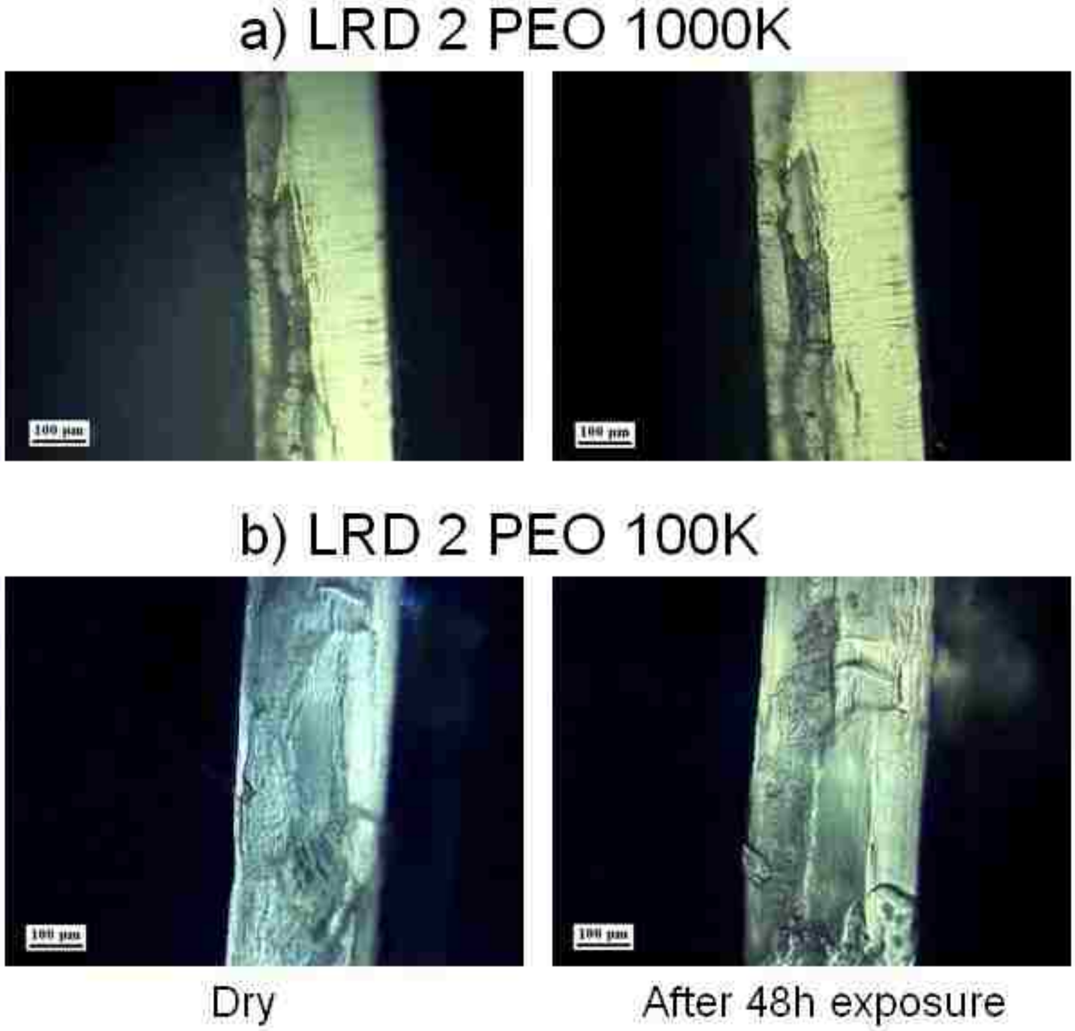

Figure 6.9: Polarized optical microscopy images from nanocomposite films of same composition but different polymer Mw. The x-y planes (side surfaces) of films are shown. **a)** LRD-60%-PEO-40%-1000 kg/mol, **b)** LRD-60%-PEO-40%-100 kg/mol

Upon reaching critical water content the motions of PEO chain backbones are strong enough to diffuse, twist and bend into crystallites. Surprisingly the lower polymer Mw LRD60%-PEO40%-300 sample needs 48 hours of exposure to humidity to completely loose crystallinity (Figure 6.8b). General trends and differences between nanocomposites with different polymer Mw were also monitored with TGA (Figure 6.8d and Table 6.2). The weight loss as function of temperature shows the influence of water on the nanocomposite weight. Up to ca. 30% of water can be adsorbed in the film when measured at 100 degree C. The reversible swelling of the film x-y plane as monitored by polarized optical microscopy is shown in Figure 6.9. Fractured surfaces are shown for dry films and the same films exposed to humidity. While the x-z film plane (top surface) is black under crossed polarizers (see Figure 6.2a), the x-y plane is strongly birefringent due to aligned polymer and clay particles. Upon exposure to humidity a 260 micron thick film will swell up to 290 microns (Figure 6.9). On a qualitative level no significant polymer Mw dependence has been observed in swelling behavior or TGA. Further experiments on many samples are necessary in order to understand the swelling behavior on a quantitative level.

Table 6.2: Weight loss percentage at 100°C as resulted from the TGA measurements.

Sample (exposure to humidity)	**Weight loss (%) LRD60-PEO40-1000**	**Weight loss (%) LRD60-PEO40-300**	**Weight loss (%) LRD60-PEO40-100**
dry sample (no humidity)	0.39	0.37	0.34
1st wet sample (after 3h)	12.15	13.25	10.1
2nd wet sample (after 6h)	15.88	15.06	14.36
3rd wet sample (after 12h)	19.94	16.98	16.68
4th wet sample (after 24h)	24.61	19.11	22.26
5th wet sample (after 48h)	27.23	30.05	26.2

6.3 Conclusions

We have shown that the crystalline structure of the nanocomposite multilayered films can be tuned by controlling the composition, polymer Mw and the water content. We have studied the concentration, polymer Mw and humidity dependence on polymer crystallinity and have found that sample preparation and history are important in controlling structure and properties.

Much of the layer formation is not well understood. For example, comparable PEO-laponite and PEO-montmorillonite nanocomposite films show a very similar d-spacing between polymer intercalated clay stacks, when detected by diffraction measurements[5, 67, 77] but the layer nanostructure is very different when observed with microscopy.[5, 67] To date we can only speculate about the origins of such effects.

Our preliminary results on the design of nanocomposite solutions and gels for film preparation are used to rapidly evaluate new and promising candidate materials for the fabrication of other hierarchical structured films. The optimization of the film fabrication techniques will guide the fabrication of transparent and multilayered films over the whole laponite concentration range. This will allow for characterizing the critical parameters responsible for the appearance or disappearance of polymer crystallinity.

CHAPTER 7
CONCLUSIONS AND FUTURE WORK

7.1 Conclusions

The structure, interactions and properties of PEO-laponite and PEO-montmorillonite nanocomposite hydrogels and multilayered films have been investigated by means of microscopy, rheology, thermal analysis and X-ray diffraction measurements. In order to better understand these complex systems the structures were examined as a function of polymer molecular weight, clay type and size, polymer and clay concentrations, nature of salt added in the system, and sample preparation method.

It has been shown that in solution a network structure forms between water molecules and polyethylene oxide chains corresponding to two or three water molecules associated with each $–CH_2CH_2O-$ unit through hydrogen bonding (Figure 7.1).[73, 75] When ionic salts are added to the polymer solution the hydrogen bonding is disrupted by the ions.[72] The disruption of the PEO-water network allows the polymer chains to better interact with the montmorillonite platelets. Li cations can spread in the system and coordinate to oxygen containing groups more strongly and uniformly due to their smaller ionic radius and increased diffusion ability when compared to Na cations (Figure 7.1). Due to the stronger interaction with the water molecules, Li cations are capable of screening the water-PEO hydrogen bonding to a greater extent than Na cations, triggering the improvement of the polymer-clay interactions.

When comparing laponite-based gels with montmorillonite-based gels of similar compositions it has been observed that laponite dispersions form stronger networks than montmorillonite dispersions. Due to their small diameter, for a given mass, completely exfoliated laponite platelets provide a very large effective surface available for coordination with the incoming PEO chains. Having diameters three to four times larger, exfoliated montmorillonite clay provides a much smaller coordination surface, for the same mass. This decreased effective surface leads to the formation of fewer polymer-clay cross-links in the system, which further leads to the appearance of weaker polymer-clay networks, with many free uncoordinated PEO chains. The weaker network is the reason why montmorillonite rich gels exhibit viscosities and shear moduli lower than laponite rich gels.

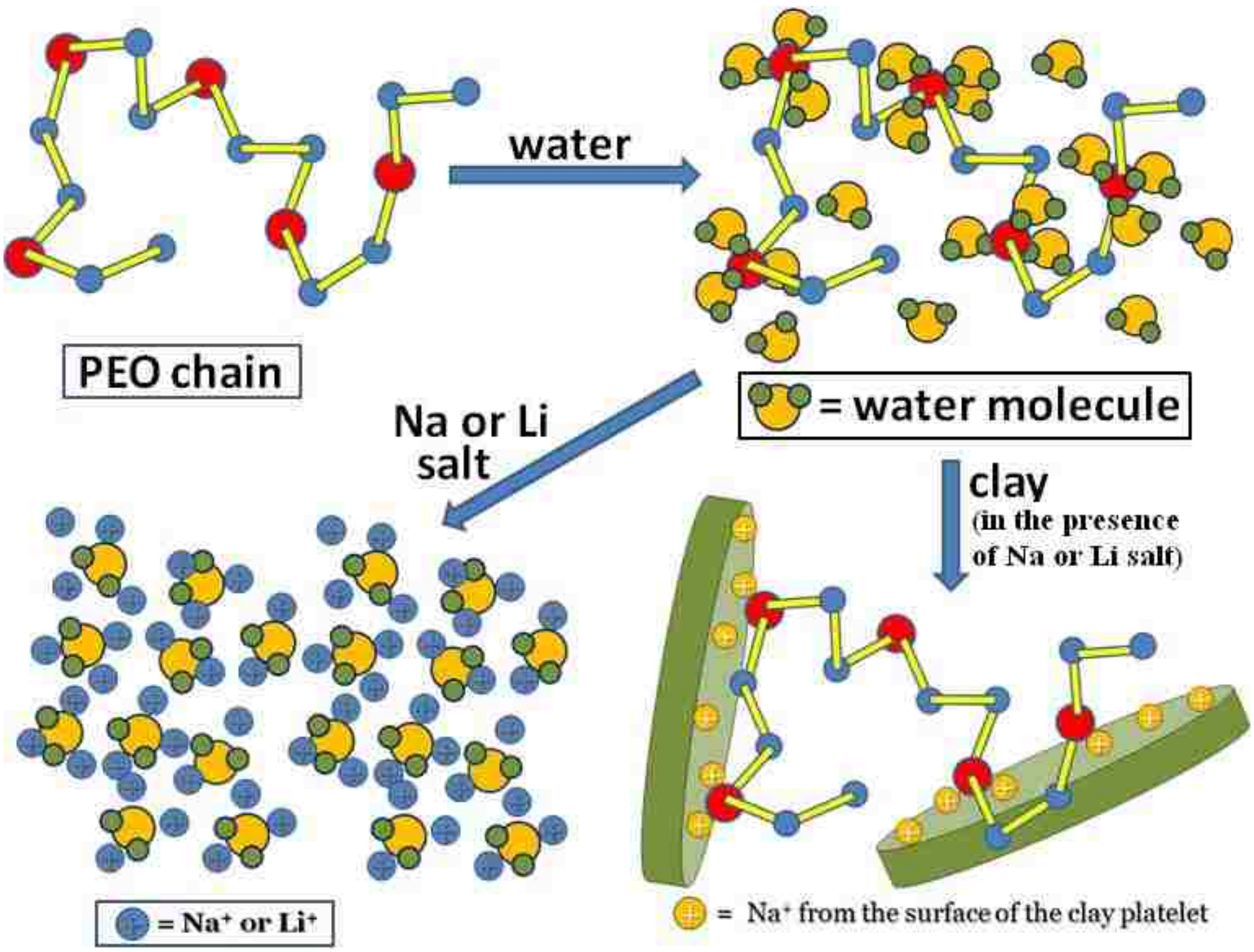

Figure 7.1. Schematic showing the interactions occurring in PEO-clay aqueous dispersions in the presence of metal salts.

Furthermore measurements of the storage modulus of the laponite-based multilayered films and montmorillonite-based films, prepared from the corresponding gels (mentioned above), revealed that montmorillonite films are tougher than the ones containing laponite. While the factor responsible for the elevation of storage modulus in gels was the increase in the strength of the polymer-clay network, the reason for the elevation of storage modulus in the films consists in the increase in crystalline fraction of the PEO in the nanocomposite. Since the strength of the network in solution is given by the fraction of PEO chains cross-linked to the clay platelets, which cannot rearrange and crystallize, we concluded that the strength of the network is inversely proportional to the fraction of crystalline PEO in the film. XRD measurements that were conducted on these films indicated that the gradual replacement of montmorillonite with equivalent amounts of laponite results in an increase in the integrated intensity of the corresponding intercalation peaks up to the point where no montmorillonite is present in the system. This effect was attributed to the differences in the diffraction patterns exhibited by the PEO crystals and the PEO covered stacked platelets, which triggers the formation of destructive interference in the diffraction process (Figure 7.2).

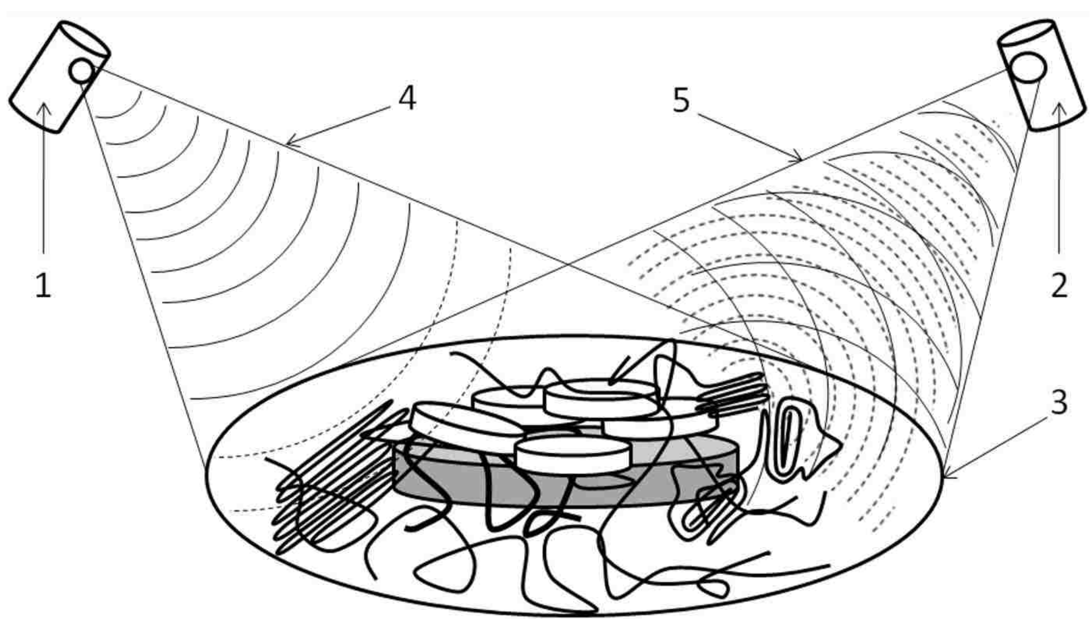

Figure 7.2. Schematic showing the formation of destructive interference when PEO crystals form in the vicinity of clay platelets. In this schematic: 1- X-ray tube, 2- detector, 3 – simplified schematic of a polymer clay film portion (the large grey platelet represents the montmorillonite, and the small white platelets represent the laponite), 4 – incident ray, and 5 – diffracted ray (with the formation of destructive interference).

Furthermore the XRD measurements indicated that the complete absence of montmorillonite platelets from the system causes the laponite platelets to gradually lose parallelism as they keep adding on top of the stack, due to their modest aspect-ratio. This deviation from parallelism of the platelets results in a considerable decrease in the constructive interference of the diffracted beam, diminishing in this way the maximum intensity of the intercalation peak. A schematic showing the laponite platelets losing parallelism is presented in Figure 7.3.

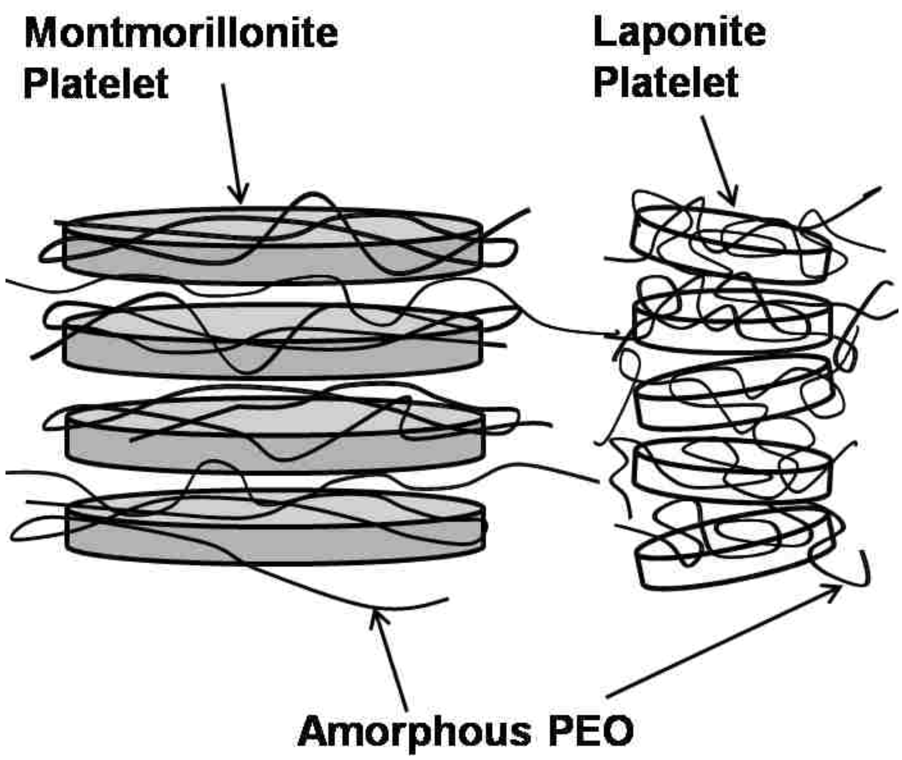

Figure 7.3. Schematic showing the effect of the aspect-ratio on the final parallelism of clay platelets within the PEO-clay stack. The high aspect-ratio montmorillonite platelets are able to maintain parallelism after intercalation of PEO chains while the small aspect-ratio laponite platelets gradually loose parallelism within a stack when PEO chains intercalate between platelets.

We have also compared the multilayered structure of laponite-PEO films with the one of montmorillonite-PEO films and have observed (via AFM measurements) that the high polydispersity in the size of montmorillonite platelets leads to more defects in the order and orientation of the multilayers (Figure 7.4).

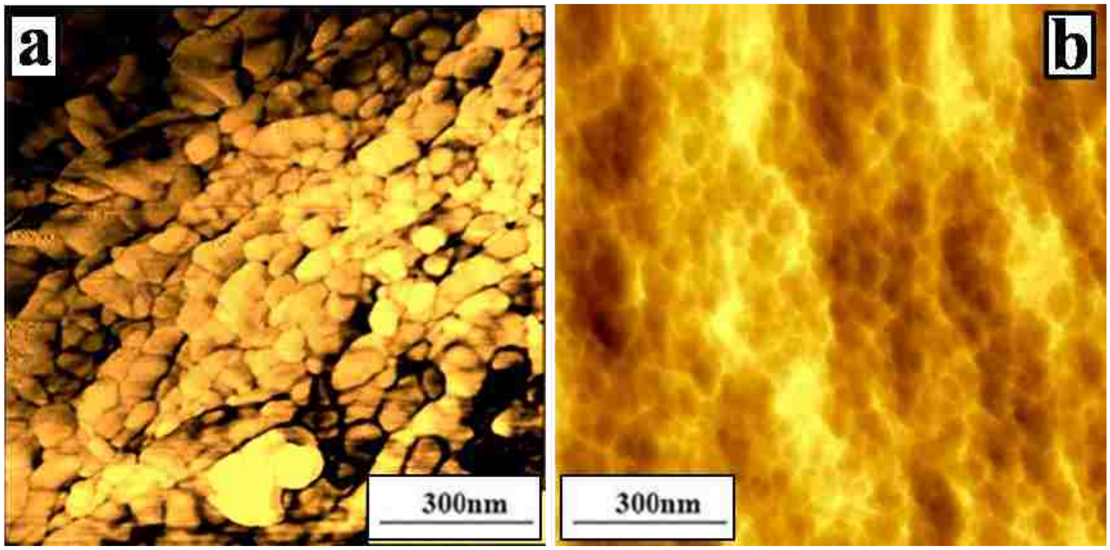

Figure 7.4. AFM phase images from the x-y plane sections of multilayered films for CNA60%-PEO40% (a) and LRD60%-PEO40% (b)

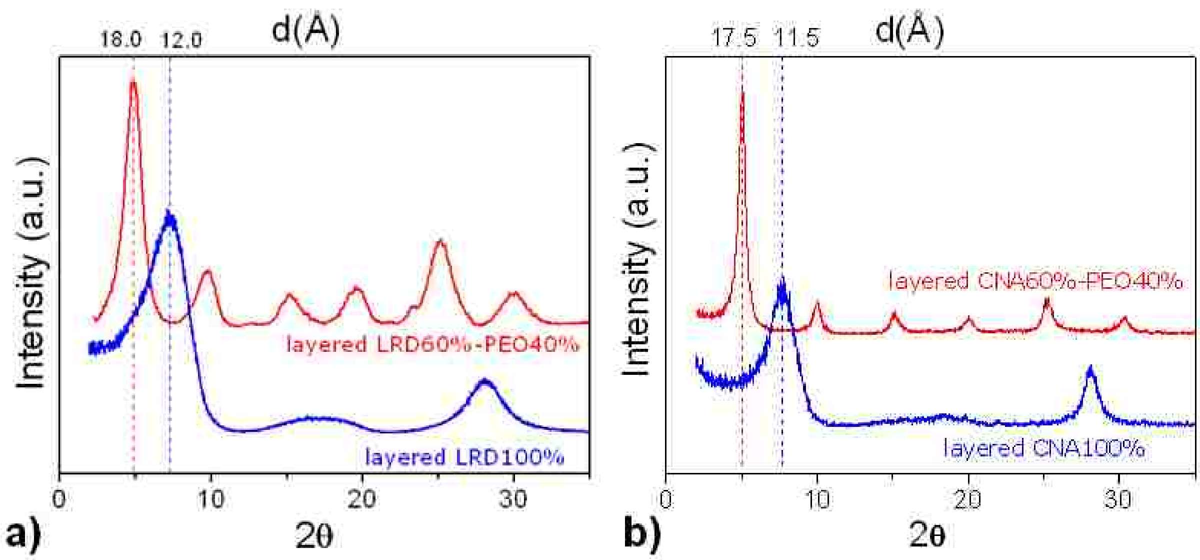

Figure 7.5. XRD reflections from laponite-based (a) and montmorillonite-based multilayered films. The d-spacing values of the intercalation peaks suggest the presence of PEO chains between clay platelets for both LRD60%-PEO40% and CNA60%-PEO40% nanocomposites

Although all the laponite-PEO and montmorillonite-PEO multilayered films were prepared from predominantly exfoliated solutions, XRD measurements proved that during the spreading and drying process of the films intercalation of PEO chains in between clay platelets occurs. The intercalation of the polymer chains between clay platelets is observed as an increase of the d-spacing between clay particles when comparing the layered clay with the layered nanocomposite (Figure 7.5).

We have studied the composition dependence of the structure of PEO-laponite nanocomposites and observed that large amounts of polymer added to the sample leads to an increased crystallinity of the macromolecules in the multilayered film. Evidence from cross polarized optical microscopy showed that besides large crystals and small crystallites these films contain an important fraction of clay aggregates. The cross polarized images in Figure 7.6 show the disappearance of crystalline fraction of polymer in LRD15%-PEO85% (PEO 1000Kg/mol) films when the temperature is increased from 25°C to 85°C. The fact that the small white dots do not melt at 85°C is clearly an indication that they are not PEO crystallites but rather small laponite aggregates.

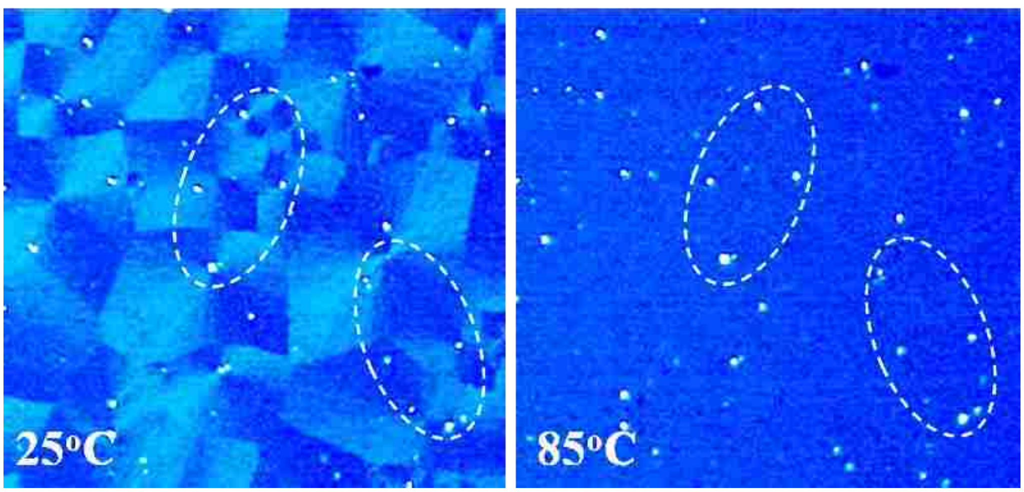

Figure 7.6. Cross polarized microscopy images from the top surface of LRD15%-PEO85% at 25°C and 85°C. Specific features are highlighted for comparison.

Finally, we have examined the kinetics of water adsorption by the PEO-laponite nanocomposites and have observed that the presence of the water molecules and the kinetics of water adsorption strongly influence the polymer crystallinity in the multilayered films. Adsorption of water decreases PEO crystallinity gradually until the polymer becomes amorphous in the nanocomposite.

7.2 Future Work

In the future solid polymer-clay nanocomposites need to be prepared using a melt-intercalation technique. The qualitative comparisons of melt-intercalation solid nanocomposites with solution-intercalation solid nanocomposites will reveal the better method for fabricating conductive films for use in the fields of rechargeable batteries and high density power sources. The new solid nanocomposites should be prepared as a function of polymer/clay ratio, polymer molecular weight, ionic strength, and clay aspect ratio, and should be tested through the same characterization techniques as the old ones, to allow an objective evaluation of results.

The direct link between the strength of the network in gels and the final ionic transport in the multilayered films should be proven. Also, a direct correlation between the crystallinity of PEO in nanocomposite films and the ionic transport in the sample has to be made. Future work should include ionic conductivity measurements on PEO-laponite and PEO-montmorillonite multilayered films. Ionic transport measurements should be performed on films containing various clay/polymer ratios, various water amounts, different clays, and PEOs of different molecular weights. The knowledge and control of crystallinity at the nanometer length scale is critical in tailoring polymer-nanoparticle interactions and thus desired properties. Although ionic conductivity in the polymer crystalline phase has been observed by some scientists, the variation of the conductivity in the crystalline phase of PEO in the presence of clay nanoparticles, and in the presence of ionic salts has to be proven. Finally, it has to be proven that the supramolecular and hierarchical organization of multilayered films, brought by a rigorous control of the film preparation, results in an significant improvement of the unidirectional ionic transport in the solid nanocomposites.

REFERENCES

1. Bujdak, J.; Hackett, E.; Giannelis, E. P., Effect of layer charge on the intercalation of poly(ethylene oxide) in layered silicates: Implications on nanocomposite polymer electrolytes. *Chemistry of Materials* **2000,** 12, (8), 2168-2174.

2. Chaiko, D. J., New poly(ethylene oxide)-clay composites. *Chemistry of Materials* **2003,** 15, (5), 1105-1110.

3. Croce, F.; Appetecchi, G. B.; Persi, L.; Scrosati, B., Nanocomposite polymer electrolytes for lithium batteries. *Nature* **1998,** 394, 456-458.

4. Darder, M.; Aranda, P.; Ruiz-Hitzky, E., Bionanocomposites: A new concept of ecological, bioinspired, and functional hybrid materials. *Advanced Materials* **2007,** 19, 1309-1319.

5. Dundigalla, A.; Lin Gibson, S.; Ferreiro, V.; Malwitz, M. M.; Schmidt, G., Unusual multilayered structures in PEO/laponite nanocomposite films. *Macromolecular Rapid Communications* **2005,** 26, (3), 143-149.

6. Elmahdy, M. M.; Chrissopoulou, K.; Afratis, A.; Floudas, G.; Anastasiadis, S. H., Effect of confinement on polymer segmental motion and ion mobility in PEO/layered silicate nanocomposites. *Macromolecules* **2006,** 39, 5170-5173.

7. Koerner, H.; Jacobs, D.; Tomlin, D. W.; Busbee, J. D.; Vaia, R. D., Tuning polymer nanocomposite morphology: AC electric field manipulation of epoxy-montmorillonite (clay) suspensions. *Advanced Materials* **2004,** 16, 297-302.

8. Lin, J. J.; Chu, C. C.; Chou, C. C.; Shieu, F. S., Self-assembled nanofibers from random silicate platelets. *Advanced Materials* **2005,** 17, 301-304.

9. Lin, J.-J.; Chen, Y.-M., Amphiphilic properties of poly(oxyalkylene)amine-intercalated smectite aluminosilicates, *Langmuir* **2004,** 20, 4261-4264.

10. Loiseau, A.; Tassin, J. F., Model nanocomposites based on laponite and poly(ethylene oxide): Preparation and rheology. *Macromolecules* **2006,** 39, 9185-9191.

11. Mack, J. J.; Viculis, L. M.; Ali, A.; Luoh, R.; Yang, G.; Hahn, T.; Ko, F. K.; Kaner, R. B., Graphite nanoplatelet reinforcement of electrospun polyacrylonitrile nanofibers. *Advanced Materials* **2005,** 17, 77-80.

12. Siripurapu, S.; De Simone, J. M.; Khan, S. A.; Spontak, R. J., Low temperature, surface mediated foaming of polymer films. *Advanced Materials* **2004,** 16, 989-994.

13. Smay, J. E.; Gratson, G. M.; Shepherd, R. F.; Cesarano, J.; J.A., L., Directed colloidal assembly of 3D periodic structures. *Advanced Materials* **2002,** 14, 1279-1283.

14. Stefanescu, E. A.; Dundigalla, A.; Ferreiro, V.; Loizou, E.; Porcar, L.; Negulescu, I.; Garno, J.; Schmidt, G., Supramolecular structures in nanocomposite multilayered films. *Physical Chemistry Chemical Physics* **2006,** 8, (14), 1739-1746.

15. Stefanescu, E. A.; Schexnailder, P. J.; Dundigalla, A.; Negulescu, I. I.; Schmidt, G., Structure and thermal properties of multilayered laponite/PEO nanocomposite films. *Polymer* **2006,** 47, 7339-7348.

16. Tsai, T. Y.; Li, C. H.; Chang, C. H.; Cheng, W. H.; Hwang, C. L.; Wu, R. J., Preparation of exfoliated polymer/clay nanocomposites. *Advanced Materials* **2005,** 17, 1769-1773.

17. Novak, B. M., Hybrid nanocomposite materials - between inorganic glasses and organic polymers. *Advanced Materials* **1993,** 5, (6), 422-433.

18. Schmidt, G.; Malwitz, M. M., Properties of polymer-nanoparticle composites. *Current Opinion in Colloid & Interface Science* **2003,** 8, (1), 103-108.

19. Antonietti, M., *Colloid chemistry I*. Springer: Berlin, 2003; Vol. 226.

20. Krishnamoorti, R.; Vaia, R. A., *Polymer nanocomposites*. ACS: Washington DC, 2002; Vol. 804.

21. Vaia, R. A.; Gianellis, E. P., Polymer nanocomposites: status and applications. *MRS Bulletin* **2001,** 62, (5), 394-401.

22. Gabriel, J. C. P.; Camerel, F.; Lemaire, B. J.; Desvaux, H.; Davidson, P.; Batail, P., Swollen liquid-crystalline lamellar phase based on extended solid-like sheets. *Nature* **2001,** 413, (6855), 504-508.

23. Schmidt, G.; Muller, S.; Schmidt, C.; Richtering, W., Rheo-optical investigations of lyotropic mesophases of polymeric surfactants. *Rheologica Acta* **1999,** 38, (6), 486-494.

24. Schmidt, G.; Muller, S.; Lindner, P.; Schmidt, C.; Richtering, W., Shear orientation of lyotropic hexagonal phases. *Journal of Physical Chemistry B* **1998,** 102, (3), 507-513.

25. Klok, H. A.; Lecommandoux, S., Supramolecular materials via block copolymer self-assembly. *Advanced Materials* **2001,** 13, (16), 1217-1229.

26. Schmidt, G.; Richtering, W.; Lindner, P.; Alexandridis, P., Shear orientation of a hexagonal lyotropic triblock copolymer phase as probed by flow birefringence and small-angle light and neutron scattering. *Macromolecules* **1998,** 31, (7), 2293-2298.

27. Almdal, K.; Koppi, K. A.; Bates, F. S.; Mortensen, K., Multiple ordered phases in a block copolymer melt. *Macromolecules* **1992,** 25, (6), 1743-1751.

28. Rajagopal, K.; Schneider, J. P., Self-assembling peptides and proteins for nanotechnological applications. *Current Opinion in Structural Biology* **2004,** 14, (4), 480-486.

29. Baghdadi, H. A.; Sardinha, H.; Bhatia, S. R., Rheology and gelation kinetics in laponite dispersions containing poly(ethylene oxide). *Journal of Polymer Science Part B-Polymer Physics* **2005,** 43, (2), 233-240.

30. Herrera, N. N.; Letoffe, J. M.; Putaux, J. L.; David, L.; Bourgeat-Lami, E., Aqueous dispersions of silane-functionalized laponite clay platelets: A first step toward the elaboration of water-based polymer/clay nanocomposites. *Langmuir* **2004,** 20, (5), 1564-1571.

31. Liu, J.; Hoffmann, H., Hydrogels in aqueous phases of polyvinylalcohol (PVA), surfactants and clay minerals. *Colloid and Polymer Science* **2004,** 283, (1), 24-32.

32. Schmidt, G.; Nakatani, A. I.; Butler, P. D.; Han, C. C., Small-angle neutron scattering from viscoelastic polymer-clay solutions. *Macromolecules* **2002,** 35, (12), 4725-4732.

33. Schmidt, G.; Nakatani, A. I.; Butler, P. D.; Karim, A.; Han, C. C., Shear orientation of viscoelastic polymer-clay solutions probed by flow birefringence and SANS. *Macromolecules* **2000,** 33, (20), 7219-7222.

34. Schmidt, G.; Nakatani, A. I.; Han, C. C., Rheology and flow-birefringence from viscoelastic polymer-clay solutions. *Rheologica Acta* **2002,** 41, (1-2), 45-54.

35. Zebrowski, J.; Prasad, V.; Zhang, W.; Walker, L. M.; Weitz, D. A., Shake-gels: shear-induced gelation of laponite-PEO mixtures. *Colloids and Surfaces a-Physicochemical and Engineering Aspects* **2003,** 213, (2-3), 189-197.

36. Pozzo, D. C.; Walker, L. M., Reversible shear gelation of polymer-clay dispersions. *Colloids and Surfaces a-Physicochemical and Engineering Aspects* **2004,** 240, (1-3), 187-198.

37. Haraguchi, K.; Takehisa, T., Nanocomposite hydrogels: A unique organic-inorganic network structure with extraordinary mechanical, optical, and swelling/de-swelling properties. *Advanced Materials* **2002,** 14, (16), 1120-1124.

38. Haraguchi, K.; Takehisa, T.; Fan, S., Effects of clay content on the properties of nanocomposite hydrogels composed of poly(N-isopropylacrylamide) and clay. *Macromolecules* **2002,** 35, (27), 10162-10171.

39. Bafna, A.; Beaucage, G.; Mirabella, F.; Mehta, S., 3D Hierarchical orientation in polymer-clay nanocomposite films. *Polymer* **2003,** 44, (4), 1103-1115.

40. Loizou, E.; Butler, P.; Porcar, L.; Schmidt, G., Dynamic responses in nanocomposite hydrogels. *Macromolecules* **2006,** 39, (4), 1614-1619.

41. Loizou, E.; Butler, P. D.; Porcar, L.; Talmon, Y.; Kesselman, E.; Schmidt, G., Large scale structures in polymer-clay hydrogels. *Macromolecules* **2005,** 38, 2047-2049.

42. Chaiko, D. J.; Leyva, A.; Niyogi, S., Nanocomposite manufacturing. *Advanced Materials & Processes* **2003,** 161, (6), 44-46.

43. Aranda, P.; Mosqueda, Y.; Perez-Cappe, E.; Ruiz-Hitzky, E., Electrical characterization of poly(ethylene oxide)-clay nanocomposites prepared by microwave irradiation. *Journal of Polymer Science Part B-Polymer Physics* **2003,** 41, (24), 3249-3263.

44. Aranda, P.; Ruiz-Hitzky, E., Poly(ethylene oxide)/NH_4^+-smectite nanocomposites. *Applied Clay Science* **1999,** 15, (1-2), 119-135.

45. Wu, J. H.; Lerner, M. M., Structural, thermal, and electrical characterization of layered nanocomposites derived from Na-montmorillonite and polyethers. *Chemistry of Materials* **1993,** 5, (6), 835-838.

46. Vaia, R. A.; Vasudevan, S.; Krawiec, W.; Scanlon, L. G.; Giannelis, E. P., New polymer electrolyte nanocomposites - melt intercalation of poly(ethylene oxide) in mica-type silicates. *Advanced Materials* **1995,** 7, (2), 154-156.

47. Lagaly, G., Introduction: From clay mineral-polymer interactions to clay mineral-polymer nanocomposites. *Applied Clay Science* **1999,** 15, (1-2), 1-9.

48. Lagaly, G.; Ziesmer, S., Colloid chemistry of clay minerals: the coagulation of montmorillonite dispersions. *Advances in Colloid and Interface Science* **2003,** 100, 105-128.

49. Strawhecker, K. E.; Manias, E., Crystallization behavior of poly(ethylene oxide) in the presence of Na plus montmorillonite fillers. *Chemistry of Materials* **2003,** 15, (4), 844-849.

50. Gadjourova, Z.; Andreev, Y. G.; Tunstall, D. P.; Bruce, P. G., Ionic conductivity in crystalline polymer electrolytes. *Nature* **2001,** 412, (6846), 520-523.

51. Gadjourova, Z.; Marero, D. M.; Andersen, K. H.; Andreev, Y. G.; Bruce, P. G., Structures of the polymer electrolyte complexes PEO6 : LiXF6 (X = P, Sb), determined from neutron powder diffraction data. *Chemistry of Materials* **2001,** 13, (4), 1282-1285.

52. Bhatia, S. R., Ultra small angle scattering studies of complex fluids. *Current Opinion in Colloid and Interface Science* **2005,** 9, 404-411.

53. Laponite - Performance focused attributes in rheology and specialty film forming applications. *Southern Clay Products - Chem Brief*, June 2001; Vol. 1.

54. www.laponite.com.

55. Avery, R. G.; Ramsay, J. D. F., Colloidal properties of synthetic hectorite clay dispersions. 2. Light and small-angle neutron-scattering. *Journal of Colloid and Interface Science* **1986,** 109, (2), 448-454.

56. Nelson, A.; Cosgrove, T., Dynamic light scattering studies of poly(ethylene oxide) adsorbed on laponite: Layer conformation and its effect on particle stability. *Langmuir* **2004,** 20, (24), 2750-2755.

57. Mori, Y.; Togashi, K.; Nakamura, K., Colloidal properties of synthetic hectorite clay dispersion measured by dynamic light scattering and small angle X-ray scattering. *Advanced Powder Technology* **2001,** 12, (1), 45-59.

58. Cummins, H. Z., Liquid, glass, gel: The phases of colloidal laponite. *Journal of non-crystalline solids* **2007,** 353, 3891–3905.

59. Laponite - performance focused attributes in rheology and specialty film forming applications. *Chem Brief*, Southern Clay Products - June 2001; Vol. 1.

60. http://mineral.galleries.com/minerals/silicate/montmori/montmori.htm.

61. Inyang, H. I.; Bae, S.; Mbamalu, G.; Park, S.-W., Aqueous polymer effects on volumetric swelling of Na-montmorillonite. *Journal of Materials in Civil Engineering* **2007,** 19:1, 84-90.

62. Arias, C. B.; Zaman, A. A.; Talton, J., Rheological behavior and wear abrasion resistanceof polyethylene oxide/laponie nanocomposites. *Journal of Dispersion Science and Technology* **2007,** 28, 247-254.

63. Chen, H.-W.; Chiu, C.-Y.; Wu, H.-D.; Shen, I.-W.; Chang, F.-C., Solid-state electrolyte nanocomposites based on poly(ethylene oxide), poly(oxypropylene) diamine, mineral clay and lithium perchlorate. *Polymer* **2002,** 43, 5011-5016.

64. Doeff, M. M.; Reed, J. S., Li ion conductors based on laponite/poly(ethylene oxide) composites. *Solid State Ionics* **1998,** 113-115, 109-115.

65. Edman, L.; Ferry, A.; Doeff, M. M., Slow recrystallization in the polymer electrolyte system poly(ethylene oxide)(n)-LiN(CF3SO2)(2). *Journal of Materials Research* **2000,** 15, (9), 1950-1954.

66. Loyens, W.; Maurer, H. J. F.; Jannasch, P., Melt-compounded salt-containing poly(ethylene oxide)/clay nanocomposites for polymer electrolyte membranes. *Polymer* **2005,** 46, 7334-7345.

67. Malwitz, M. M.; Dundigalla, A.; Ferreiro, V.; Butler, P. D.; Henk, M. C.; Schmidt, G., Layered structures of shear-oriented and multilayered PEO/silicate nanocomposite films. *Physical Chemistry Chemical Physics* **2004,** 6, (11), 2977-2982.

68. Cowie, J. M. G., *Polymers: Chemistry & Physics of Modern Materials*. 2nd ed.; Nelson Thornes Ltd: Cheltenham, UK, 1991; p 436.

69. Odian, G., *Principles of Polymerization*. 3rd ed.; Wiley - Interscience: USA, 1991; p 768.

70. Young, R. J.; Lovell, P. A., *Introduction to Polymers*. 2nd ed.; CRC Press LLC: Boca Raton, FL 33431, 1991; p 443.

71. Sperling, L. H., *Introduction to Physical Polymer Science*. John Wiley and Sons: New Jersey, 2006; p 845.

72. Florin, E.; Kjellander, R.; Eriksson, J. C., Salt effects on the cloud point of the poly(ethylene-oxide)+water system. *J. Chem. Soc., Faraday Trans.* **1984,** 80, 2889-2910.

73. Kjellander, R.; Florin, E., Water structure and changes in thermal stability of the system poly(ethylene oxide)-water. *J. Chem. Soc., Faraday Trans.* **1981,** 77, 2053-2077.

74. Hammouda, B.; Ho, D. L.; Kline, S., Insight into clustering in poly(ethylene oxide) solutions. *Macromolecules* **2004,** 37, (18), 6932-6937.

75. Briscoe, B.; Luckham, P.; Zhu, S., Rheological study of poly(ethylene oxide) in aqueous salt solutions at high temperature and pressure. *Macromolecules* **1996,** 29, 6208-6211.

76. Daga, V. K.; Wagner, N. J., Linear viscoelastic master curves of neat and laponite-filled poly(ethylene oxide)- water solutions. *Rheol. Acta* **2006,** 45, 813-824.

77. Malwitz, M. M.; Lin-Gibson, S.; Hobbie, E. K.; Butler, P. D.; Schmidt, G., Orientation of platelets in multilayered nanocomposite polymer films. *Journal of Polymer Science Part B-Polymer Physics* **2003,** 41, (24), 3237-3248.

78. Tang, Z. Y.; Kotov, N. A.; Magonov, S.; Ozturk, B., Nanostructured artificial nacre. *Nature Materials* **2003,** 2, (6), 413-U8.

79. Decher, G.; Schlenoff, J., *Multilayer thin films: Sequential assembly of nanocomposite materials*. VCH Verlagsgesellschaft: 2003.

80. Macosko, C. W., *Rheology: Principles, measurements, and applications*. Wiley - VCH: 1994; p 550.

81. Morrison, F. A., *Understanding rheology*. Oxford University Press, Inc.: New York, 10016, 2001; p 545.

82. Larson, L. G., *The structure and rheology of complex fluids*. Oxford University Press: New York, 1999; p 663.

83. Menard, K. P., *Dynamic mechanical analysis: A practical introduction*. CRC Press LLC: Boca Raton, FL, 33431, 1999; p 208.

84. Dealy, J. M.; Wissbrun, K. F., *Melt rheology and its role in plastics processing; theory and applications*. Kluwer Academic Publishers: The Netherlands, 1999.

85. Collier, J. R., Lubricated Flow Elongational Rheometer. *U.S. Patent 5,357,784* **1994,** issued to LSU.

86. Collier, J. R.; Petrovan, S.; Patil, P.; Collier, B., Elongational rheology of fiber forming polymers. *Journal of Materials Science* **2005,** 40, (19), 5133-5137.

87. Collier, J. R.; Romanoschi, O.; Petrovan, S., Elongational rheology of polymer melts and solutions. *Journal of Applied Polymer Science* **1998,** 69, 2357-2367.

88. Kim, H. C.; Pendse, A.; Collier, J. R., Polymer melt lubricated elongational flow. *J. Rheol.* **1994,** 38, (4), 831-845.

89. Feigl, K.; Tanner, F. X.; Edwards, B. J.; Collier, J. R., A numerical study of the measurement of elongational viscosity of polymeric fluids in a semihyperbolically converging die. *J. Non-Newton. Fluid. Mech.* **2003,** 115, (191).

90. Heal, G. R.; Laye, P. G.; Price, D. M.; Warrington, S. B.; Wilson, R. J., *Principles of thermal analysis and calorimetry*. The Royal Society of Chemistry: Cambridge, UK, 2002; p 220.

91. Benoist, L.; Berghmans, H.; Hemminger, W.; Hohne, G. W. H.; Jansen, J. A. J.; Mathot, V. B. F.; Richardson, M. J.; Riesen, R.; Schuijff, A.; Wingfield, M., *Calorimetry and thermal analysis of polymers*. Hanser/Gardner Publications, Inc.: Geleen, The Netherlands, 1994; p 369.

92. Negulescu, I. I.; Daly, W. H., Application of oscillating DSC to the detection of thermal transitions in poly (γ - alkyl - α, L - glutamate) *Polymer Preprints* **1994,** 35, (1), 441-442.

93. Wunderlich, B., *Thermal analysis*. Academic Press, Inc.: San Diego, CA 92101, USA, 1990; p 450.

94. Warren, B. E., *X-Ray diffraction*. Dover Publications, Inc.: N.Y. 11501, USA, 1990; p 381.

95. Moore, D. M.; Reynolds, R. C., Jr, *X-ray diffraction of clay minerals*. 2nd ed.; Oxford University Press, Inc.: N.Y. 10016, USA, 1997; p 378.

96. Cullity, B. D., *Elements of X-ray diffraction*. 2nd ed.; Addison-Wesley Publishing Company, Inc.: USA, 1978; p 555.

97. Moore, D. M.; Reynolds, R. C. J., *X-ray diffraction and the identification and analysis of clay minerals*. 2nd ed.; Oxford University press, Inc.: 198 Madison Avenue, New York, NY 10016, 1997; p 378.

98. Goldstein, J.; Newbury, D.; Joy, D.; Lyman, C.; Echlin, P.; Lifshin, E.; Sawyer, L.; Michael, J., *Scanning electron microscopy and X-ray microanalysis*. 3rd ed.; Springer Science + Business Media, Inc.: N.Y.10013, USA, 2003; p 689.

99. Echlin, P.; Fiori, C. E.; Goldstein, J.; Joy, D. C.; Newbury, D. E., *Advanced scanning electron microscopy and X-ray microanalysis.* Plenum Press: New York, 1986; p 454.

100. Egerton, R. F., *Physical principles of electron microscopy: An introduction to TEM, SEM, and AEM*. Springer Science & Business Media, Inc.: New York, 2005.

101. Bragga, P. C.; Ricci, D., *Atomic force microscopy - biomedical methods and applications*. Humana Press Inc.: N.J. 07512, USA, 2004; p 394.

102. Morita, S.; Wiesendanger, R.; Meyer, E., *Noncontact atomic force microscopy*. Springer-Verlag Berlin Heidelberg: 2002; p 439.

103. Robinson, P. C.; Davidson, M. W., *Introduction to polarized light microscopy*. http://www.microscopyu.com/articles/polarized/polarizedintro.html **2006**.

104. Malwitz, M. M.; Butler, P. D.; Porcar, L.; Angelette, D. P.; Schmidt, G., Orientation and relaxation of polymer-clay solutions studied by rheology and small-angle neutron scattering. *Journal of Polymer Science Part B-Polymer Physics* **2004,** 42, (17), 3102-3112.

105. Nielsen, L. E., *Mechanical properties of polymers and composites*. Marcel Dekker, Inc: 1974; Vol. 1.

106. Ratna, D.; Divekar, S.; Samui, A. B.; Chakraborty, B. C.; Banthia, A. K., Poly(ethylene oxide)/clay nanocomposite: Thermomechanical properties and morphology. *Polymer* **2006,** 47, 4068-4074.

107. Chen, H.-W.; Chang, F.-C., The novel polymer electrolyte nanocomposite composed of poly(ethylene oxide), lithium triflate and mineral clay. *Polymer* **2001,** 42, 9763-9769.

108. Polydispersity is estimated to be ca. 30% by the supplier.

109. Brandup, J.; Immergut, E. H.; Grulke, E. A., *Polymer handbook*. John Wiley and Sons: 1999.

110. Ho, D. L.; Briber, R. M.; Glinka, C. J., Characterization of organically modified clays using scattering and microscopy techniques. *Chemistry of Materials* **2001,** 13, (5), 1923-1931.

111. Hanley, H. J. M.; Muzny, C. D.; Ho, D. L.; Glinka, C. J., A Small angle neutron scattering study of a commercial organoclay dispersion. *Langmuir* **2003,** 19, 5575-5580.

112. Thompson, D. W.; Butterworth, J. T., The nature of laponite and its aqueous dispersions. *Journal of Colloid and Interface Science* **1992,** 151, (1), 236-243.

113. Glinka, C. J.; Barker, J. G.; Hammouda, B.; Krueger, S.; Moyer, J. J.; Orts, W. J., The 30m small-angle neutron scattering instruments at the National Institute of Standards and Technology. *Journal of Applied Crystallography* **1998,** 31, 430-445.

114. Ferreiro, V.; Coulon, G., Shear banding in strained semicrystalline polyamide 6 films as revealed by atomic force microscopy: Role of the amorphous phase. *J. Polym. Sci. : Polym. Phys. Part. B* **2004,** 42, 687-701.

115. Ogata, N.; Kawakage, S.; Ogihara, T., Structure and thermal/mechanical properties of poly(ethylene oxide) clay mineral blends. *Polymer* **1997,** 38, (20), 5115-5118.

APPENDIX: COPYRIGHT PERMISSIONS

ELSEVIER LIMITED LICENSE
TERMS AND CONDITIONS

Feb 07, 2008

This is a License Agreement between Eduard A Stefanescu ("You") and Elsevier Limited ("Elsevier Limited"). The license consists of your order details, the terms and conditions provided by Elsevier Limited, and the payment terms and conditions.

License Number	1883780718938
License date	Feb 07, 2008
Licensed content publisher	Elsevier Limited
Licensed content publication	Polymer
Licensed content title	Structure and thermal properties of multilayered Laponite/PEO nanocomposite films
Licensed content author	Stefanescu Eduard A., Schexnailder Patrick J., Dundigalla Avinash, Negulescu Ioan I. and Schmidt Gudrun
Licensed content date	4 October 2006
Volume number	47
Issue number	21
Pages	10
Type of Use	Thesis / Dissertation
Portion	Figures/table/illustration/abstracts
Quantity	1
Format	Electronic
You are an author of the Elsevier article	Yes
Are you translating?	No
Purchase order number	
Expected publication date	Jun 2008
Elsevier VAT number	GB 494 6272 12
Permissions price	0.00 USD
Value added tax 0.0%	0.00 USD
Total	0.00 USD
Terms and Conditions	

GENERAL TERMS

Elsevier hereby grants you permission to reproduce the aforementioned material subject to the terms and conditions indicated.

Acknowledgement: If any part of the material to be used (for example, figures) has appeared in our publication with credit or acknowledgement to another source, permission must also be sought from that source. If such permission is not obtained then that material may not be included in your publication/copies. Suitable acknowledgement to the source must be made, either as a footnote or in a reference list at the end of your publication, as follows:

"Reprinted from Publication title, Vol number, Author(s), Title of article, Pages No., Copyright (Year), with permission from Elsevier [OR APPLICABLE SOCIETY COPYRIGHT OWNER]." Also Lancet special credit - "Reprinted from The Lancet, Vol. number, Author(s), Title of article, Pages No., Copyright (Year), with permission from Elsevier."

Reproduction of this material is confined to the purpose and/or media for which permission is hereby given.

Altering/Modifying Material: Not Permitted. However figures and illustrations may be altered/adapted minimally to serve your work. Any other abbreviations, additions, deletions and/or any other alterations shall be made only with prior written authorization of Elsevier Ltd. (Please contact Elsevier at permissions@elsevier.com)

If the permission fee for the requested use of our material is waived in this instance, please be advised that your future requests for Elsevier materials may attract a fee.

Reservation of Rights: Publisher reserves all rights not specifically granted in the combination of (i) the license details provided by you and accepted in the course of this licensing transaction, (ii) these terms and conditions and (iii) CCC's Billing and Payment terms and conditions.

License Contingent Upon Payment: While you may exercise the rights licensed immediately upon issuance of the license at the end of the licensing process for the transaction, provided that you have disclosed complete and accurate details of your proposed use, no license is finally effective unless and until full payment is received from you (either by publisher or by CCC) as provided in CCC's Billing and Payment terms and conditions. If full payment is not received on a timely basis, then any license preliminarily granted shall be deemed automatically revoked and shall be void as if never granted. Further, in the event that you breach any of these terms and conditions or any of CCC's Billing and Payment terms and conditions, the license is automatically revoked and shall be void as if never granted. Use of materials as described in a revoked license, as well as any use of the materials beyond the scope of an unrevoked license, may constitute copyright infringement and publisher reserves the right to take any and all action to protect its copyright in the materials.

Warranties: Publisher makes no representations or warranties with respect to the licensed material.

LIMITED LICENSE

Electronic reserve: If licensed material is to be posted to website, the web site is to be password-protected and made available only to bona fide students registered on a relevant course if:
This license was made in connection with a course,
This permission is granted for 1 year only. You may obtain a license for future website posting,
All content posted to the web site must maintain the copyright information line on the bottom of each image,

Thesis/Dissertation: If your license is for use in a thesis/dissertation your thesis may be submitted to your institution in either print or electronic form. Should your thesis be published commercially, please reapply for permission. These requirements include permission for the Library and Archives of Canada to supply single copies, on demand, of the complete thesis and include permission for UMI to supply single copies, on demand, of the complete thesis. Should your thesis be published commercially, please reapply for permission.

ELSEVIER

RSC | Advancing the Chemical Sciences

The Royal Society of Chemistry (RSC) hereby grants permission for the use of your paper(s) specified below in the printed and microfilm version of your thesis. You may also make available the PDF version of your paper(s) that the RSC sent to the corresponding author(s) of your paper(s) upon publication of the paper(s) in the following ways: in your thesis via any website that your university may have for the deposition of theses, via your university's Intranet or via your own personal website. We are however unable to grant you permission to include the PDF version of the paper(s) on its own in your institutional repository. The Royal Society of Chemistry is a signatory to the STM Guidelines on Permissions (available on request).

Please note that if the material specified below or any part of it appears with credit or acknowledgement to a third party then you must also secure permission from that third party before reproducing that material.

Please ensure that the published article states the following:

Reproduced by permission of the PCCP Owner Societies.

Regards,

Gill Cockhead

Contracts & Copyright Executive

Gill Cockhead (Mrs), Contracts & Copyright Executive
Royal Society of Chemistry, Thomas Graham House
Science Park, Milton Road, Cambridge CB4 0WF, UK
Tel +44 (0) 1223 432134, Fax +44 (0) 1223 423623
http://www.rsc.org

Dear Customer,

Thank you for your email.

We hereby grant permission for the requested use expected that due credit is given to the original source.

If material appears within our work with credit to another source, authorisation from that source must be obtained.

Credit must include the following components:
- Books: Author(s)/ Editor(s) Name(s): Title of the Book. Page(s). Publication year. Copyright Wiley-VCH Verlag GmbH & Co. KGaA. Reproduced with permission.

- Journals: Author(s) Name(s): Title of the Article. Name of the Journal. Publication year. Volume. Page(s). Copyright Wiley-VCH Verlag GmbH & Co. KGaA. Reproduced with permission.

With kind regards

Bettina Loycke
****

Bettina Loycke
Copyright & Licensing Manager
Wiley-VCH Verlag GmbH & Co. KGaA
Boschstr. 12
69469 Weinheim
Germany

Phone: +49 (0) 62 01- 606 - 280
Fax: +49 (0) 62 01 - 606 - 332
Email: rights@wiley-vch.de

VITA

Eduard A. Stefanescu was born in 1980 in Iasi, Romania. After graduating from a public high school, he enrolled in the fall of 1999 at the Industrial Chemistry Department of the Technical University of Iasi, Romania. During the last of the five years spent there, Eduard prepared his thesis work with the help and guidance of Professor Nicolae Hurduc. His thesis title was “Industrial Processing of poly(styrene-co-butadiene) rubber”. In the summer of 2004 he obtained a Bachelor of Science from the Industrial Chemistry Department of the Technical University of Iasi, graduating with the highest GPA in his class. Later that summer he moved to the United States to pursue a Doctor of Philosophy in the Chemistry Department of Louisiana State University. He joined Professor Gudrun Schmidt’s research group in January 2005. Because Professor Gudrun Schmidt left Louisiana State University in August 2006, Eduard joined that summer the research group of Professors William H. Daly and Ioan I. Negulescu. During this period he became familiar with the concept of polymer-clay nanocomposites and he developed a strong knowledge in the fields of rheological and thermo-mechanical characterization of polymer based materials. His dissertation focuses on the rheological and thermodynamic properties of polymer-clay dispersions and multilayered thin films prepared from such dispersions.